Title
Fault Detection and Handling for Longitudinal Control

Authors
Yi, Jingang
Howell, Adam
Horowitz, Roberto
et al.

Publication Date
2001-09-01

CALIFORNIA PATH PROGRAM
INSTITUTE OF TRANSPORTATION STUDIES
UNIVERSITY OF CALIFORNIA, BERKELEY

Fault Detection and Handling for Longitudinal Control

Jingang Yi, Adam Howell, Roberto Horowitz,
Karl Hedrick, Luis Alvarez
University of California, Berkeley

California PATH Research Report
UCB-ITS-PRR-2001-21

This work was performed as part of the California PATH Program of the University of California, in cooperation with the State of California Business, Transportation, and Housing Agency, Department of Transportation; and the United States Department of Transportation, Federal Highway Administration.

Report for MOU 312

September 2001

ISSN 1055-1425

Fault Detection and Handling for Longitudinal Control of AHS

Jingang Yi, Adam Howell, Roberto Horowitz, Karl Hedrick
Department of Mechanical Engineering
Univeristy of California at Berkeley

Luis Alvarez
Instituto de Ingeniería
Universidad Nacional Autónoma de México

May 17, 2001

ABSTRACT

The purpose of this project is to extend and integrate existing results on fault diagnostics and fault management for passenger vehicles used in automated highway systems (AHS). These results have been combined to form a fault diagnostic and management system for the longitudinal control system of the automated vehicles which has a heirarchical framework that complements the established PATH control system. Furthermore, the fault diagnostic module effectively monitors all of the sensors and actuators required for longitudinal control, while the fault handling module corrects for any detected faults via controller reconfiguration and degraded modes of operation. Simulations using the SHIFT programming language are presented to demonstrate the performance of the fault diagnostic and management system for different fault scenarios. Limited experimental results are also provided to show the initial stages of real-time implementation.

KEYWORDS

Fault diagnostics, fault handling, automated highway systems (AHS), hybrid systems, simulation, SHIFT, tire/road friction estimation

ACKNOWLEDGEMENT

This work was executed under grant MOU312 of the the Institute of Transportation Studies at the University of California at Berkeley and part of a large effort to develop the SmartAHS simulation package. The authors would specially like to thank Tunc Simsic at the Department of Electrical Engineering and Computer Sciences at UC Berkeley and Joel VanderWerf at California PATH headquarter for all of their help with the use of the SHIFT programming language.

Executive Summary

This project presents the design and verification of a unified framework for a fault tolerant AHS longitudinal control system which combines previous and current work in the areas of fault diagnosis and fault handling. This fault tolerant control system is an extension of the normal mode hierarchical control architecture presented in Varaiya (1993), which incorporates all of the existing AHS control laws and maneuver protocols.

A systematic design for the fault diagnostic system based on model-based techniques is presented. A combination of parity equations, linear observers, and nonlinear observers is used to create a set of signals sensitive to faults in the longitudinal control components. A linear least squares estimation scheme is developed to detect, identify, and estimate the magnitude of the component faults. Results from simulations show good performance, however limited experimental results indicate further modeling and tuning is required.

The fault handling system consists of two structures to compensate for faults and degraded system performance. The capability structure relies on a set of degraded mode maneuvers to ensure the safety of the automated vehicles when a critical fault occurs. The performance structure uses controller reconfiguration to minimize the loss of AHS performance due to minor faults, adverse weather conditions, and comonent wear. Moreover, a scheme for road/tire friction estimation has been added to the performance structure for handling adverse environmental conditions. Simulation results shows that the estimation scheme can identify the road/tire conditions without priori highway information while guaranteeing the safety by underestimation of friction coefficient.

Finally, a high fidelity nonlinear vehicle model and the complete fault tolerant AHS control architecture has been implemented and tested in the SmartAHS micro-simulator. Simulations of the fault tolerant control architecture under each component fault are also presented.

Contents

List of Figures

List of Tables

Chapter 1

Introduction

Over the last ten years, PATH's Advanced Vehicle Control System effort has made impressive strides in the modeling, control design and implementation of several vehicle control laws. From the overall Automated Highway Systems (AHS) point of view, the two most important requirements of an AHS are to significantly increase the capacity and safety of highway travel.

To satisfy these requirements, the AHS should be designed such that the automated vehicles are able to safely operate under abnormal conditions, as well as under nominal conditions. The nominal operating condition assumes the faultless operation of the system components and benign environmental conditions. The abnormal operating conditions are which are generally considered include(Lygeros *et al.* 2000; Godbole *et al.* 2000):

1. Hard Faults: these include failures or faults in one of the control system components, such as mechanical failures in the vehicles, failures in sensing, communication, control and actuation both on the vehicle and the roadside.

2. Soft Faults: these include Adverse environmental conditions, such as rain, fog, snow, etc. and the loss of performance due to gradual wear of AHS components.

The AHS address these two classes of operating conditions by switching between two general modes of operation: normal mode, which gives optimal performance under nominal conditions, and several degraded modes, which ensure safety and attempt to minimize performance degradation under abnormal conditions. A great deal of effort has been dedicated towards the design of a robust controllers for both modes of operation. Normal mode control laws at the regulation, coordination and link layer have been developed and tested in simulations and experiments. Fault detection algorithms for the onboard sensor and actuator critical to automated control have been developed and tested in simulations and experiments (Garg 1995; Chung *et al.* 1996; Chung *et al.* 1997; Patwardhan 1994a; Agogino *et al.* 1997; Rajamani *et al.* 1997; Rajamani *et al.* 1997). At the same time, fault handling schemes using new maneuvers and control laws have been designed for degraded modes of operation to ensure that the safety of the AHS is maintained and the performance loss is minimized in abnormal situations (Lygeros *et al.* 2000; Godbole *et al.* 2000; Chen *et al.* 1997). In addition, these fault handling schemes have been successfully tested in the SmartPATH simulation program (Carbaugh *et al.* 1997).

The goal of this project is to merge and improve these developments in the areas of fault diagnostics and fault handling with the existing control hierarchy (Varaiya 1993) to produce a complete fault tolerant AHS control system that can be implemented on the vehicles and the roadway. The

project concentrates on the design of a fault tolerant AHS control system that can detect and handle both hard and soft faults in the longitudinal control system. However, acts of nature, such as earthquakes, floods, etc. and obstacles on the road are not considered in order to limit the scope of the project. The overall structure of the fault tolerant AHS control system is shown schematically in Figure 1.1.

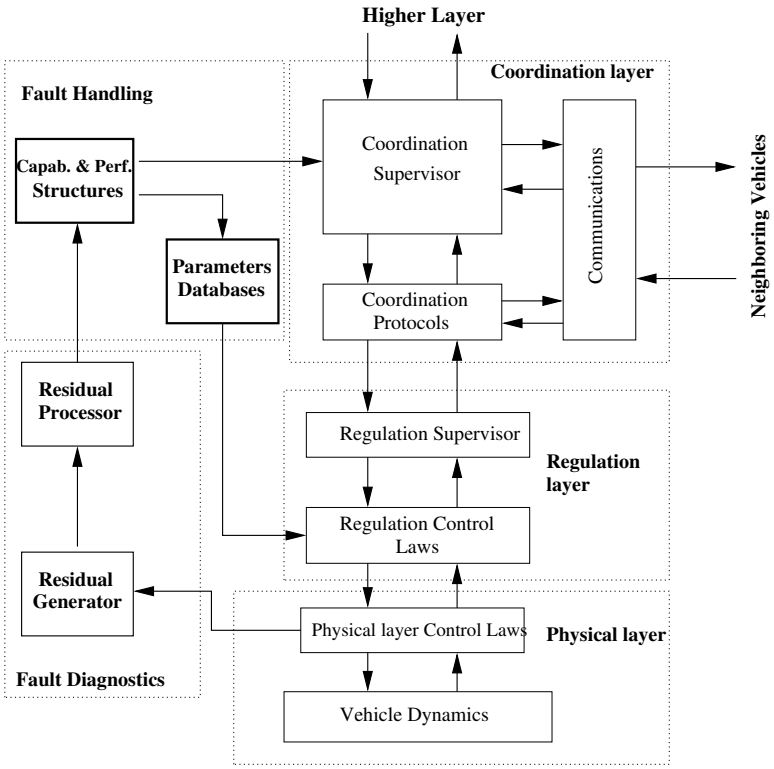

Figure 1.1: Extended hierarchical fault tolerant AHS controller

In addition to the design of the fault tolerant AHS control system, the considerable task of implementing the entire system and vehicle models in SmartAHS, a micro-simulator written in SHIFT, was also completed. SHIFT is a programming language developed at PATH to simulate the behavior of large scale hybrid systems (Deshpande *et al.* 1997). The fault diagnostic and fault handling modules of the system, except for the estimation of tire/road friction and braking capability, are also rigorously tested in SmartAHS.

The remainder of this report is divided into five chapters which discuss the details of each portion of the fault tolerant controller shown in Figure 1.1. Chapter 2 introduces the vehicle model that is used as a basis for the development of the automated control system and vehicle simulation software. In chapter 3, the normal mode longitudinal controller of the PATH control hierarchical architecture is reviewed. Chapter 4 describes the design of a complete fault diagnostic system for the physical layer longitudinal controllers. Simulation and experimental results are also presented for all faults in sensors and actuators. Chapter 5 describes the fault management system for the regulation and coordination layers. The capability structure for normal mode maneuvers are discussed along with simulations for all faults in the onboard sensors, actuators and communication devices. In addition, a scheme to estimate the friction coefficient of the tire/road interface and the braking capability of vehicles is also presented in this chapter (Alvarez *et al.* 2000; Alvarez and Yi 1999). Concluding remarks and a discussion of possible future work are presented in chapter 6.

Finally, appendix A describes the structure of the SmartAHS simulation software developed for testing of the complete system.

Chapter 2

Vehicle Model

This chapter presents a mathematical model of a passenger car equipped with a spark ignition engine and automatic transmission. While only a brief overview of the model is presented, a more detailed coverage of the the longitudinal vehicle dynamics and powertrain model can be found in (McMahon 1994; Gerdes 1996; Cho 1987; Moskwa 1988), while the lateral dynamics are described in (Patwardhan 1994b; Peng 1992; Pham 1996).

The vehicle model presented in this chapter is a six-degree of freedom nonlinear model based on both analytical derivations and experimental data. The vehicle is modeled as a sprung mass, representing the vehicle body and the drivetrain, attached to a negligible unsprung mass, the wheels and tires, via the suspension. The remaining sections will describe in more detail the dynamics associated with the sprung mass, the powertrain, the brake system, the suspension and finally the wheels and tires.

2.1 Sprung Mass Dynamics

The sprung mass is modeled as a rigid body, so Newton-Euler equations are employed to obtain the differential equations of motion along it's six degrees of freedom; longitudinal, lateral and vertical translations, and roll, pitch, and yaw rotations. A diagram of the coordinate system is shown in Figure 2.1,

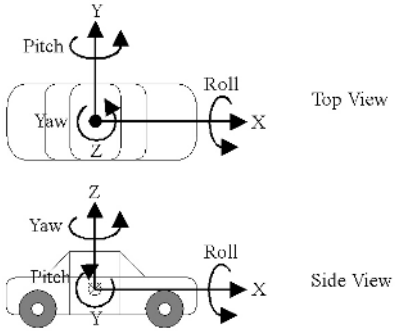

Figure 2.1: Diagram of Vehicle Model Coordinate Axes

The forces acting on the vehicle are the traction forces from the tires (F_{ti}), the aerodynamic

drag ($c_x\dot{x}^2$), the suspension forces (F_{pi}), and gravitational forces as a function of road grade and banking (Δ and γ, respectively). Losses due to rolling resistance in the tires are included in the term T_{rr}. These forces affect the sprung mass as shown on the free body diagram in Figure 2.2.

Considering these external forces and the three dimensional kinematics of the vehicle, the following differential equations describing the vehicle's motion can be derived

$$\begin{aligned}
\ddot{x} &= \frac{\sum_{i=1}^{4} F_{txi} - c_x\dot{x}^2 sign(\dot{x}) - T_{rr}}{M} + \dot{y}\dot{\epsilon} - \dot{z}\dot{\theta} + g\sin(\Delta) \\
\ddot{y} &= \frac{\sum_{i=1}^{4} F_{tyi} - c_y\dot{y}^2 sign(\dot{y})}{M} - \dot{x}\dot{\epsilon} + \dot{z}\dot{\phi} + g\cos(\Delta)\sin(\gamma) \\
\ddot{z} &= \frac{\sum_{i=1}^{4} F_{pi}}{M} + \dot{x}w_y - \dot{y}w_x + g\cos(\Delta)\cos(\gamma)
\end{aligned}$$

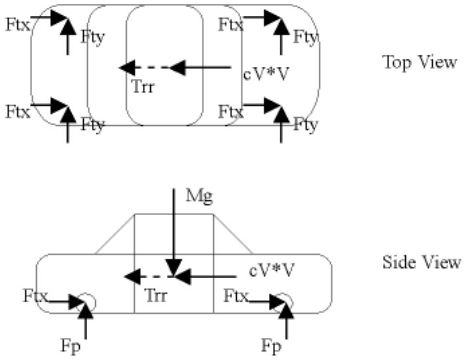

Figure 2.2: Sprung Mass Free-body Diagram

$$\begin{aligned}
I_x\ddot{\phi} &= (I_y - I_z)\dot{\theta}\dot{\epsilon} + M_x \\
I_y\ddot{\theta} &= (I_z - I_x)\dot{\epsilon}\dot{\phi} + M_y \\
I_z\ddot{\epsilon} &= (I_x - I_y)\dot{\phi}\dot{\theta} + M_z
\end{aligned}$$

The moments acting on the sprung mass are caused by the tractive forces (F_{txi}) and the sus-

pension forces (F_{pi}), which are related geometrically by the following algebraic equations

$$\begin{aligned}
M_x &= \frac{1}{2}(\sin(\theta)((F_{tx1}-F_{tx2})s_{b1}+(F_{tx3}-F_{tx4})s_{b2}) \\
&\quad +\cos(\theta)\sin(\phi)((F_{ty1}-F_{ty2})s_{b1}+(F_{ty3}-F_{ty4})s_{b2}) \\
&\quad +\cos(\theta)\cos(\phi)((F_{p1}-F_{p2})s_{b1}+(F_{p3}-F_{p4})s_{b2})) \\
&\quad -\sin(\theta)\sin(\phi)H_0\sum_{i=1}^{4}F_{txi}+\cos(\theta)H_0\sum_{i=1}^{4}F_{tyi} \\
M_y &= -H_0\cos(\phi)\sum_{i=1}^{4}F_{txi} \\
&\quad -\sin(\theta)((F_{tx1}+F_{tx2})l_1-(F_{tx3}+F_{tx4})l_2) \\
&\quad +\cos(\theta)\sin(\phi)((F_{ty1}+F_{ty2})l_1-(F_{ty3}+F_{ty4})l_2) \\
&\quad -\cos(\theta)\cos(\phi)((F_{p1}+F_{p2})l_1-(F_{p3}+F_{p4})l_2) \\
M_z &= \cos(\phi)((F_{ty1}+F_{ty2})l_1-(F_{ty3}+F_{ty4})l_2) \\
&\quad +\sin(\phi)((F_{p1}+F_{p2})l_1-(F_{p3}+F_{p4})l_2) \\
&\quad -\frac{1}{2}(\cos(\theta)(s_{b1}(F_{tx1}-F_{tx2})+s_{b2}(F_{tx3}-F_{tx4})) \\
&\quad +\sin(\theta)\sin(\phi)(s_{b1}(F_{ty1}-F_{ty2})+s_{b2}(F_{ty3}-F_{ty4})))
\end{aligned}$$

2.2 Powertrain

The most significant forces acting on the sprung mass are the tractive forces generated at the tires. These forces are a result of the power generated and delivered to the wheels by the powertrain. The powertrain in turn is composed of three subsystems, the engine, the torque converter, and the transmission. The equations of motion associated with each of these subsystems will now be described in more detail.

2.2.1 Engine Dynamics

The engine dynamics have two states; the engine speed (ω_e) and the mass of air in the intake manifold (m_a). By applying Newton's second law of motion to the engine and the conservation of mass to the intake manifold, the differential equations describing ω_e and m_a are

$$I_e\,\dot{\omega}_e = T_{net}(\omega_e, P_{man}) - T_{pump}(\omega_e, \omega_t) \tag{2.1}$$

$$\dot{m}_a = MAX\,TC(\alpha)\,PRI(P_{man}/P_{atm}) - \dot{m}_{ao}(\omega_e, P_{man}) \tag{2.2}$$

$$P_{man}\,V_{man} = R_{air}\,T_{man}\,m_a \tag{2.3}$$

The last algebraic equation shows the relationship between m_a and the pressure of the intake manifold (P_{man}). This relation holds under the assumptions that the temperature of the intake manifold is constant and the air acts as an ideal gas.

Notice that the net engine torque ($T_{net}(\omega_e, P_{man})$) and mass flow rate of air out of the intake manifold($\dot{m}_{ao}(\omega_e, P_{man})$), are both nonlinear functions of the engine speed (ω_e) and the intake

manifold pressure (P_{man}). Similarly, the pump torque ($T_{pump}(\omega_e, \omega_t)$) is a function of ω_e and the turbine speed of the torque converter (ω_t). These functions are obtained through experimentation and are usually provided by the engine manufacturers as a static map (Cho and J.K. 1989). The current value is then calculated via a table-lookup and interpolation of the map. The format of the engine map used for simulation and control is shown in Table 2.1, while the map for the pump torque is explained in Section 2.2.3.

ω_e	T_{net}	$\dot{m}_{ao}$	P_{man}	α
$\vdots$	$\vdots$	$\vdots$	$\vdots$	$\vdots$

Table 2.1: Engine Map Format

Similarly, the mass flow rate of air into the intake manifold is also an empirical nonlinear mapping expressed by the first term of the manifold dynamics (Cho and J.K. 1989). The nonlinear functions $TC(\alpha)$ and $PRI(P_{man}/P_{atm})$ reflect the influence of the throttle body geometry and pressure difference upon the air flow, respectively. Both are also represented as static maps and are calculated via table-lookup and interpolation. The constant coefficient MAX represents the maximum flow possible into the intake manifold.

Finally, the throttle actuator dynamics are represented as an additional first order system described by

$$\tau_e \, \dot{\alpha} + \alpha = \alpha_c$$

2.2.2 Torque Converter

The torque converter is composed of one state, the turbine speed (ω_t). Again, using Newton's second law, the differential equation describing the dynamics of ω_t is

$$I_t \, \dot{\omega}_t = T_{turb}(\omega_e, \omega_t) - R^* T_{shaft}$$

The torque converter's fluidic coupling is also modeled as a nonlinear function of the engine and wheel speeds (ω_e and ω_t) (McMahon 1994). The function is represented as a pair of second order polynomials, with the outputs of pump and turbine torque (T_{pump} and T_{turb}). These polynomials have the following form:

$$T_{pump} = \begin{cases} a_0\omega_e^2 + a_1\omega_e\omega_t + a_2\omega_t^2 & \text{if } \frac{\omega_t}{\omega_e} < 0.9 \\ c_0\omega_e^2 + c_1\omega_e\omega_t + c_2\omega_t^2 & \text{otherwise} \end{cases}$$

$$T_{turb} = \begin{cases} b_0\omega_e^2 + b_1\omega_e\omega_t + b_2\omega_t^2 & \text{if } \frac{\omega_t}{\omega_e} < 0.9 \\ c_0\omega_e^2 + c_1\omega_e\omega_t + c_2\omega_t^2 & \text{otherwise} \end{cases}$$

where the coefficients a_i, b_i, and c_i model the input-output relationship at lower and higher speed ratios, respectively. These coefficients are experimentally determined for a specific torque converter.

The torque converter also exhibits a discrete change of operating mode called *locking*. In the locked mode, the pump and turbine shafts of the torque converter become mechanically linked in order to reduce losses through the fluidic coupling in higher gears (typically third and fourth gear). When the torque converter is locked, the pump and turbine torques become equal and the

powertrain dynamics reduce to a second order system. The reduced order dynamics can be written as:

$$
\begin{aligned}
(I_e + I_t)\,\dot{\omega}_e &= T_{net}(\omega_e, P_{man}) - R^* T_{shaft} && (2.4)\\
\dot{m}_a &= MAX\,TC(\alpha)\,PRI(P_{man}/P_{atm}) - \dot{m}_{ao}(\omega_e, P_{man}) && (2.5)\\
P_{man}\,V_{man} &= R_{air}\,T_{man}\,m_a && (2.6)\\
\omega_e &= \omega_t && (2.7)
\end{aligned}
$$

2.2.3 Transmission

The transmission consists of a simple static model of the automated gear shift routine. The current gear ratio (R_g) is modeled as another table lookup function dependent on the vehicle speed ($\dot{x}$) and the throttle angle (α). Gear shift schedule charts are also provided by the vehicle manufacturers. Gear shift schedules are in the form shown in Table 2.2:

Shift up from i-th gear	α	$\dot{x}$
$\vdots$	$\vdots$	$\vdots$
Shift down from i-th gear	α	$\dot{x}$
$\vdots$	$\vdots$	$\vdots$

Table 2.2: Gear Shift Chart Format

2.3 Brake System

While the powertrain can increase the tractive forces generated via the commanded throttle angle, it has only limited ability to decrease these forces. Therefore, the braking system fills this deficiency by allowing direct control of the wheel decelerations. Two models of the braking system are available for the user which are dependent on the type of control input; one model assumes direct control of the master cylinder pressure, while the other assumes control of the brake pedal.

2.3.1 Direct Master Cylinder Pressure Control

For automated longitudinal operations, the vacuum booster is bypassed, since it is a source of a large "pure" time delay and lag (Gerdes 1996). Therefore, direct control of the brake fluid pressure within the master cylinder (P_{mc}) is attained through an additional intermediate cylinder piston controlled by the commanded pressure feed (P_{mcc}) (Maciuca 1997).

These brake system hydraulics are modeled by an experimentally determined capacitance , while the wheel cylinder pressure ($P_{wheel}(V_{mc})$) is a nonlinear function of the volume of fluid entering the master cylinder (V_{mc}) as follows

$$\dot{V}_{mc} = C_q \sqrt{|P_{mc} + P_{mcc} - P_{wheel}(V_{mc})|}\ \text{sign}(P_{mc} + P_{mcc} - P_{wheel}(V_{mc}))$$

The capacitance curve, $P_{wheel}(V_{mc})$, may be approximated as a cubic polynomial of V_{mc} and such cubic curves are typical of brake system hydraulics (Maciuca 1997).

Finally, the wheel cylinder pressure is related linearly to the brake torque by the following equation

$$T_{br} = K_b P_{wheel}(V_{mc})$$

Losses in the brake torque from warping in the brake rotors, uneven pad wear, etc. are contained within K_b. Therefore, K_b is highly uncertain and it can vary due to age, brake pad temperature, and even imperceptible manufacturing differences. Empirical data (Maciuca 1997) has shown that values of $K_b \leq 0.9$ are typical.

2.3.2 Master Cylinder Pressure Control via the Vacuum Booster

Alternatively, an input braking force (F_{in}) can be applied at the brake pedal. This input force is subsequently amplified by the vacuum booster before affecting the master cylinder piston. This alternative input is more realistic when a human driver model is used as the vehicle controller.

The vacuum booster is essentially a hydraulic amplifier composed of two chambers; the apply chamber and the vacuum chamber. The pressure difference between these two chambers causes the amplification of braking force. There are two states associated with the vacuum booster; the mass of air in the apply chamber and the mass of air in the vacuum chamber. There are also three discrete stages of operation of the vacuum booster; apply, hold and release. The stage of operation depends on the pedal input and the state of the vacuum booster. The output force of the vacuum booster in turn pushes the piston in the master cylinder, affecting the pressure and volume of the master cylinder. For a detailed explanation of the operation of a vacuum booster, the interested reader is referred to (Gerdes 1996).

The governing equations for the transmission of F_{in} to P_{mc} through the vacuum booster are:

$$\begin{aligned}
P_{app} &= \frac{m_{apply} R T_{MAN}}{(V_{ao} + A_d x_{mc})} \\
P_{vac} &= \frac{m_{vacuum} R T_{MAN}}{(V_{vo} - A_d x_{mc})} \\
F_d &= A_d (P_{app} - P_{vac}) \\
F_{rs} &= F_{rso} + K_{rs} x_{mc} \\
F_{out} &= \begin{cases} F_d + F_{in} - F_{rs} & F_d + F_{in} - F_{rs} \geq 0 \\ 0 & \text{otherwise} \end{cases}
\end{aligned}$$

F_{apply} and $F_{release}$ are functions of F_{in} and vacuum booster output force (F_{out}). They delimit

the stages of operation of the vacuum booster.

$$
\begin{aligned}
\dot{m}_{vm} &= \begin{cases} -C_{vm}(P_{vac} - P_{man} - P_o) & P_{vac} \geq P_{man} + P_o \\ 0 & \text{otherwise} \end{cases} \\
\text{stage} &= \begin{cases} \text{release} & F_{in} < F_{release} \\ \text{hold} & F_{release} \leq F_{in} < F_{apply} \\ \text{apply} & \text{otherwise} \end{cases} \\
\dot{m}_{apply} &= \begin{cases} C_{av}(P_{vac} - P_{app}) & \text{stage = release} \\ C_{leak}(P_{vac} - P_{app}) & \text{stage = hold} \\ C_{aa}(P_{ATM} - P_{app}) & \text{stage = apply} \end{cases} \\
\dot{m}_{vacuum} &= \begin{cases} \dot{m}_{vm} + C_{av}(P_{app} - P_{vac}) & \text{stage = release} \\ \dot{m}_{vm} + C_{leak}(P_{app} - P_{vac}) & \text{stage = hold} \\ \dot{m}_{vm} & \text{stage = apply} \end{cases} \\
F_{cs} &= F_{cso} + K_{cs}x_{mc} \\
P_{mc} &= \begin{cases} \frac{(F_{out} - F_{cs} - F_{cf})}{A_{mc}} & F_{out} \geq F_{cs} + F_{cf} \\ 0 & \text{otherwise} \end{cases} \\
V_{mc} &= A_{mc}x_{mc} \\
\dot{V}_{mc} &= C_q\sqrt{|P_{mc} - P_{wheel}(V_{mc})|}\ \text{sign}(P_{mc} - P_{wheel}(V_{mc})) \\
T_{br} &= K_b P_{wheel}(V_{mc})
\end{aligned}
$$

where the last equations are identical to those found in the previous description of direct master cylinder pressure control.

2.4 Suspension System

The suspension system provides a well damped connection between the sprung and unsprung masses in order to improve ride quality and vehicle handling. The vehicle's suspension is modeled as a nonlinear hardening spring in parallel with a linear shock absorber. The suspension deflections (d) and deflection rates ($\dot{d}$) are obtained from the kinematics of the suspension system represented in the following equations

$$
\begin{aligned}
d_{fl} &= H_0 - z + (H_5 + l_1)\theta - \frac{s_{b1}\phi}{2} \\
d_{fr} &= H_0 - z + (H_5 + l_1)\theta + \frac{s_{b1}\phi}{2} \\
d_{rl} &= H_0 - z + (H_5 - l_2)\theta - \frac{s_{b2}\phi}{2} \\
d_{rr} &= H_0 - z + (H_5 - l_2)\theta + \frac{s_{b2}\phi}{2} \\
\dot{d}_{fl} &= -\dot{z} + (H_5 + l_1)\dot{\theta} - \frac{s_{b1}\dot{\phi}}{2} \\
\dot{d}_{fr} &= -\dot{z} + (H_5 + l_1)\dot{\theta} + \frac{s_{b1}\dot{\phi}}{2} \\
\dot{d}_{rl} &= -\dot{z} + (H_5 - l_2)\dot{\theta} - \frac{s_{b2}\dot{\phi}}{2} \\
\dot{d}_{rr} &= -\dot{z} + (H_5 - l_2)\dot{\theta} + \frac{s_{b2}\dot{\phi}}{2}
\end{aligned}
$$

Subsequently, the suspension forces (F_{pi}) given by Newton's Second Law are

$$
\begin{aligned}
F_1 &= K_1 d_{fl}(1 + C_2 d_{fl}^4) + C_i \dot{d}_{fl} + \frac{Mgl_2}{l_1 + l_2} \\
F_2 &= K_1 d_{fr}(1 + C_2 d_{fr}^4) + C_i \dot{d}_{fr} + \frac{Mgl_2}{l_1 + l_2} \\
F_3 &= K_2 d_{rl}(1 + C_2 d_{rl}^4) + C_i \dot{d}_{rl} + \frac{Mgl_1}{l_1 + l_2} \\
F_4 &= K_2 d_{rr}(1 + C_2 d_{rr}^4) + C_i \dot{d}_{rr} + \frac{Mgl_1}{l_1 + l_2} \\
F_{pi} &= \begin{cases} 0 & F_i \leq 0 \\ \frac{Mg}{2} & F_i \geq \frac{Mg}{2} \\ F_i & \text{otherwise} \end{cases}
\end{aligned}
$$

2.5 Wheel Dynamics

The wheel dynamics are obtained by applying Newton's second law of motion to the wheels. A free body diagram of an individual wheel is given in Figure 2.3. The angular speed of wheel *i* (ω_{wi}), is described by the following differential equation

$$I_{wi}\dot{\omega}_{wi} = \beta_i T_{shaft} - hF_{txi} - T_{bri} sign(\omega_{wi})$$

and the average wheel speed measured by the speedometer is

$$\omega_{av} = \sum_{i=1}^{4} \beta_i \omega_{wi}$$

The inclusion of different types of drive train can be incorporated into the wheel dynamics with the parameter β_i. For example, for a front-drive vehicle, the front wheels would have $\beta_1 = \beta_2 = 0.5$, while the rear wheels would have $\beta_3 = \beta_4 = 0$.

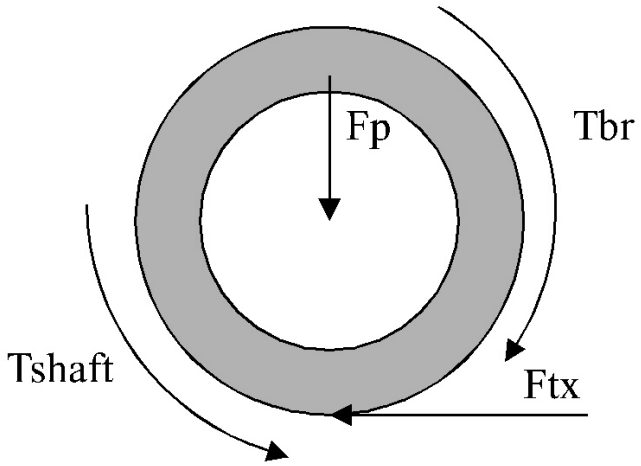

Figure 2.3: Free-body diagram of a wheel

2.6 Tire Model

The tractive forces necessary to move the vehicle in the lateral and longitudinal directions are estimated by a tire model. Various tire models exist in the vehicle dynamics literature, however the current model used was developed by Bakker and Pacjeka (Bakker *et al.* 1987b). This model is also more commonly known as the *magic tire formula*. This tire model describes the longitudinal and lateral tractive forces as a nonlinear function of longitudinal tire slip (λ), slip angle (ζ), normal force acting on the wheel (F_p), and the condition of the road and tire interface (RC).

To determine the tractive forces, the velocity of each wheel must be found with respect to a coordinate frame aligned with the wheel. A diagram of the coordinate frames is shown in Figure 2.4.

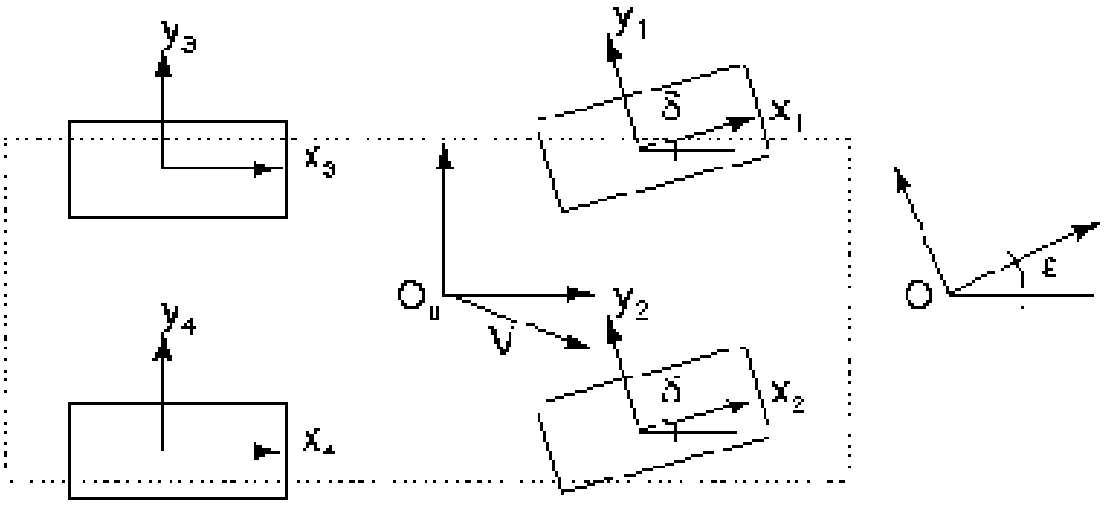

Figure 2.4: Wheel coordinate frames in relation to unsprung mass (O_u) and global(O) coordinate frames

The velocities of each tire are determined by the following algebraic equations

$$
\begin{aligned}
v_{x1} &= \dot{x} - \frac{s_{b1}\dot{\epsilon}}{2} \qquad & v_{y1} &= \dot{y} + l_1\dot{\epsilon} \\
v_{x2} &= \dot{x} + \frac{s_{b1}\dot{\epsilon}}{2} \qquad & v_{y2} &= \dot{y} + l_1\dot{\epsilon} \\
v_{x3} &= \dot{x} - \frac{s_{b2}\dot{\epsilon}}{2} \qquad & v_{y3} &= \dot{y} - l_2\dot{\epsilon} \\
v_{x4} &= \dot{x} + \frac{s_{b2}\dot{\epsilon}}{2} \qquad & v_{y4} &= \dot{y} - l_2\dot{\epsilon}
\end{aligned}
$$

Once the velocities of each wheel are found, the longitudinal slip, slip angle, and tractive forces of tire *i* can be calculated using the following equations

$$
\lambda_i = 1 - \frac{\sqrt{v_{xi}^2 + v_{yi}^2}}{h_i \omega_{wi}} \qquad \zeta_i = \eta_i \delta - \tan^{-1}\left(\frac{v_{yi}}{v_{xi}}\right)
$$

$$
\begin{aligned}
F_{txi} &= F_{tx}(\lambda_i, \zeta_i, F_{pi}, \text{RC(skid number)}) \\
F_{tyi} &= F_{ty}(\lambda_i, \zeta_i, F_{pi}, \text{RC(skid number)})
\end{aligned}
$$

where F_{tx}, F_{ty} are functions determined by the tire model used and the specific tire which is being modeled.

Notice that different steering architectures can be implemented using the variable η_i. For example, for a front wheel steered vehicle, $\eta_1 = \eta_2 = 1, \eta_3 = \eta_4 = 0$. Alternatively, a vehicle equipped with four wheel steering, $\eta_1 = \eta_2 = \eta_3 = \eta_4 = 1$.

Chapter 3

Automated Longitudinal Control in Normal Mode

The first layer of the hierarchical control system is the *physical layer*. The physical layer is a set of longitudinal and lateral controllers which give actuator commands such that the vehicle tracks a desired acceleration trajectory provided by the regulation layer.

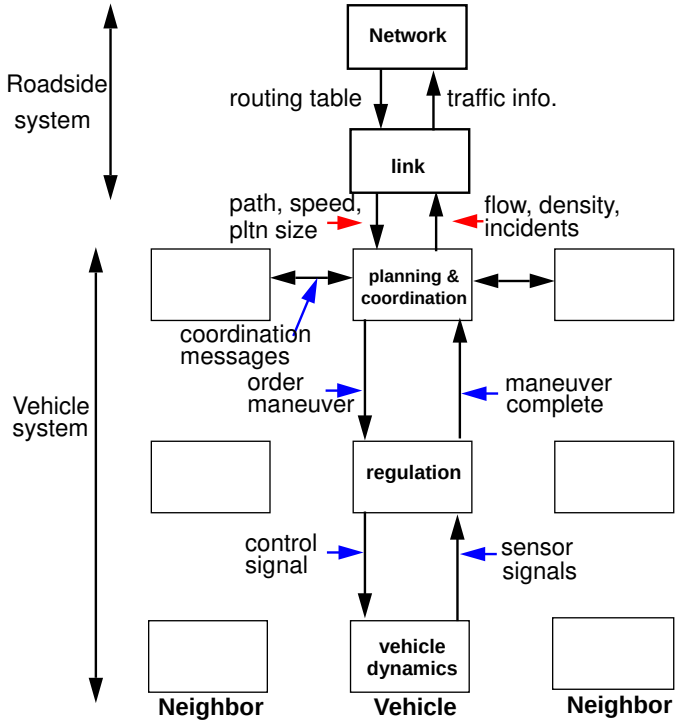

Figure 3.1: PATH AHS control architecture

3.1 Physical Layer Control System

The longitudinal controller at the physical layer is based on a nonlinear control technique called *sliding mode control*. While the details of this design technique are beyond the scope of this work,

the interested reader is referred to (Khalil 1996),(Slotine and Li 1991) for more information. This controller has also been successfully implemented and thoroughly tested on the experimental vehicles at PATH, and thus represents the default physical layer controller which will used for the remainder of this report.

The lateral control system is based on a "look-down" magnetic marker system to determine the lateral deviation of the vehicle from the center of the roadway. The goal of the lateral controller is to regulate the vehicle's lateral position about a desired path with respect to the road centerline. A description of the lateral control system is beyond the scope of this project, however the interested reader is referred to (Pham 1996; Patwardhan 1994b) for more detailed information.

The longitudinal control at the physical layer has several distinct control tasks, so a hierarchical control architecture is used to address each of these in turn. The hierarchical controller is composed of three levels of control as shown in Figure 3.2.

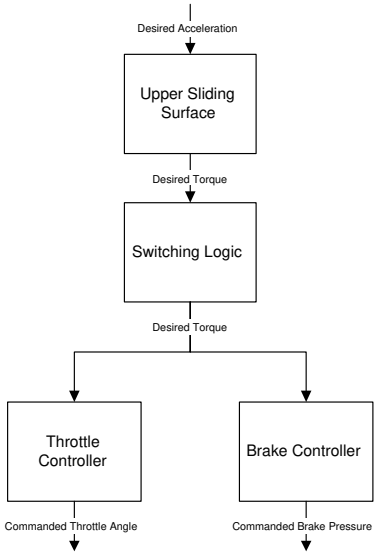

Figure 3.2: Physical layer of the longitudinal control hierarchy

At the top level, feedback linearization is used to determine the desired engine torque required to track the desired acceleration given by the regulation layer (Swaroop *et al.* 1996; Gerdes 1996). The middle level of the longitudinal controller is a switching logic which decides whether acceleration or braking is required based on the current state of the vehicle and the desired torque (Gerdes 1996). If acceleration is required, the desired torque is subsequently passed on the the throttle controller to determine the throttle actuator command. Similarly, if deceleration is required, the desired torque is subsequently passed on the the brake controller to determine the brake actuator command (Maciuca 1997). Both of these bottom level controllers use a sliding mode control algorithm to meet the desired torque. This overall control approach of cascading sliding mode controllers is known as *multiple sliding surface control*, or *dynamic sliding surface control* (Swaroop *et al.* 1996).

The remaining parts of this section will cover the vehicle model used for the controller design, the key relations describing the resulting three levels of the physical layer controller, and the sensor's and actuator's required for the given controller.

3.1.1 Simplified Vehicle Model for Control

While the vehicle model presented in Chapter 2 is appropriate for simulation, it is far too complex for control system design. Therefore, a simplified longitudinal vehicle model is used to develop the longitudinal controller.

The vehicle model can be simplified by making the following assumptions:

1. The slip between the tires and the road surface is negligible.
2. The torque converter is locked.
3. The actuator dynamics are fast compared to the vehicle dynamics.

Under these assumptions, the longitudinal velocity of the vehicle $\dot{x}$ is proportionally related to the angular velocity of the engine ω_e through the gear ratio and tire radius as follows

$$\dot{x} = R^* h \omega_e$$

The dynamics relating engine speed ω_e to the net combustion torque T_{net}, brake torque T_{br}, and aerodynamic losses can be modeled by

$$J_e \dot{\omega}_e = T_{net}(m_a, \omega_e) - c_x R^{*3} h^3 \omega_e^2 - R^*(T_{rr} + T_{br}(P_{wheel}))$$

where J_e is the effective inertia of the engine, drive train and vehicle.

By applying the conservation of mass to the intake manifold, the mass of air in the manifold is defined by

$$\dot{m}_a = MAX\, TC(\alpha)\, PRI(m_a) + \dot{m}_{ao}(\omega_e, m_a)$$

3.1.2 Upper Level: Torque Control

The main goal of the longitudinal controller is to effectively linearize the vehicle dynamics through feedback such that the vehicle dynamics become

$$\ddot{x} = u_{isl}$$

where u_{isl} is the synthetic input, or desired acceleration, given by the regulation layer. This allows the designer to completely specify the dynamic behavior of the vehicle via the choice of the synthetic input. However, notice that direct control of $\ddot{x}$ is not possible since the control inputs (the throttle angle α and the brake pressure P_{wheel}) do not directly affect it. The control objective can only be achieved by controlling the net torque T_{net} and the brake torque T_{br}. In addition, the use of the brakes and throttle should be mutually exclusive to minimize actuator usage and wear and tear on the vehicle. Therefore, considering the net torque and brake torque as new *pseudo-inputs*, the goal above can be achieved by choosing

$$T_{net}(m_a, \omega_e) = \frac{J_e}{R^* h} u_{isl} + c_x R^{*3} h^3 \omega_e^2 + R^*(T_{rr} + T_{br}(P_{wheel}))$$

when throttle control is required and

$$T_{br}(P_{wheel}) = \frac{J_e}{R^* h} u_{isl} - T_{net}(m_a, \omega_e) + c_x R^{*3} h^3 \omega_e^2 + R^* T_{rr}$$

when the brakes are needed. These terms are not true control inputs, since dynamics exist between the torques and the actual control inputs, namely the throttle angle and brake pressure. Therefore, another level of control is required to attain these desired torques using the true control inputs. However, a methodology for choosing between throttle and brake control will be discussed next.

3.1.3 Middle Level: Switching Logic

As mentioned above, the throttle and brake commands should be mutually-exclusive to reduce actuation and system wear (ie. a human driver rarely uses both the throttle and brakes at the same time). However, some type of switching logic is required to decide when each type of control should be used (Gerdes 1996). Intuitively, the brakes should be used only when the natural braking forces on the vehicle, such as aerodynamic drag, rolling resistance, and engine braking, are not sufficient to achieve the desired synthetic input. Written more mathematically, this idea can be expressed as

$$\begin{aligned} u_{isl} - a_{res} > \lambda_u &\Rightarrow throttle \\ u_{isl} - a_{res} < \lambda_l &\Rightarrow brake \\ \lambda_l \leq u_{isl} - a_{res} \leq \lambda_u &\Rightarrow wait \end{aligned}$$

where a hysteresis region has been added to reduce chattering around the switching line $u_{isl} - a_{res} = 0$ (Gerdes 1996). Also, the residual acceleration a_{res} of the vehicle is

$$a_{res} = \frac{R^* h}{J_e}(T_{engbrk}(m_a, \omega_e) - c_x R^{*3} h^3 \omega_e^2 - R^*(T_{rr} + T_{br}(P_{wheel}))$$

3.1.4 Lower Level: Throttle Control

Once the decision has been made to use the throttle, the desired value of the pseudo-input $T_{net}(m_a, \omega_e)$ is clearly defined by

$$T_{net}(\bar{m}_a, \omega_e) = \frac{J_e}{R^* h} u_{isl} + c_x R^{*3} h^3 \omega_e^2 + R^*(T_{rr} + T_{br}(P_{wheel}))$$

where $\bar{m}_a$ is the mass of air in the intake manifold necessary to achieve this desired net torque, which can be determined explicitly by inverting the nonlinearity $T_{net}(\bar{m}_a, \omega_e)$. Now, we will design a dynamic surface controller (Swaroop *et al.* 1996) to force m_a to track $\bar{m}_a$, which subsequently forces $\ddot{x}$ to track u_{isl}. Let's define the surface S_1 such that

$$S_1 = m_a - m_{a,des}$$

Then choosing the surface dynamics as

$$\dot{S}_1 = -K_1 S$$

and using the manifold dynamics presented in Section 3.1.1 the following relationships for the commanded throttle angle α_c and the desired mass of air $m_{a,des}$ can be determined

$$\begin{aligned} \alpha_c &= TC^{-1}\left(\frac{\dot{m}a_o(m_a, \omega_e) + \dot{m}_{a,des} - K_1 S_1}{MAX\ PRI(m_a)}\right) \\ \tau_1 \dot{m}_{a,des} + m_{a,des} &= \bar{m}_a \end{aligned}$$

A similar derivation will now be performed for the accompanying brake controller.

3.1.5 Lower Level: Brake Control

Once the decision has been made to use the brake, the desired value of the pseudo input $T_{br}(P_wheel)$ is clearly defined by

$$T_{br}(\bar{P}_{wheel}) = \frac{J_e}{R^* h} u_{isl} - T_{net}(m_a, \omega_e) + c_x R^{*3} h^3 \omega_e^2 + R^* T_{rr}$$

Using the direct master cylinder controlled brake model presented in Section 2.3.1, the required brake pressure at the wheel $\bar{P}_{wheel}$ are found to be

$$\bar{P}_{wheel} = \frac{1}{K_b}(\frac{J_e}{R^* h} u_{isl} - T_{net}(m_a, \omega_e) + c_x R^{*3} h^3 \omega_e^2 + R^* T_{rr} + P_{po})$$

Now, define the surface S_2 to be

$$S_2 = P_{wheel} - P_{wheel,des}$$

and the surface dynamics to satisfy

$$\dot{S}_2 = -K_2 S$$

then the resulting commanded master cylinder pressure P_{mcc} and the desired brake pressure at the wheel $P_{wheel,des}$ is described by

$$\begin{aligned} P_{mcc} &= \begin{cases} P_{wheel} + \Delta_{pb} & \text{if } (\dot{P}_{wheel,des} - K_2 S_2) > 0 \\ P_{wheel} - \Delta_{pb} & \text{otherwise} \end{cases} \\ \Delta_{pb} &= \frac{(\dot{P}_{wheel,des} - K_2 S_2)^2}{C_q^2} \\ \tau_2 \dot{P}_{wheel,des} + P_{wheel,des} &= \bar{P}_{wheel} \end{aligned}$$

3.1.6 Required Sensors and Actuators

Having reviewed the controller design, there are seven sensors and two actuators required for the longitudinal controller. In addition, a communication system will be required to receive information about the lead and previous vehicles in the platoon. The following table summarizes the sensors and actuators which are required. In addition, the standard deviation of normally distributed noise for each of the sensors after filtering is also included in the table, as well as the average time constants for first order actuator dynamics.

3.2 Regulation Layer Control System

This chapter discusses the derivation of the controller for the regulation layer, the derivation of an observer for the lead car, and a proof of stability for the controller. A complete derivation of a previous controller for the regulation layer is given in (Li *et al.* 1997). The derivation that follows is very similar to this previous work, with the following important differences:

- The new controller assumes that the acceleration of the car can be controlled directly. This is a change from the previous controller, where the jerk was the parameter that could be controlled. This modification reflects the controller onboard the automated cars that are being designed and tested by PATH engineers.

Table 3.1: Sensor and Actuator Characteristics

Sensors & Actuators	Typical Variance
Radar	2.5 cm in range, no noise assumed in range rate
Accelerometer	0.1 m/sec^2
Wheel Speed Sensor	0.03 m/sec
Throttle Angle Sensor	0.1 degrees
Brake Pressure Sensor	70 KPa
Manifold Pressure Sensor	0.25 KPa
Engine Speed Sensor	1 rpm
Throttle Actuator (Stepper Motor)	0.01 sec
Brake Actuator (Hydraulic System)	0.1 sec

- A full order observer is presented in Section 3.2.2. This observer is different from the observer introduced in (Li *et al.* 1997) because the position of the lead car is not included in the analysis. This reduces the complexity of the observer because the absolute position of the lead car does not need to be explicitly known.

These two major differences are highlighted in the following chapters, which are the theoretical basis for the regulation layer controller.

3.2.1 Controller Derivation

The objective of the regulation layer controller is to keep a vehicle traveling in the highway according with the conditions of relative velocity and relative spacing associated with a given maneuver. The next higher layer in the automated highway hierarchy, the coordination layer, issues commands that select the specific maneuver such as join, follow, or split. When there is a change of maneuver, the automated vehicle's regulation controller attempts to switch from the conditions associated with the present maneuver to the conditions associated with the new one in a quick and safe manner. To accomplish this task, the regulation layer controller tries to follow a desired velocity profile. Calculation of the desired velocity profile depends on three items: (1) the current maneuver, (2) the relative spacing between the trail car and a lead car, and (3) the velocity of a lead car.

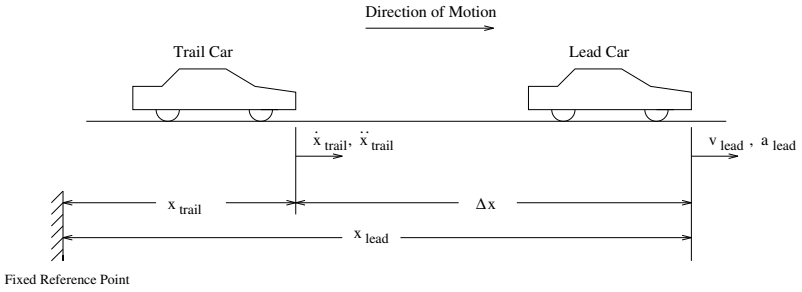

Figure 3.3: Geometry for controller derivation.

Figure 3.3 shows the important geometrical parameters for the derivation. In this analysis, the trail car is assumed to be the automated car that is the target of the controller's action, and the lead

car is the car that is directly ahead of the trail car in the same highway lane. Variables associated with the trail car are denoted with the subscript *trail*; likewise, variables associated with the lead car are indicated with the subscript *lead*. Also, derivatives with respect to time are indicated by a dot above a given variable.

The basis for the controller algorithm is to minimize the error between the trail car's velocity, $\dot{x}_{lead}$, and the desired velocity, $v_d(\Delta x, v_{lead})$, which is a function of the relative spacing between the trail car and lead car Δx and v_{lead} is the lead car velocity. It is clear from Figure 3.3 that the relative spacing is

$$\Delta x = x_{lead} - x_{trail}.$$

If we define the velocity error *e* by

$$e := \dot{x}_{trail} - v_d(\Delta x, v_{lead}). \tag{3.1}$$

then taking the derivative of the error with respect to time yields

$$\dot{e} = \ddot{x}_{trail} - \left(\frac{\partial v_d}{\partial \Delta x} \quad \frac{\partial v_d}{\partial v_{lead}} \right) \begin{pmatrix} v_{lead} - \dot{x}_{trail} \\ \dot{v}_{lead} \end{pmatrix}. \tag{3.2}$$

Assuming that the goal is to drive the error to zero exponentially, an appropriate expression for the closed loop error dynamics is

$$\dot{e} = -\lambda_1 e \tag{3.3}$$

Substituting this expression into Eq. (3.2) and solving for the trail car's acceleration results in the following equation:

$$\ddot{x}_{trail} := -\lambda_1 e + \left(\frac{\partial v_d}{\partial \Delta x} \quad \frac{\partial v_d}{\partial v_{lead}} \right) \begin{pmatrix} v_{lead} - \dot{x}_{trail} \\ a_{lead} \end{pmatrix}, \tag{3.4}$$

This equation would drive the velocity error to zero exponentially; unfortunately, the lead car's acceleration is not known exactly. If instead, it is assumed that an estimate of the lead car's acceleration is known[1], then the following is an acceptable control law for the trail car acceleration:

$$\ddot{x}_{trail} := \Gamma(\Delta x, v_{lead}, \dot{x}_{trail}, \hat{a}_{lead}) = -\lambda_1 e + \left(\frac{\partial v_d}{\partial \Delta x} \quad \frac{\partial v_d}{\partial v_{lead}} \right) \begin{pmatrix} v_{lead} - \dot{x}_{trail} \\ \hat{a}_{lead} \end{pmatrix}, \tag{3.5}$$

Note that the last term involves the estimate of the lead car's acceleration, $\hat{a}_{lead}$, instead of the true acceleration. In the next section, an observer for the lead car's acceleration will be introduced.

The dynamics for the velocity error *e* are easily shown to be

$$\dot{e} = -\lambda_1 e - \frac{\partial v_d}{\partial v_{lead}} \tilde{a}_{lead}, \tag{3.6}$$

where $\tilde{a}_{lead}$ is the estimation error for the lead car acceleration,

$$\tilde{a}_{lead} := a_{lead} - \hat{a}_{lead}. \tag{3.7}$$

Thus so long as the estimation error remains small, the error approaches zero approximately exponentially. The stability of this solution will be investigated further in Section 3.2.3.

[1]This approach is known as back-stepping (Krstic *et al.* 1995).

3.2.2 Observer for Lead Car Motion

An estimate for the lead car acceleration is necessary for the proposed controller. Assuming that the lead car velocity v_{lead} is known from sensor data, the following is the derivation of a full order observer for the lead car acceleration.

The lead car dynamics are given by

$$\frac{d^3}{dt^3}x_{lead} = \dot{a}_{lead}(t), \tag{3.8}$$

where a_{lead} is the acceleration input to the lead car. Written in state space form where the state matrix is $\mathbf{x} = \begin{pmatrix} v_{lead} & a_{lead} \end{pmatrix}^T$ the above equation becomes

$$\dot{\mathbf{x}} = A\mathbf{x} + B\dot{a}_{lead}(t). \tag{3.9}$$

where

$$A := \begin{pmatrix} 0 & 1 \\ 0 & 0 \end{pmatrix}, \qquad B := \begin{pmatrix} 0 \\ 1 \end{pmatrix}. \tag{3.10}$$

Also, since the only variable assumed to be known by the trail car is the lead car velocity, the equation for the sensor output is

$$y = C\mathbf{x}, \tag{3.11}$$

where

$$C := \begin{pmatrix} 1 & 0 \end{pmatrix}. \tag{3.12}$$

A full order observer for the state $\mathbf{x}$ is

$$\dot{\hat{\mathbf{x}}} = A\hat{\mathbf{x}} + L(y - C\hat{\mathbf{x}}) + \mathbf{q}(t), \tag{3.13}$$

where $\hat{\mathbf{x}}$ is the state estimate, L is the observer gain matrix, and $\mathbf{q}(t)$ is a tuning function to be determined in the stability analysis. This is a standard full order observer with the addition of one term, $\mathbf{q}(t)$, which accounts for the nonlinearities inherent in the system. By subtracting Eq. (3.13) from Eq. (3.9), the dynamics for the state estimator error, $\tilde{\mathbf{x}} = \mathbf{x} - \hat{\mathbf{x}}$, is found to be

$$\dot{\tilde{\mathbf{x}}} = (A - LC)\tilde{\mathbf{x}} + B\dot{a}_{lead}(t) - \mathbf{q}(t). \tag{3.14}$$

If both $a_{lead}(t)$ and $\mathbf{q}(t)$ remain bounded, the state estimates will approach the actual states so long as the both of the eigenvalues of $A_F \equiv (A - LC)$ have negative real components. A simple calculation shows that this occurs when the components of L are both positive.

3.2.3 Stability Analysis

Since the controller involves the estimate of the lead car acceleration, which is calculated by the full order observer, the dynamic responses of the controller and the observer are coupled. Consider the following candidate for a Lyapunov function:

$$V(e, \tilde{x}_{lead}) = \frac{1}{2}Qe^2 + \frac{1}{2}\gamma\tilde{\mathbf{x}}_{lead}^T P\tilde{\mathbf{x}}_{lead}, \tag{3.15}$$

where Q and γ are both positive constants and P is a positive definite matrix. This candidate function includes terms involving both the controller error e and the observer error $\tilde{x}$. The most difficult part of this analysis is the choice of P such that it satisfies the relationship

$$A_F{}^T P + P A_F = -2C \tag{3.16}$$

where C is also a positive definite matrix. This relationship is necessary for proving that V is indeed a Lyapunov function. Prior to discussing P further, several other derivations are required.

Consider the real decomposition of A_F,

$$A_F = T \Lambda T^{-1}, \tag{3.17}$$

where T is real and invertible and the diagonal of Λ contains the real parts of the eigenvalues of A_F. Λ can be further decomposed into two components,

$$\Lambda = \Lambda_1 + \Lambda_2, \tag{3.18}$$

where Λ_1 is symmetric (i.e. $\Lambda_1 = \Lambda_1{}^T$) and Λ_2 is skew-symmetric (i.e. $\Lambda_2 = -\Lambda_2{}^T$).

One possibility for the choice of P is

$$P = (T^{-1})^T T^{-1}, \tag{3.19}$$

where T is the matrix introduced above. In this case, we find that the matrix C that satisfies Eq. (3.16) is

$$C = -(T^{-1})^T \Lambda_1 T^{-1}, \tag{3.20}$$

which is positive definite if every diagonal element of the matrix Λ_1 is negative. Since the diagonal elements of Λ_1 are the real parts of the eigenvalues of A_F, C is positive definite if the full-order observer state matrix A_F has stable eigenvalues. Thus choosing P according to Eq. (3.19) guarantees a positive definite solution to C in Eq. (3.16) given an appropriate full order observer. This fact is essential in completing the next portion of the analysis.

For the function V to be an acceptable Lyapunov function, its derivative with respect to time, $\dot{V}$, must be negative definite. Taking the time derivative of Eq. (3.15), and using the relationship between P and C given in Eq. (3.16), yields

$$\dot{V} = -\lambda_1 Q e^2 - \gamma \tilde{\mathbf{x}}_{lead}^T C \tilde{\mathbf{x}}_{lead} + \gamma \tilde{\mathbf{x}}_{lead}^T P B \dot{a}_{lead}(t) - Qe \frac{\partial v_d}{\partial v_{lead}} \begin{pmatrix} 0 & 1 \end{pmatrix} \tilde{\mathbf{x}}_{lead} - \gamma \mathbf{q}^T P \tilde{\mathbf{x}}_{lead}. \tag{3.21}$$

Because the fourth term involves $\frac{\partial v_d}{\partial v_{lead}}$, a nonlinear function of Δx and v_{lead}, it is convenient to choose the tuning function $\mathbf{q}$ such that the fourth term is eliminated from the equation. Thus, an appropriate choice for $\mathbf{q}$ is

$$\mathbf{q} = \frac{Qe}{\gamma} \frac{\partial v_d}{\partial v_{lead}} P^{-1} \begin{pmatrix} 0 \\ 1 \end{pmatrix}, \tag{3.22}$$

Substituting this expression into the equation for $\dot{V}$ yields

$$\dot{V} = -\lambda_1 Q e^2 - \gamma \tilde{\mathbf{x}}_{lead}^T C \tilde{\mathbf{x}}_{lead} + \gamma \tilde{\mathbf{x}}_{lead}^T P B \dot{a}_{lead}(t). \tag{3.23}$$

A derivation that closely follows the methods presented in (Li *et al.* 1997) shows that for any initial condition $e(0)$, and for any $\epsilon > 0$, there is a time T_1 such that if $t \geq T_1$ then

$$\sqrt{\frac{Q}{2}} |e(t)| \leq V^{\frac{1}{2}}(t) \leq \frac{j_{max}}{\zeta} \sqrt{\frac{\delta}{\gamma}} (1 + \epsilon), \tag{3.24}$$

where

$$|\dot{u}| \leq j_{max},$$

and

$$\delta := 2P_{\cdot 2}^T P^{-1} P_{\cdot 2}\,,$$

where $P_{\cdot 2}$ is the second column of P.

Therefore, $|e(t)| \leq \frac{j_{max}}{\zeta}\sqrt{\frac{\delta\rho}{\gamma}}(1+\epsilon)$ after a long enough time.

3.3 Coordination Layer

The coordination layer design is based on those of SmartPATH design (Eskafi 1996) and the coordination protocol designs by Hsu *et al.* (1994) and Varaiya (1993). However, in this project we consider the communication design in details with the coordinated protocols among the vehicles and those between vehicles and roadside systems. Fig. 3.4 shows the general structure for the coordination layer scheme.

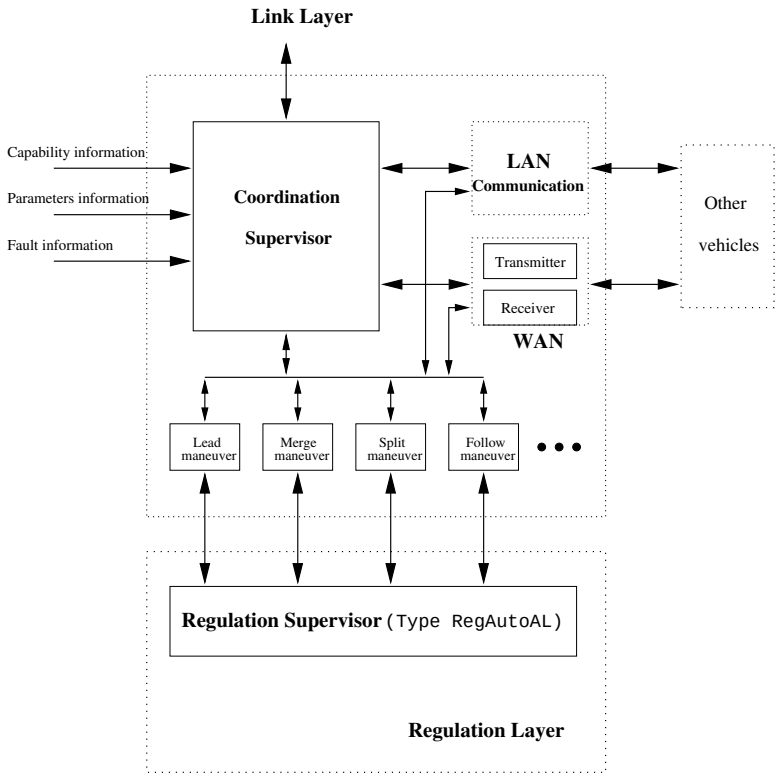

Figure 3.4: A schematic of coordination layer implementation

The coordination scheme consists of three parts: *coordination supervisor, maneuver protocols* and *communication design*. The coordination supervisor coordinates with different maneuver protocols and executes (initiates) maneuvers by communication with other vehicles or roadside systems. Basically it is discrete-event system. The maneuver protocols coordinates with other vehicles to guarantee the correctness and safety of each maneuver. There are two steady state maneuvers: *lead* and *follow* and some other transit maneuvers such as *split, merge, changelane* and

stoplight etc. The communication in the AHS system transmits the information among the vehicles and that between vehicles and roadside system. There are two types of communication among vehicles: local area networks (LAN) and wide area networks (WAN). The LAN is used to pass down the information of velocity and acceleration of leader and previous vehicle to the following vehicles in the platoon (Lindsey 1997) and the WAN is for passing the maneuver messages among the different vehicles. The roadside system also broadcasts the link layer information for each vehicle on that section of highway and this communication goes through vehicles and roadside system.

The coordination supervisor is similar to the regulation supervisor except that it initiates the maneuver protocols not regulation control laws. Based on the sensor information and the communication message it gets the coordination supervisor initiates a maneuver initiator or responder and after this maneuver has finished it returns to the maneuver before. For example, when the leader of platoon A receives link layer broadcasts and by the decision planner (we will discuss later in link layer section) it can initiate a *merge* maneuver initiator, then it sends out the `mergeReq` to the leader of previous platoon B. When the coordination supervisor of the leader of platoon B receives this message and initiate *merge* maneuver responder if there are no other maneuvers it involves. Then *merge* maneuver can start and after it finishes, the leader of platoon A becomes a follower with follower protocol and leader of platoon B becomes the leader of the new platoon. The finite state machine (FSM) diagram can be found in appendix A.4.3.

The maneuver protocol consists the coordinated actions among the vehicles involved in a maneuver. For most of transit maneuvers such as *merge, split, changelane* and *stoplight* there have two protocols needed for accomplishment of the maneuver: one is for maneuver initiator and another responder. However, for the steady state maneuver such as *lead* and *follow*, one protocol is enough. The maneuver initiator starts the maneuver and setups the communication with the responding vehicle. If it gets acknowledgment from the maneuver responder, then it commands the regulation supervisor and the actual maneuver executed; otherwise, the maneuver aborted. The details finite state machines for each maneuver protocols are also listed in appendix A.4.3.

Chapter 4

Fault Diagnostics for the Longitudinal Controller

Many types of fault diagnostic systems can be found in the literature, however techniques relying on a mathematical model of the monitored system are perhaps the most prevalent (Gertler 1988; Frank 1990; Isermann 1984). A model-based fault diagnostic system is typically composed of two main stages: the *residual generator* and the *residual processor*. The residual generator uses current knowledge about the state of the system to create a set of signals, called *residuals*, which are sensitive to the occurrence of faults. These residuals are a designer-defined set of comparisons between the various types of information known about the system, such as sensor measurements, command inputs, parameter estimates, as well as state and output estimates based on a model of the system (Beard 1971; Willsky 1976). The choice of which types of information to use depends on the system model, as well as the type of faults to be detected.

Although several types of fault models exist in the literature, this project considers only faults in the system components which can be modeled as additive terms to the residual vector. More technically, let the set of residuals be defined by the vector $r \in \Re^n$. In the case of no faults and an exact model of the monitored system, the vector $\mathbf{r}$ would be exactly zero. However, the residual vector has nonzero components when sensor noise and modeling uncertainties are considered. This nonzero value of the residual vector under nominal conditions will be denoted $r_{nom} \in \Re^n$. The relationship between these vectors and the faults to be considered can be written in the form

$$r(t) = r_{nom}(t) + F\mu(t) \tag{4.1}$$

where the last term represents the effects of the different faults which the diagnostic system will attempt to detect. Each fault is represented by two parts: the *fault signature* matrix $F \in \Re^{n \times p}$, whose columns describe the directional characteristics of the p faults, and the *fault mode* $\mu(t)$, which is a (possibly time-varying) vector describing the fault magnitude at time t. This project will only consider the occurrence of a single fault in the physical layer control components at any given time, thus restricting $\mu(t)$ to have only one nonzero element corresponding to the column of F which models the specific fault. Based on this fault model, the residual generator will use a combination of parity equations (Gertler 1988) and state observers (Frank 1990) to form the residual vector.

The second stage of the diagnostic system processes the residual vector to determine when a fault has occurred and to identify the faulty component based on the vector's characteristics. This processing is a complex task that can incorporate a variety of disciplines including change

detection (Basseville and Nikiforov 1993), pattern recognition (Bow 1992), and reasoning (Ross 1995). For the residual processor to correctly identify faults in the monitored system, the effect of each fault on the set of residuals must be unique. If this criteria is met, the faults are said to be *isolatable*. While this criteria theoretically guarantees that the identification of each fault is possible, the isolation of faults is generally not very robust to noise and unmodeled dynamics. A stronger condition can be achieved if the fault signatures $f \in Col(F)$ are linearly independent in the residual space. Diagnostic systems which satisfy this condition are said to have *structured* or *directional residuals* (Isermann 1997).

The remainder of this section will address the diagnosis of faults in the sensors and actuators at the physical layer of the automated control system using the framework described above. First, some theoretical results on nonlinear observers will be presented as background in Section 4.1. Section 4.2 will then describe the design of the residual generator, while the design of the residual processor is outlined in Section 4.3. Finally, simulation results for the complete system and some limited experimental results will be presented in Sections 4.4 and Sections 4.5, respectively.

4.1 Exponential Observer Design for Nonlinear Systems

For the diagnosis of faults in the longitudinal control components, the simplified nonlinear model presented in Section 3.1.1 can be used in the design of a nonlinear observer for the engine speed and mass of air in the intake manifold. Prior work in this project under MOU 288 used the techniques developed by Raghavan (Raghavan and Hedrick 1994) and Rajamani (Rajamani and Cho 1998) to design an observer gain matrix which stabilized the observer error dynamics. However, these techniques do not account for the case when the system nonlinearities aid in the stability of the error dynamics, and instead attempt to overpower the nonlinearity through the correction term. This overpowering of the nonlinearities leads to large observer gains and a corresponding increase in sensitivity to sensor noise. An alternative design methodology will be presented here which explicitly accounts for the system nonlinearities assisting in the observer stability through a sector constraint argument similar to that presented in (Banks 1981).

The system dynamics are assumed to be of the following form

$$\dot{x} = Ax + f(x) + Bu \tag{4.2}$$
$$y = Cx \tag{4.3}$$

while the proposed observer has the form

$$\dot{\hat{x}} = A\hat{x} + f(\hat{x}) + Bu + K(y - C\hat{x}) \tag{4.4}$$

Therefore, the error dynamics of the observed system are

$$e = x - \hat{x} \tag{4.5}$$
$$\dot{e} = (A - KC)e + \phi(e, t) \tag{4.6}$$
$$\phi(e, t) = f(x) - f(\hat{x}) \tag{4.7}$$

The following lemma derived from (Banks 1981) can be used prove the stability of the proposed observer.

Lemma 1 *If the system and the observer have the forms given in 4.2 and 4.4, the pair (A,C) is detectable, and the nonlinearity satisfies*

$$e^T \phi(e,t) \leq 0 \;\; \forall e, t$$

then there exists an observer gain matrix K such that the error dynamics can be made asymptotically stable.

Proof: The stated lemma is proven in a Lyapunov stability framework, rather than the more cumbersome version shown in (Banks 1981). First, consider the Lyapunov function candidate

$$V = \frac{1}{2} e^T e$$

This quadratic form is obviously a valid candidate Lyapunov function, so all that remains for the proof is to show that it's time derivative is strictly decreasing. Taking the time derivative of V,

$$\dot{V} = \frac{1}{2}(\dot{e}^T e + e^T \dot{e})$$

Substituting in the error dynamics and rearranging terms results in

$$\dot{V} = \frac{1}{2} e^T ((A - KC)^T + (A - KC))e + e^T \phi(e,t)$$

Using the assumption that $e^T \phi(e,t) \leq 0$, $\dot{V}$ can be bounded by

$$\dot{V} \leq \frac{1}{2} e^T ((A - KC)^T + (A - KC))e$$

Finally, notice that

$$\frac{1}{2}((A - KC)^T + (A - KC)) = (A - KC)_{sym}$$

where $(A - KC)_{sym}$ is the symmetric part of the matrix. And since the (A,C) pair is detectable there exists a gain matrix K which makes the all eigenvalues of the matrix $(A - KC)_{sym}$ have negative real parts. Therefore,

$$\dot{V} \leq -e^T (A - KC)_{sym} e < 0$$

when the matrix K chosen such that $\lambda(A - KC) < 0$. ■

Although the proof does not explicitly give a method for determining the gain matrix K, standard pole placement or iterative LMI techniques can be used for the single output and multiple output cases, respectively.

Furthermore, note that the lemma requires the system to have an explicit linear term and a nonlinear drift term $\phi(e,t)$ which satisfies a sector constraint. For systems whose dynamics do not contain an explicit linear term, the dynamics can be rewritten in the appropriate form by adding and subtracting a linear term, i.e.

$$\begin{aligned} \dot{x} &= \bar{f}(x) + Bu \\ &= Ax + (\bar{f}(x) - Ax) + Bu \\ &= Ax + f(x) + Bu \end{aligned}$$

Since the A matrix can be arbitrarily chosen, a reasonable question to ask is what is the best method to choose A? One intuitively appealing method for the case of observer design is to choose A such that $e^T\phi(e,t) \leq 0$ so that Lemma 1 can be readily applied. It is easy to show that if the system nonlinearity $\bar{f}(x)$ satisfies

$$(x-\hat{x})^T(\bar{f}(x)-\bar{f}(\hat{x})) \leq (x-\hat{x})^T A(x-\hat{x})$$

for all x and $\hat{x}$ and some matrix A, then $e^T\phi(e,t) \leq 0$. In fact, it is also relatively easy to show that all Lipschitz nonlinearities satisfy this constraint by choosing $A = \gamma I$ where γ is the Lipschitz constant. However, this constraint gives more information about the nonlinearities relation to the state than the simple norm bound expressed by the Lipschitz constant.

4.2 Residual Generator

The residual generator relies on ten sensors, intervehicle communication, and the throttle and brake actuator commands to form a residual vector which is sensitive to faults in all of the vehicle's sensors and actuators. The specific components which are monitored by this system include the magnetometer and the components listed in Table 3.1. Although the magnetometer is not directly used in the longitudinal controller, it must also be monitored because the magnetometer is used in the fault diagnostic system. Diagnosis of faults in the communications system are beyond the scope of this project, however several other PATH projects are addressing this issue (Sengupta 1999; Simsek *et al.* 1999). In addition to this raw information about the vehicle's condition, several observers have been designed to provide analytical redundancy for the physical components.

The remaining parts of this section will discuss the separate residuals that compose the residual vector, as well as the design of the state observers used.

4.2.1 Vehicle Speed Residuals

From the simplified vehicle model used for controller design, the vehicle, wheel, and engine speeds are proportionally related under the stated assumptions. So the wheel speed and engine speed measurements can be used to give the following estimates of the vehicle's speed

$$\begin{aligned} \hat{v}_1 &= h\omega_w \\ \hat{v}_2 &= hR^*\omega_e \end{aligned}$$

In addition, the speed measurement of the previous vehicle is known via communication for the automated controller, and the relative velocity is measured by the vehicle's radar. Therefore a third estimate of the vehicle speed is

$$\hat{v}_3 = v_{prev} + \dot{\delta}$$

The three basic comparisons of these estimates form the first part of the residual vector, described by

$$\begin{aligned} r_0 &= \hat{v}_1 - \hat{v}_2 \\ r_1 &= \hat{v}_3 - \hat{v}_1 \\ r_2 &= \hat{v}_3 - \hat{v}_2 \end{aligned}$$

4.2.2 Vehicle Spacing Residuals

Although the radar on the automated vehicle measures the range δ and range rate $\dot{\delta}$, some other measurement of the range must be available for the fault diagnostic system. Therefore a linear observer based on the vehicle's kinematics is proposed to obtain an estimate of intervehicle spacing. This observer relies on the magnetometers used by the lateral control system to count the number of magnetic markers passed by the current vehicle. In addition, the magnet count of the previous vehicle is known via the communication system. The resulting observer has the following form

$$\dot{\hat{\delta}} = h\omega_w - v_{prev} + K_{sp}[(n - n_{prev})L_{mag} + L_{car} - \hat{\delta}]$$

where n_{prev} and n are the magnet counts of the previous and current vehicle, respectively.

The stability of the observer can seen by determining the error dynamics for $\tilde{\delta} = \delta - \hat{\delta}$. Using the differential equation for the observer shown above, the estimation error dynamics are

$$\dot{\tilde{\delta}} = -K_{sp}[(n - n_{prev})L_{mag} + L_{car} - \hat{\delta}]$$

The term $(n - n_{prev})L_{mag} + L_{car}$ is equal to δ to within a resolution of L_{mag} meters, and thus represents an independent measurement of the intervehicle distance. Since the error dynamics are a simple first order system, they can be made stable by simply choosing $K_{sp} > 0$.

The next two elements of the residual vector rely on the observer estimate and the magnetic marker count. The first element compares the estimated range to the radar measurement. The other residual compares the difference in the magnetic marker counts of the current and previous vehicles to the desired spacing which the automated vehicle is attempting to achieve. These elements of the residual vector can be written mathematically as

$$\begin{aligned} r_3 &= \delta - \hat{\delta}(\omega_w, v_{prev}, n, n_{prev}) \\ r_4 &= (n_{prev} - n)L_{mag} - L_{car} - \delta_{desired} \end{aligned}$$

4.2.3 Command Signal Residuals

The next three residuals compare the commanded throttle, brake pressure, and acceleration to the appropriate sensor measurements. These residuals are written as

$$\begin{aligned} r_5 &= a - u_{isl} \\ r_6 &= \alpha - \alpha_c \\ r_7 &= P_{wheel} - P_{mcc} \end{aligned}$$

4.2.4 Engine Dynamics Residuals

Two second order nonlinear observers are proposed to estimate both the engine speed and mass of air from engine speed measurements using the methodology developed above in Section 4.1 and the nonlinear vehicle model used in Section 3.1.1 for the longitudinal controller design. Both observers use the engine speed measurement for the correction term, while one observer uses the throttle and brake pressure sensors as inputs and the other uses the actuator commands. The first observer has the form

$$\begin{aligned}
\dot{\hat{\omega}}_e &= \frac{1}{J_e}(T_{net}(\hat{\omega}_e, \hat{m}_a) - c_x R^{*3} h^3 \hat{\omega_e^2} - R^* T_{rr} - R^* T_{br}(P_{wheel}) + K_{s1}(\omega_e - \hat{\omega}_e) \\
\dot{\hat{m}}_a &= MAX\,TC(\alpha)\,PRI(\hat{m}_a) - \dot{m}_{ao}(\hat{\omega}_e, \hat{m}_a) + K_{s2}(\omega_e - \hat{\omega}_e)
\end{aligned}$$

while the second observer can be written as

$$\begin{aligned}
\dot{\hat{\omega}}_e &= \frac{1}{J_e}(T_{net}(\hat{\omega}_e, \hat{m}_a) - c_x R^{*3} h^3 \hat{\omega_e^2} - R^* T_{rr} - R^* T_{br}(P_{mcc}) + K_{c1}(\omega_e - \hat{\omega}_e) \\
\dot{\hat{m}}_a &= MAX\,TC(\alpha_c)\,PRI(\hat{m}_a) - \dot{m}_{ao}(\hat{\omega}_e, \hat{m}_a) + K_{c2}(\omega_e - \hat{\omega}_e)
\end{aligned}$$

The residuals for these two observers form the next elements in the residual vector, specified as

$$\begin{aligned}
r_8 &= \frac{V_{man}}{R_{air} T_{man}} P_{man} - \hat{m}_a(\omega_e, P_{wheel}, \alpha) \\
r_9 &= \frac{V_{man}}{R_{air} T_{man}} P_{man} - \hat{m}_a(\omega_e, P_{mcc}, \alpha_c)
\end{aligned}$$

It is important to note that although these residuals will be nonlinearly related to the sensor measurements and actuator commands, the linear fault model given in Equation 4.1 is still applicable since the residuals can be shown to remain close to a linear system using the same argument as in (Garg and Hedrick 1995).

4.2.5 Torque Residuals

The last two residuals are again based on the nonlinear vehicle model, however they are the comparison of the torques acting on the engine. Using the engine speed differential equation, these residuals can be written as

$$\begin{aligned}
r_{10} &= J_e a + c_x R^{*3} h^3 \hat{\omega_e^2} + R^* T_{rr} + R^* T_{br}(P_{wheel}) - T_{net}(\omega_e, P_{man}) \\
r_{11} &= J_e a + c_x R^{*3} h^3 \hat{\omega_e^2} + R^* T_{rr} + R^* T_{br}(P_{mcc}) - T_{net}(\omega_e, P_{man})
\end{aligned}$$

4.3 Residual Processor

For the diagnostics of the physical layer longitudinal control system, a combination of weighted least squares estimation and thresholding is used to detect and identify faults. The first part of the residual processor provides a weighted linear least squares estimate of the fault mode vector. Next, each element of the estimate is compared to a threshold, and a fault is declared when one or more thresholds are crossed. Finally, classical logic is used to identify the faulty component based on the thresholds that are crossed. Each of these tasks will now be addressed in more detail.

4.3.1 Estimation of the Fault Mode Vector

The first task performed by the residual processor is to estimate the magnitude of the fault mode vector using the current value of the residual vector. This estimation of the fault mode is quite

useful for both fault diagnosis and fault management. In terms of fault diagnostics, the resulting estimate has a very intuitive relationship with the system dynamics and simplifies the choice of thresholds for fault detection. A fault management system could also potentially benefit from the estimate by choosing different methods of reconfiguration based on both the type of fault and it's magnitude.

Using the fault model described in Equation 4.1, the residual and fault mode vectors are related by the linear matrix equation

$$r(t) - r_{nom} = F\mu(t)$$

where r_{nom} is assumed to be constant with respect to time for simplicity. A weighted least squares solution for $\mu(t)$ can now be performed, where the residual vector is weighted by the matrix $W^{-\frac{1}{2}}$ to reduce scaling problems. The resulting estimate $\mu_{ls}(t)$ can be calculated by the following equation

$$\mu_{ls}(t) = F^{\dagger}(\mathbf{r}(t) - \mathbf{r}_{nom})$$

where $F^{\dagger} = (F^T W^{-1} F)^{-1} F^T W^{-1}$ is the weighted pseudo-inverse of F. Notice that $F^{\dagger}$ and $\mathbf{r}_{nom}$ can be determined apriori, so that only a vector addition and a matrix multiplication are required to calculate the estimate given the residual vector.

4.3.2 Thresholding and Decision Logic

The final task of the residual processor involves the choice of an appropriate threshold for each element of the fault mode vector, and the identification of the faulty component based on the thresholds exceeded. If the residual generator had structured residuals, then each fault would affect only one element of the fault mode estimate vector. The detection of a fault would then be a simple matter of choosing a threshold for each estimate element, and declaring a fault when one of the thresholds was exceeded. Identification would also be trivial, since the exceeded threshold would determine the component with the fault.

Unfortunately, the residual generator for the physical layer controller is only isolatable, which makes identification slightly more complicated. The isolability property only guarantees uniqueness of the fault signatures, however some signatures may be linear combinations of others. This is the case for both the throttle and brake actuator faults in the designed residual generator. The qualitative effects of each fault on the fault mode estimate have been summarized in Table 4.1, where H represents a "high" or increase in the estimate element and L represents a "low" or no increase in the particular estimate element. The table shows that although the actuator faults cause several elements to increase, they each have a unique effect on the fault mode estimate. Since only single faults are being considered, the actuator faults can be uniquely identified by the pattern of increased elements.

4.4 Simulation Results

The fault detection system designed in the previous sections was simulated in SHIFT to test its performance with the realistic vehicle model presented in Chapter 2. Further information about the simulation software is presented in Appendix A.

The simulations shown in this section consist of a platoon of three automated vehicles traveling on a straight road with a desired intervehicle spacing of 6 meters. The spacing of the magnetic

Table 4.1: Fault mode vector estimate μ_{ls} under component faults

Faulty Sensor / Actuator	μ_0	μ_1	μ_2	μ_3	μ_4	μ_5	μ_6	μ_7
wheel speed sensor	H	L	L	L	L	L	L	L
engine speed sensor	L	H	L	L	L	L	L	L
radar	L	L	H	L	L	L	L	L
accelerometer	L	L	L	H	L	L	L	L
magnetometer	L	L	L	L	H	L	L	L
throttle angle sensor	L	L	L	L	L	H	L	L
manifold pressure sensor	L	L	L	L	L	L	H	L
brake pressure sensor	L	L	L	L	L	L	L	H
throttle actuator	L	L	L	H	L	H	H	L
brake actuator	L	L	L	H	L	L	L	H

markers in the road was assumed to be 1 meter. In addition, sensor noise with a normal statistical distribution was included in the vehicle model for all of the simulations presented here. The statistical characteristics of the sensor noise is shown in Table 3.1. These characteristics are realistic estimates based on experimental measurements conducted using the Buick LeSabre experimental vehicles used at PATH.

This section will first present the simulation results for the performance of the intervehicle distance and nonlinear engine dynamics observers in the absence of faults, and then conclude with results for the diagnosis of each monitored fault.

4.4.1 Observer Performance

For the simulations of the observers, the desired behavior of the lead vehicle of the platoon was to track the given velocity profile shown in Figure 4.1. The two other automated vehicles in the platoon are in following mode, and will attempt to maintain the desired intervehicle spacing. Figure 4.2 shows the convergence of the inter-car spacing observer and its ability to track the actual radar measurement in the presence of noise. Figures 4.3 and 4.4 show the performance of the two engine dynamics observers designed in Section 4.2.4 in the absence of a fault. As all three figures show, the observers perform extremely well under constant and varying speed profiles.

4.4.2 Diagnosis of Faults

For the simulations in this section, the desired behavior of the lead vehicle of the platoon was to track constant velocity of 24 m/sec for simplicity. The two other automated vehicles in the platoon are in following mode, and will attempt to maintain the desired intervehicle spacing. After five seconds, a fault in one of the sensors or actuators occurs with a constant magnitude equal to the desired minimum detectable fault. The desired minimum detectable fault magnitudes for the physical layer control components were previously determined by Garg (Garg and Hedrick 1995), and their values are summarized in Table 4.2 along with the chosen thresholds.

Figures 4.5 through 4.14 show the fault mode vector estimates for faults in the wheel speed sensor, engine speed sensor, radar, accelerometer, magnetometer, manifold pressure sensor, throttle angle sensor, brake pressure sensor, and both actuators. The eight plots in each figure represent the

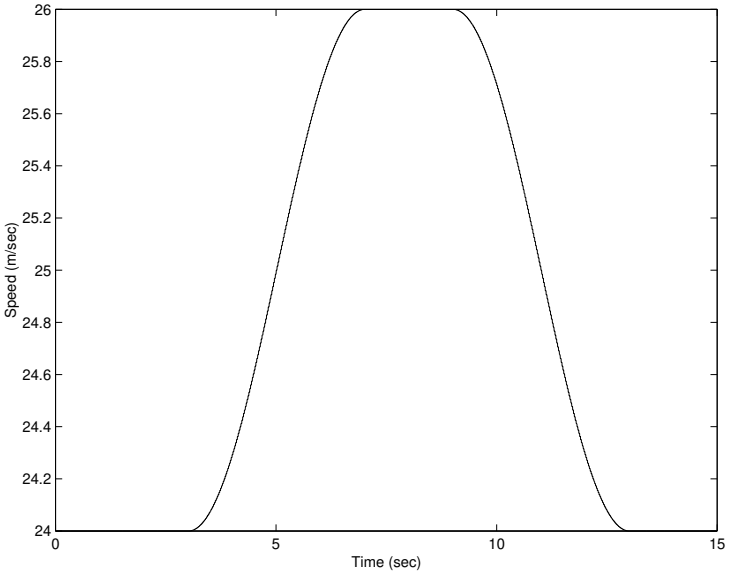

Figure 4.1: Desired velocity profile for observer simulations

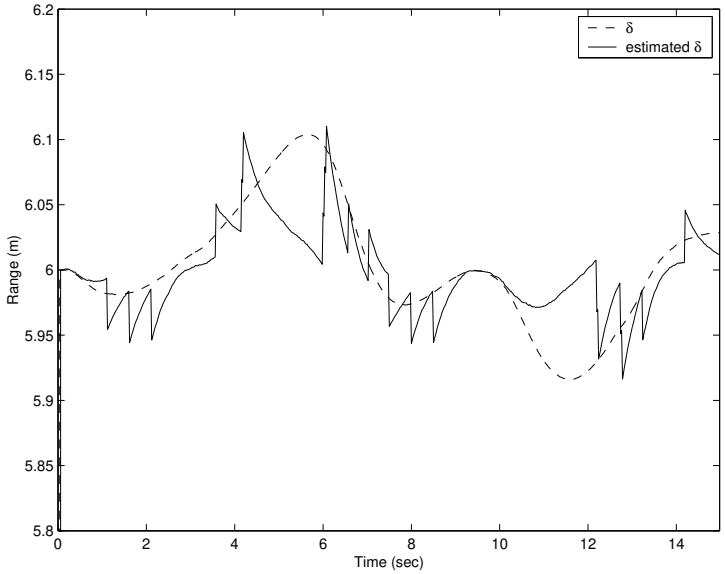

Figure 4.2: Inter-vehicle spacing observer in the absence of faults

estimate of the fault mode elements which represent each type of possible fault. The estimates are shown as solid lines, while the chosen thresholds are shown as dashed lines. Both are expressed in units which match those shown for the minimum detectable fault magnitudes in Table 4.2.

It is important to note that although the qualitative behaviors shown in Table 4.1 are idealistic, the simulation results basically agree with those shown in the table. However, three main discrepancies between the ideal and simulation results should be discussed. First, the estimates for several of the fault mode elements exceed their thresholds for approximately the first 1.25 seconds of the simulations. This is caused by the difference in initial conditions for the observer estimates and the vehicle model simulation, and any declaration of a fault during this time period would be disregarded.

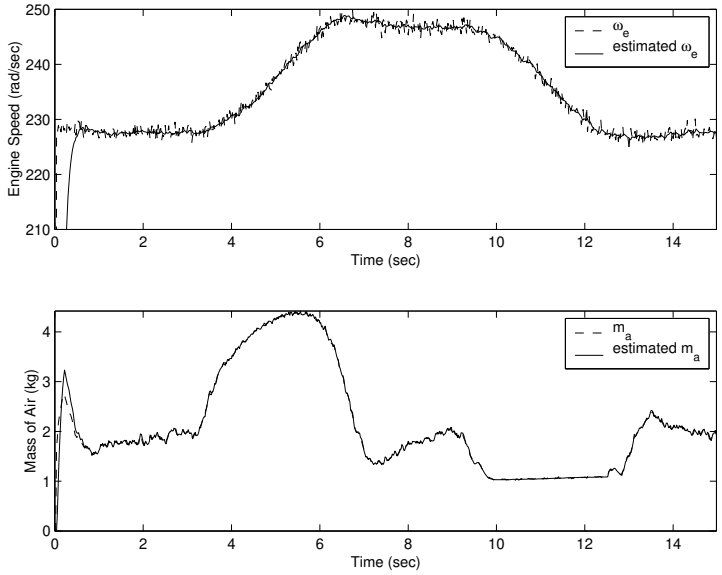

Figure 4.3: Engine speed and mass of air estimation in the absence of faults for the nonlinear observer using throttle angle and brake pressure measurements

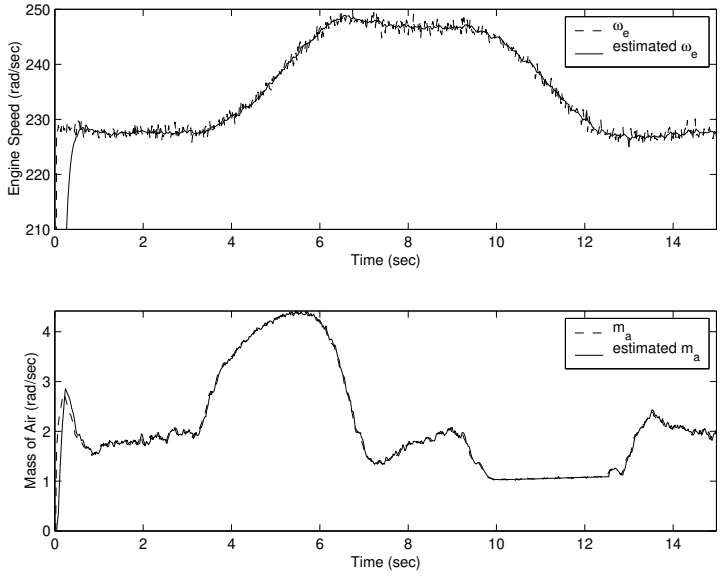

Figure 4.4: Engine speed and mass of air estimation in the absence of faults for the nonlinear observer using throttle and brake actuator commands

The second discrepancy is the transient increase in incorrect fault mode estimate elements at the onset of a fault. This effect is particularly noticeable in the wheel speed and magnetometer fault simulations in Figure 4.5 and Figure 4.9. These figures show that the radar mode estimate exceeds it's threshold even at the minimum detectable magnetometer fault, while the radar mode could exceed it's threshold at larger wheel fault magnitudes. This unwanted sensitivity could lead to incorrect identifications when magnetometer and wheel speed sensor faults occur. The cause of these transient effects is the strong similarity between some of the fault signatures. For example, the wheel speed and radar fault signatures are both cause marked changes in the residual element

Table 4.2: Minimum detectable fault magnitudes for each control component

Faulty Sensor / Actuator	Fault Magnitude	Threshold
wheel speed sensor	3 m/sec	1.5 m/sec
engine speed sensor	15 rad/sec	7.5 rad/sec
radar	0.8 m	0.6 m
accelerometer	0.3 m/sec^2	0.125 m/sec^2
magnetometer	2 marker counts	1.25 marker counts
manifold pressure sensor	5 KPa	3 KPa
throttle angle sensor & actuator	3 degrees	1.5 degrees
brake pressure sensor & actuator	250 KPa	125 KPa

r_3, so both fault mode estimates react to the wheel speed sensor fault. Once the effects of the fault on the system dynamics reaches steady state, the fault is correctly identified. However, the pattern of exceeded thresholds for these transient periods is also unique for the case of single faults and can therefore be considered as an additional fault signature. This property allows the faults with this transient behavior to be identified before the system dynamics reach steady state. Continuing with the wheel speed and radar example, the pattern of both the wheel speed and radar estimates exceeding their thresholds can be uniquely identified as the result of a wheel speed fault.

The last discrepancy can be seen in the steady state behavior of the fault mode estimates after a radar fault has occurred. At first glance, the behavior of the magnetometer and radar estimates appears to be similar to the transient effects just discussed. In this case however, the change in fault mode estimates is caused by the feedback control used in the regulation layer since there is no fault management conducted for these simulations. The radar fault is correctly detected and identified during the 5-6 second time period of the simulation, but the radar measurement is still being used by the follower law in the regulation layer. After 6 seconds of simulation, the feedback controller has increased the intervehicle spacing to attempt to match the correct desired spacing using the faulty measurement as feedback. This increase in spacing causes the residual element r_4 to correspondingly change to reflect the resulting difference between the desired spacing and the true spacing using the magnetometer counting scheme. Although this seems problematic, the radar fault would obviously be identified correctly within the first second after the faults onset, and before the controller uses the faulty measurements for very long.

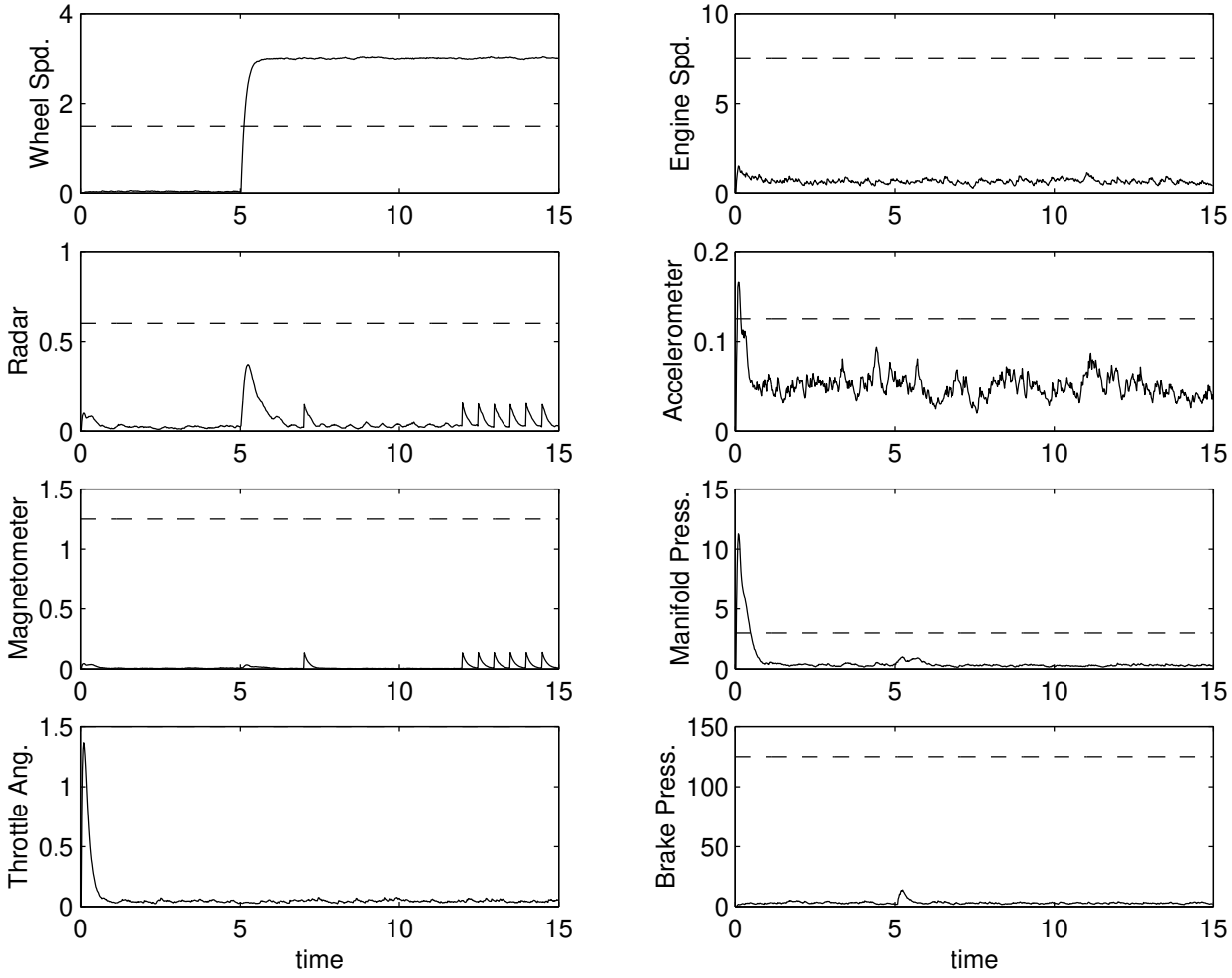

Figure 4.5: Fault mode estimate for a wheel speed sensor fault of 3 m/sec

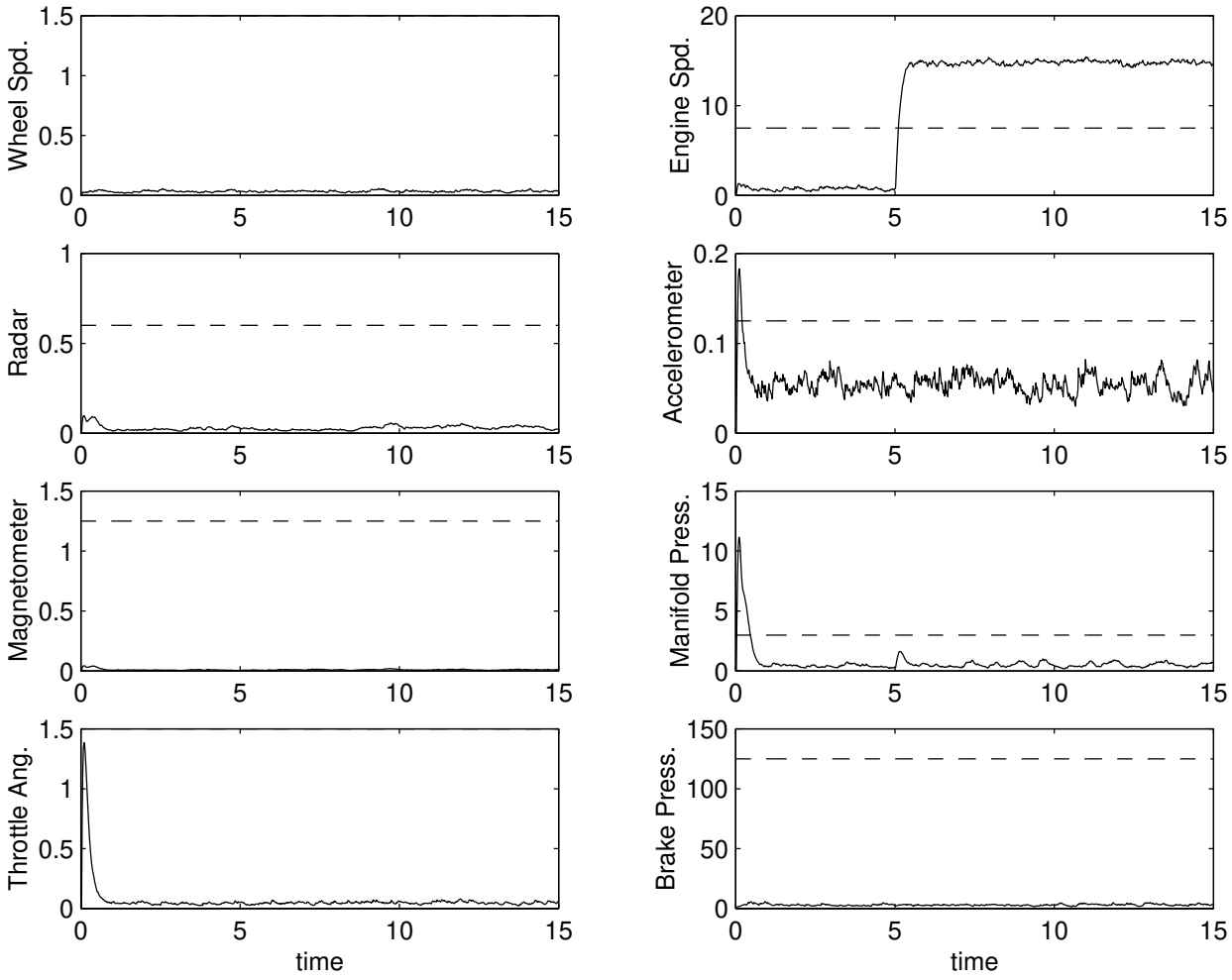

Figure 4.6: Fault mode estimate for a engine speed sensor fault of 15 rad/sec

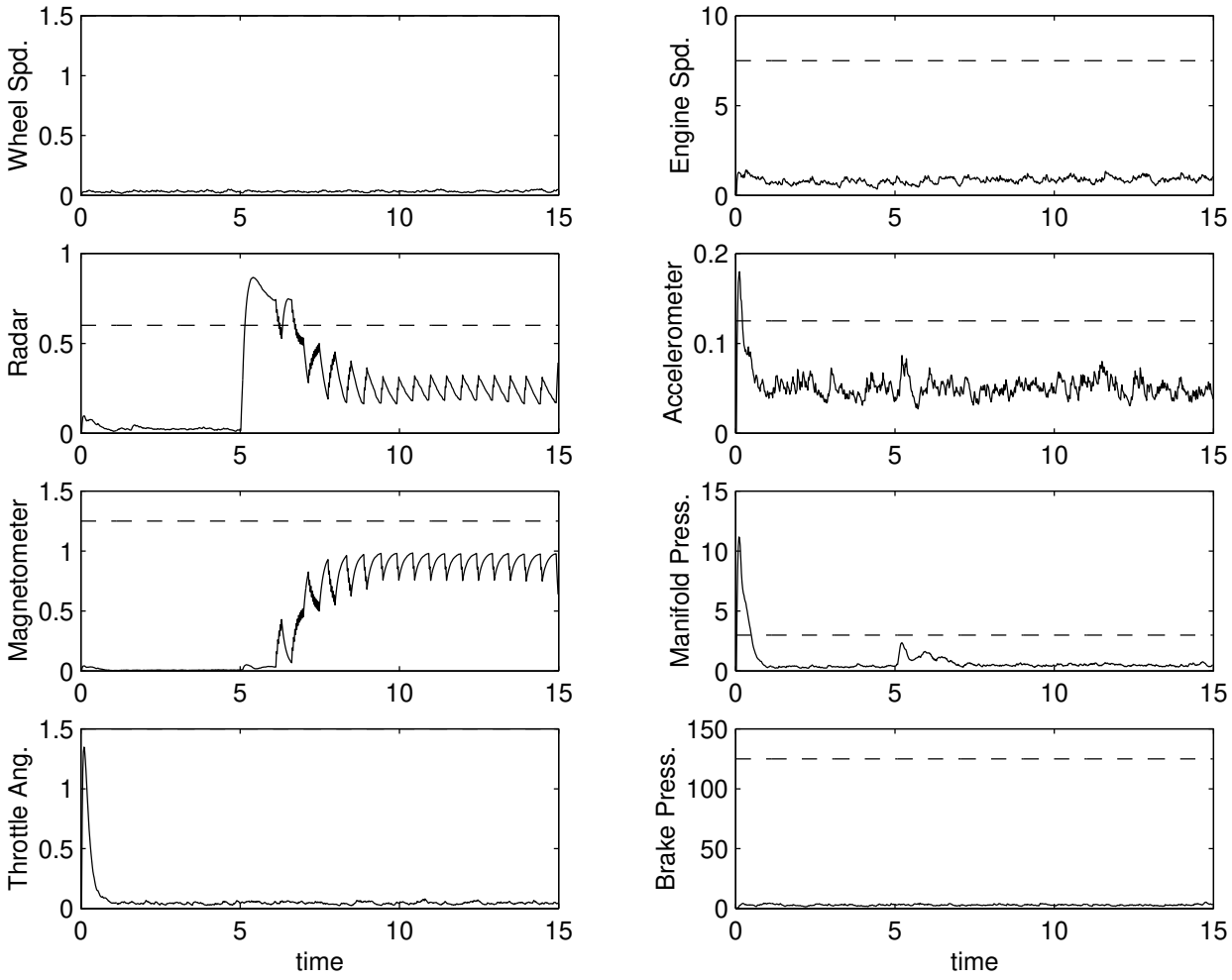

Figure 4.7: Fault mode estimate for a radar sensor fault of 0.8 m

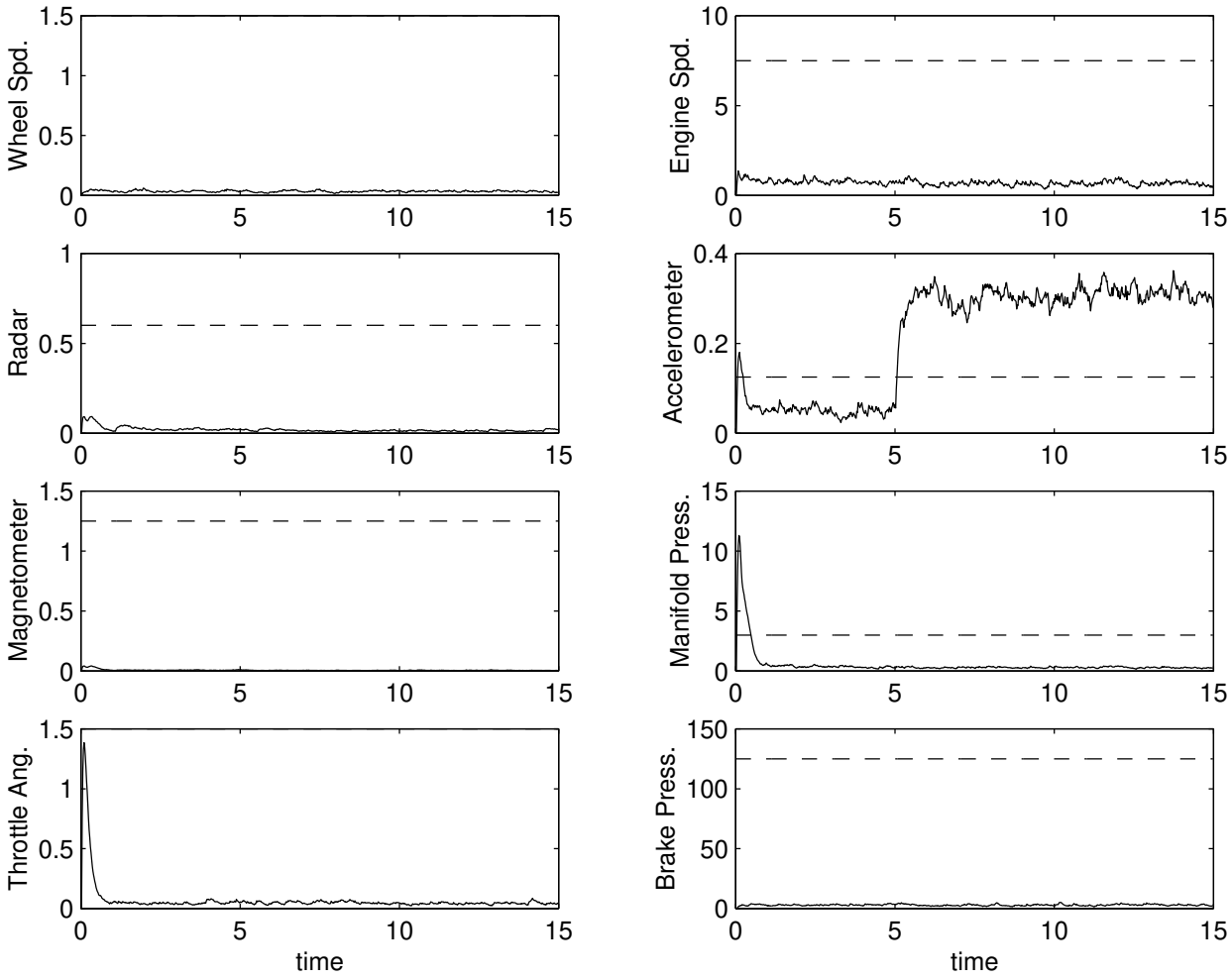

Figure 4.8: Fault mode estimate for a accelerometer fault of 0.3 m/sec^2

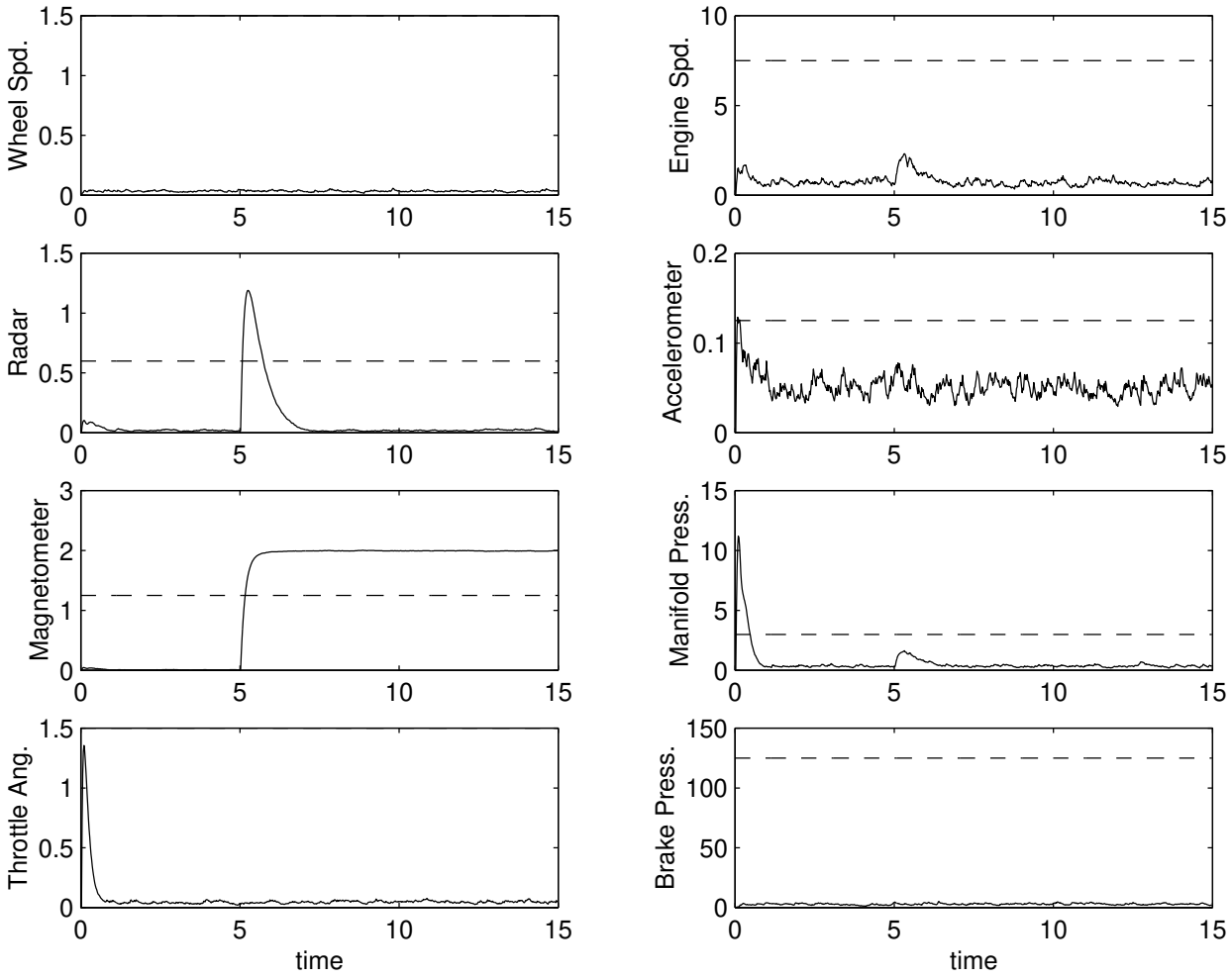

Figure 4.9: Fault mode estimate for a magnetometer fault of 2 counts

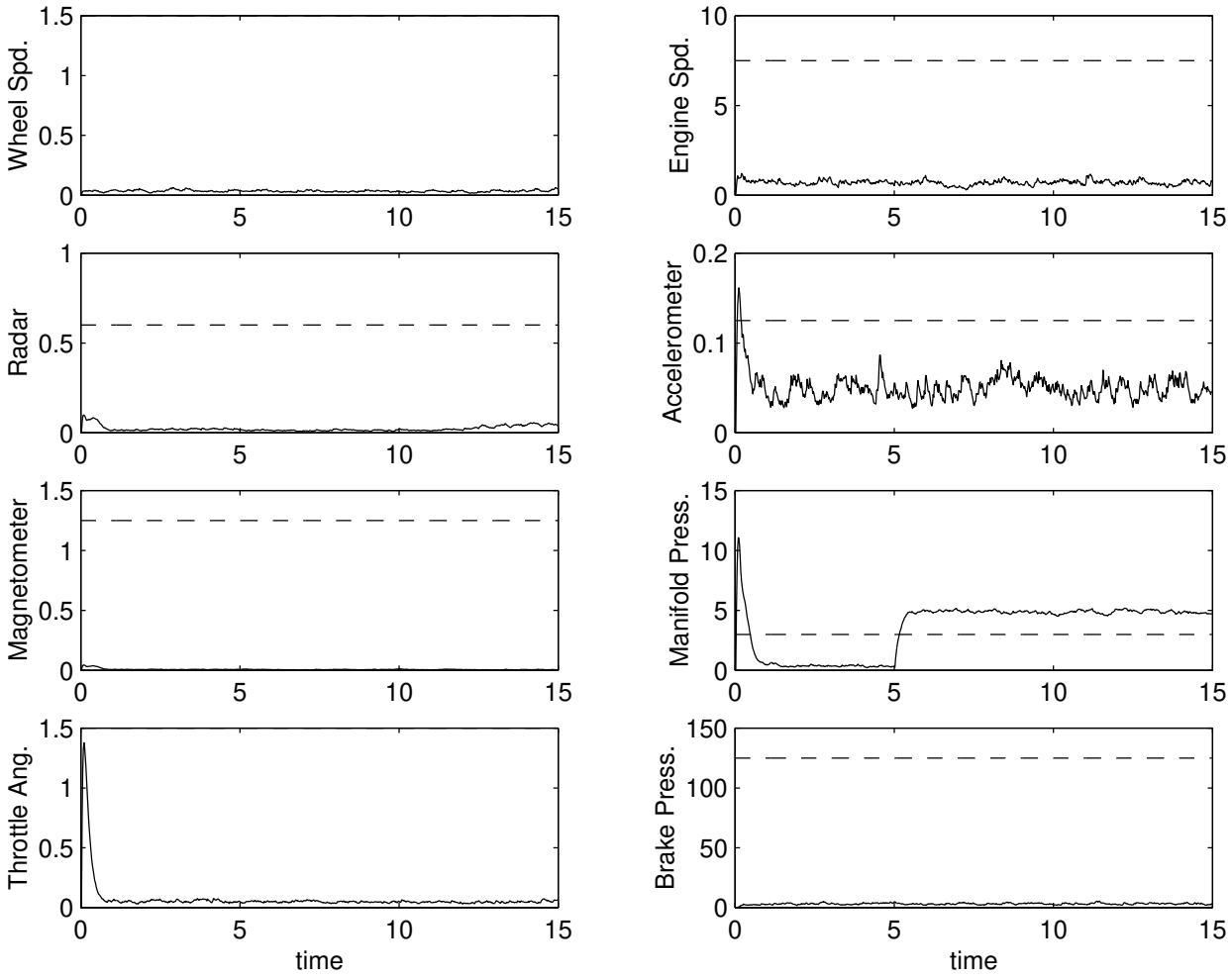

Figure 4.10: Fault mode estimate for a manifold pressure sensor fault of 5 KPa

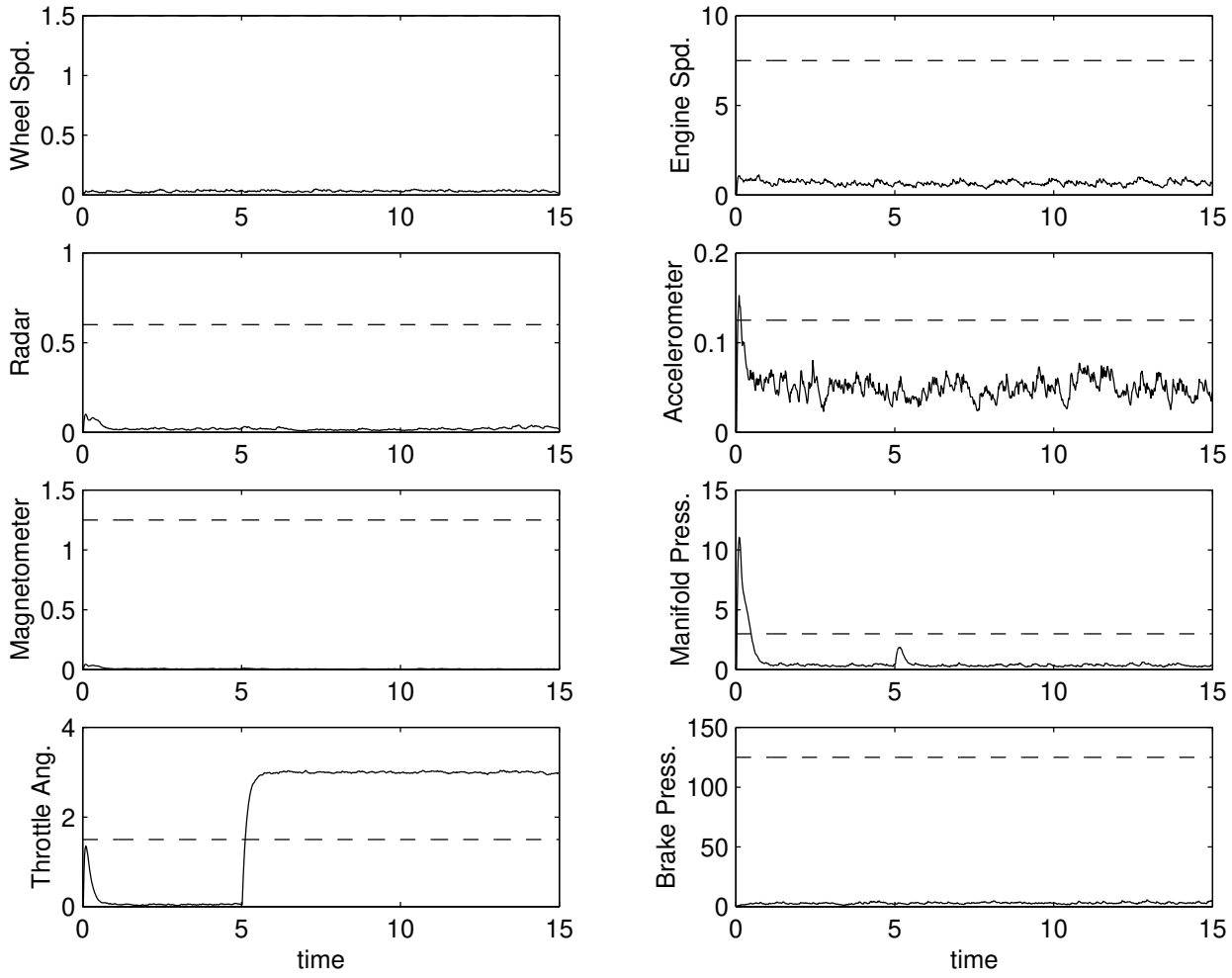

Figure 4.11: Fault mode estimate for a throttle angle sensor fault of 3 degrees

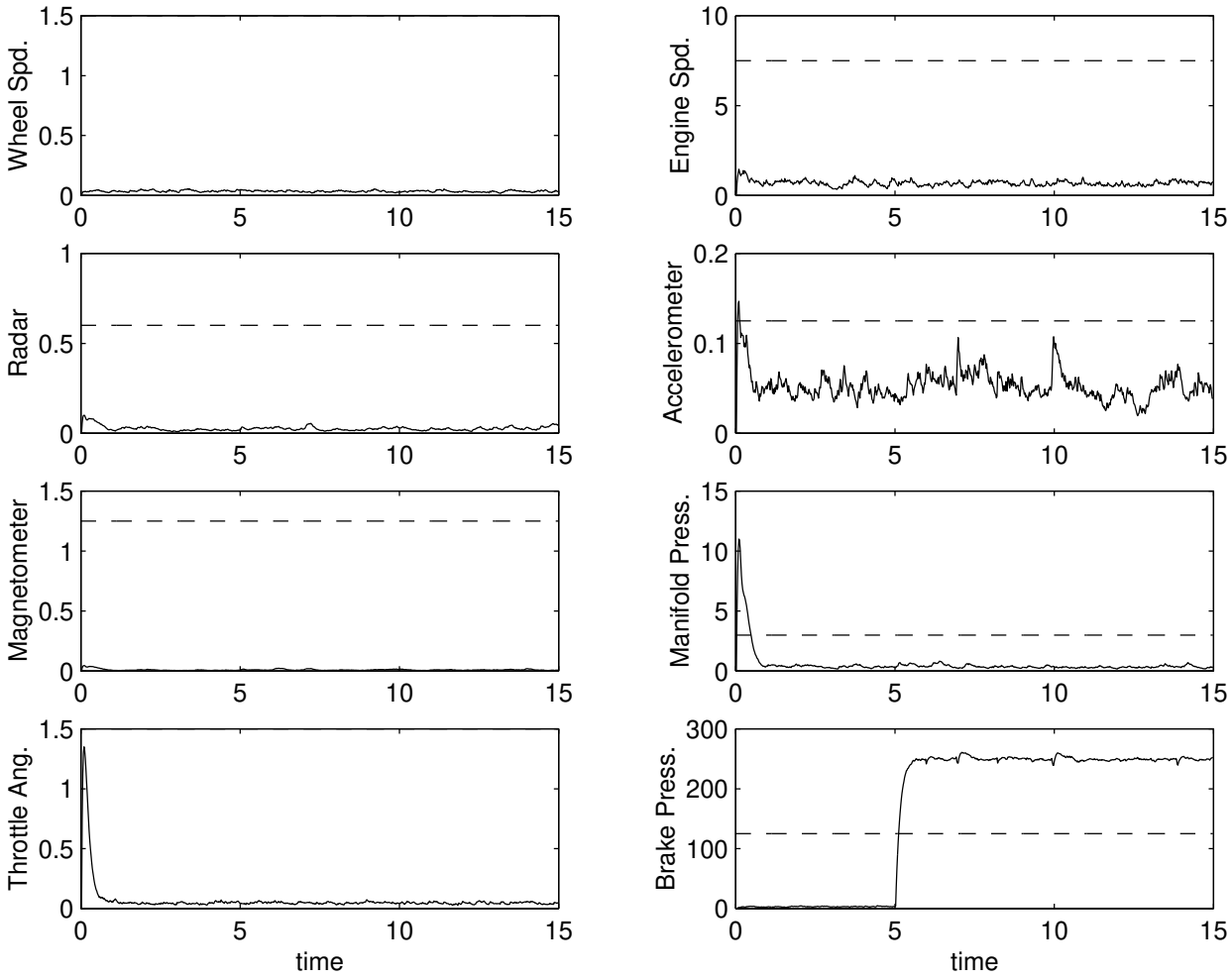

Figure 4.12: Fault mode estimate for a brake pressure sensor fault of 250 KPa

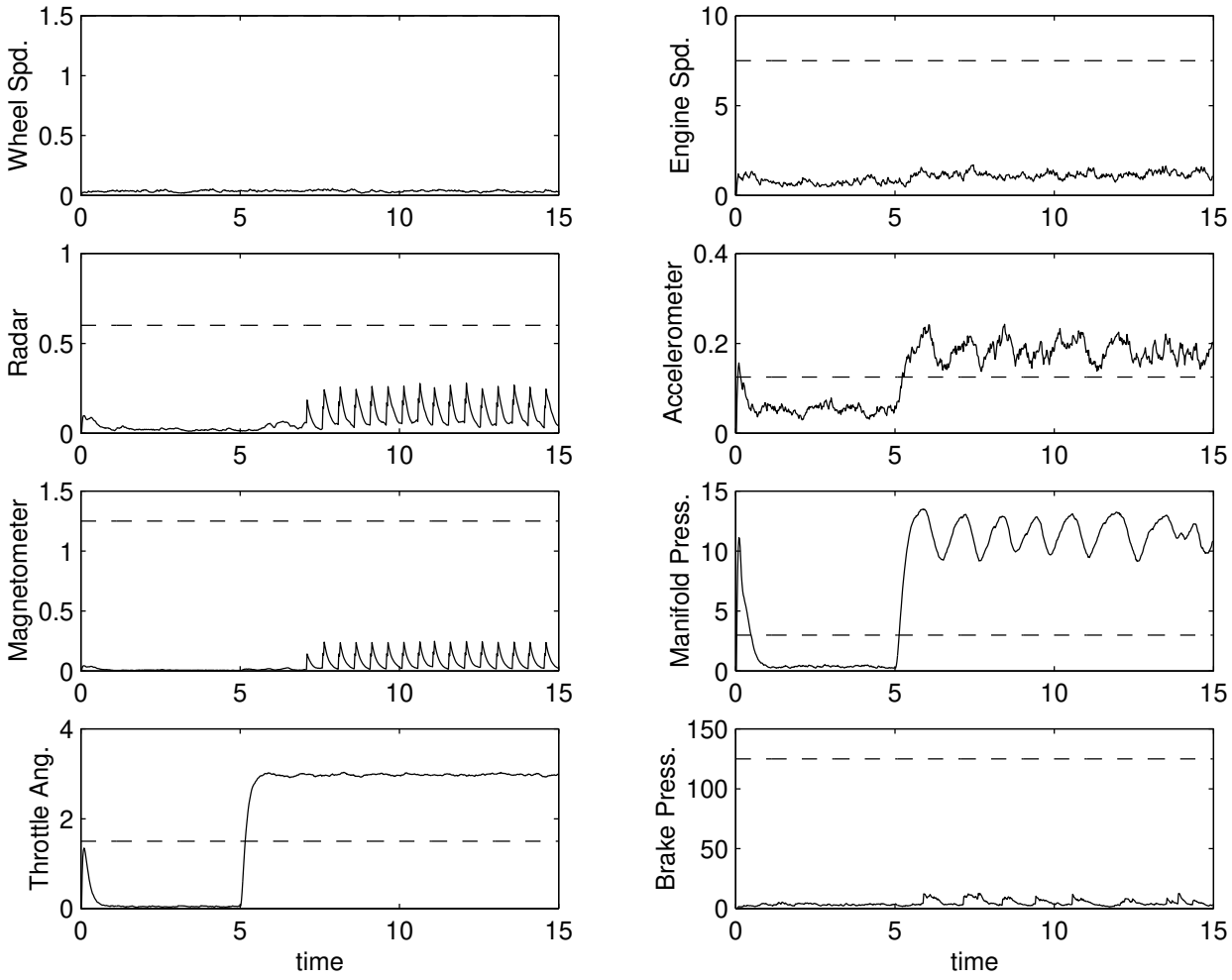

Figure 4.13: Fault mode estimate for a throttle actuator fault of 3 degrees

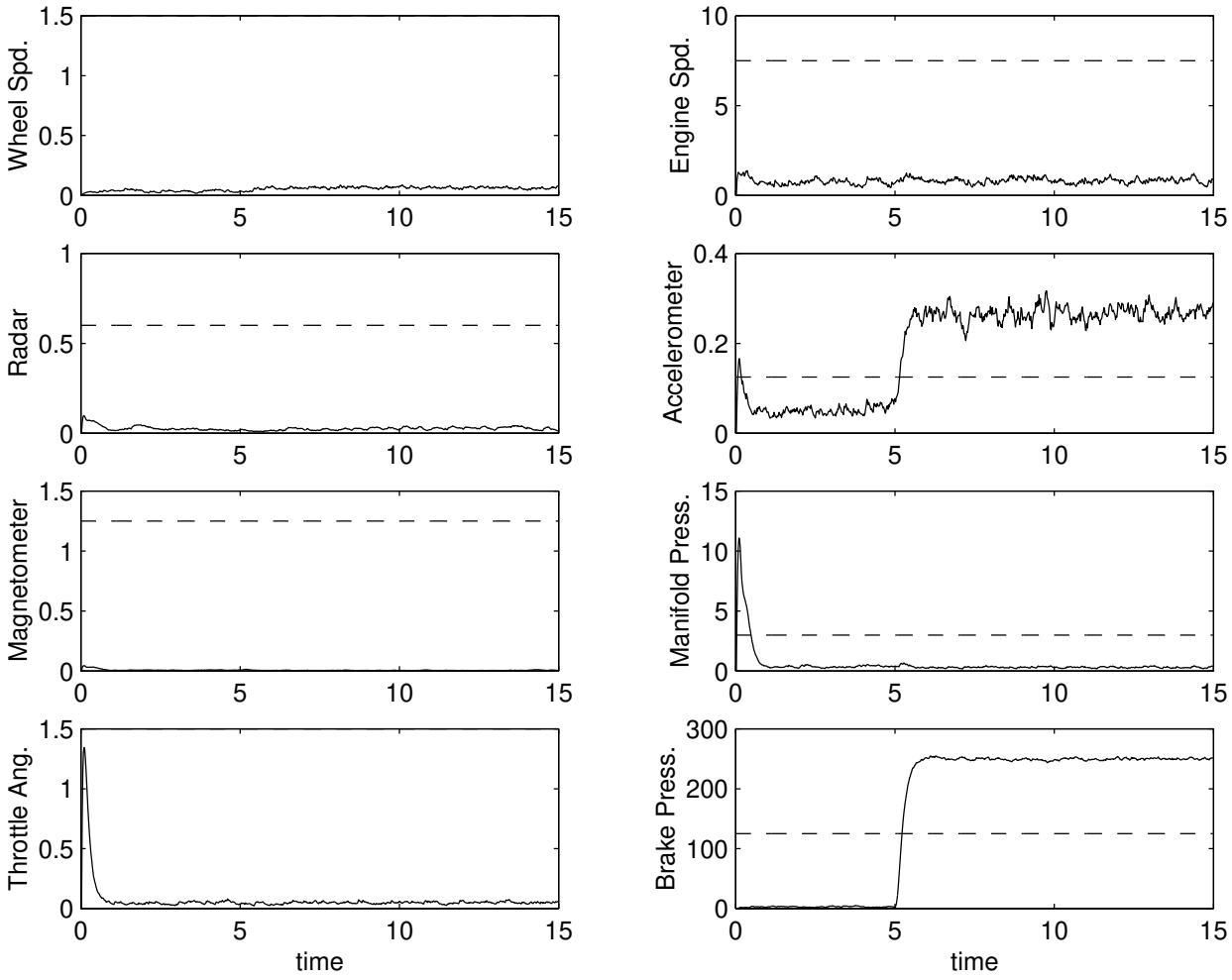

Figure 4.14: Fault mode estimate for a brake actuator fault of 250 KPa

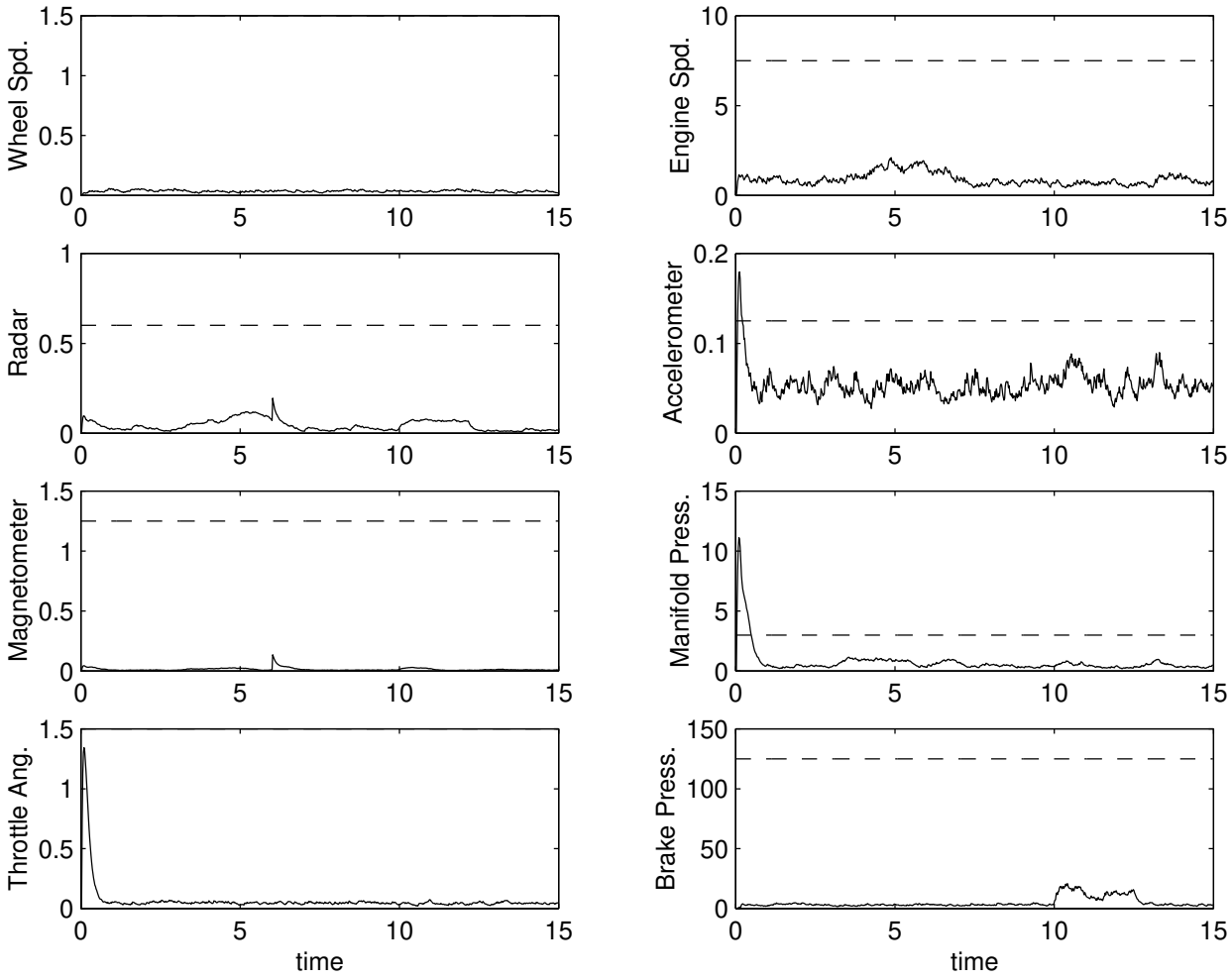

Figure 4.15: Fault mode estimate for a varying speed profile from Figure 4.1

4.5 Experimental Results

This section presents experimental results on the implementation and testing of the observers described in Section 4.2. The observers have been implemented on the Buick LeSabre experimental vehicles using the longitudinal control code developed for the 1997 NAHSC demonstration as a basis. Each observer was programmed as a separate C function which is called during the longitudinal control calculations. The remaining parts of this section will describe the tests and results for each of the observers.

4.5.1 Inter-vehicle Distance Observer

A simplified fault diagnostic and management system was implemented on the automated vehicles in preparation for the August 1997 NAHSC demonstration. This system was designed to diagnose and manage faults in the primary longitudinal control components consisting of the radar, throttle actuator, brake actuator, communications system and the CAN bus. The inter-vehicle distance observer was included in this system in order to detect faults in the radar range sensor and also to replace the radar range measurements in the regulation layer controller in the event of a radar fault. The inter-vehicle distance observer played a very important role in ensuring safe automated operation during the demonstration, since radar faults were detected and automatically replaced by the magnetic observer on several occasions during the automated platoon demonstrations.

Figure 4.16 illustrates the ability of the inter-vehicle distance observer to detect and correct for the radar faults. Each test vehicle in the platoon demonstration was designed with a rectangular opening in the front grill so that the radar would have a clear line of sight. The radar was then mounted behind this grill and below the hood of each car. In the test run shown in Figure 4.16, a misalignment of the grill mounting caused the radar to have an intermittent failure on the fifth car in the platoon. The readings of the radar jump from zero to the correct spacing value many times during the run. However, the fault detection system was triggered due to the 6 meter difference in the radar measurement and the inter-vehicle distance observer. In response to the detected radar fault, the spacing between fourth and fifth cars in the platoon was increased to 15 meters for the remainder of the run by the fault management system. In addition, the regulation layer controller used the inter-vehicle distance observer estimate to replace the radar range measurement in the calculations of the synthetic acceleration. The reconfigured controller was able to provide an excellent ride with a spacing variation of less than 1.3 meters. The maximum errors in spacing occurred in the presence of uphill and downhill grades.

4.5.2 Engine Dynamics Observer

The first step in the real-time performance testing of the fault diagnostic system designed in this project was the implementation of the engine dynamics observer. To verify the observers performance, the observer software was installed on a single automated vehicle and tested on the low speed track at the Richmond Field Station (RFS) facility. The goal of the automated vehicle was to follow the varying speed profile shown in Figure 4.17. An example of the typical results for the engine dynamics observer using the actuator commands is shown in Figures 4.18 and 4.19.

Although the observer performs fairly well, the estimation of the mass of air is definitely not accurate enough to detect faults in the manifold pressure sensor at the resolution used for the simulations in Section 4.4. A probable reason for the relatively large errors in the pressure

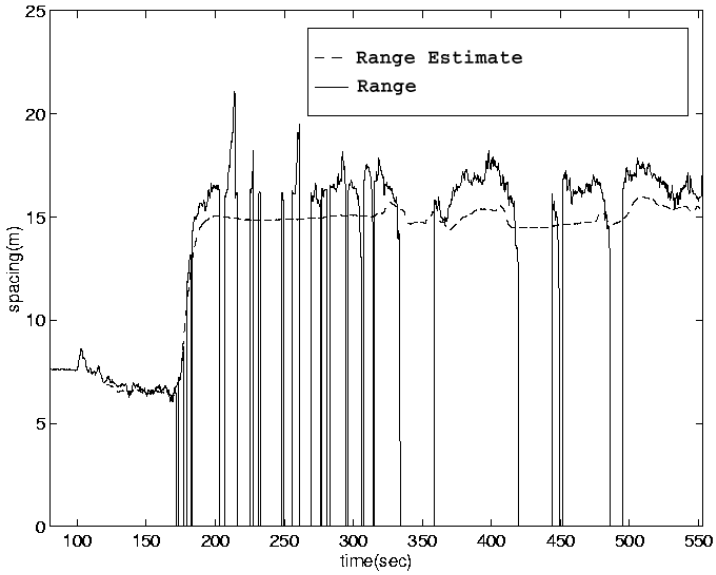

Figure 4.16: Experimental results for the inter-vehicle distance observer during an intermittent radar fault

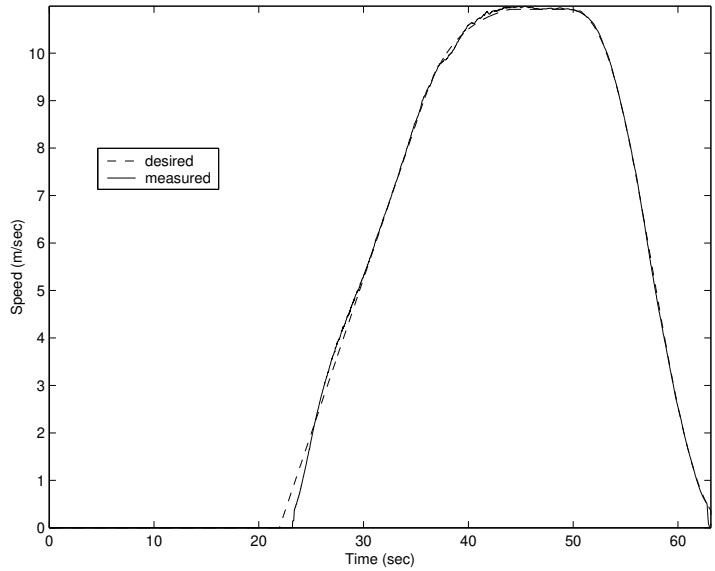

Figure 4.17: Desired velocity profile for experimental test run at RFS

estimation is the reduced accuracy of the static engine tables at lower engine speeds and manifold pressures. Although further research is required to improve the accuracy of the observer, it could still be used for fault diagnostics albeit with a larger minimum detectable fault magnitude. For example, the minimum detectable fault magnitude for a manifold pressure fault would need to be larger than 10.5 KPa for the results shown above in order to eliminate false alarms caused by estimation error.

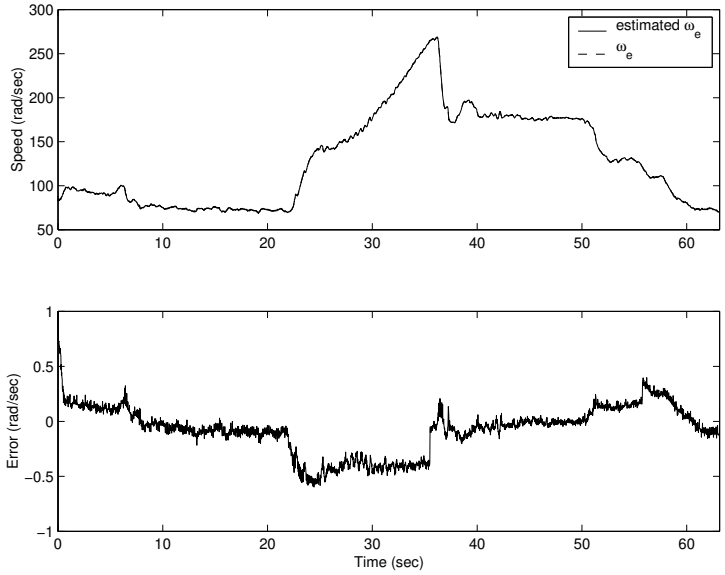

Figure 4.18: Estimation of engine speed during experimental test run at RFS

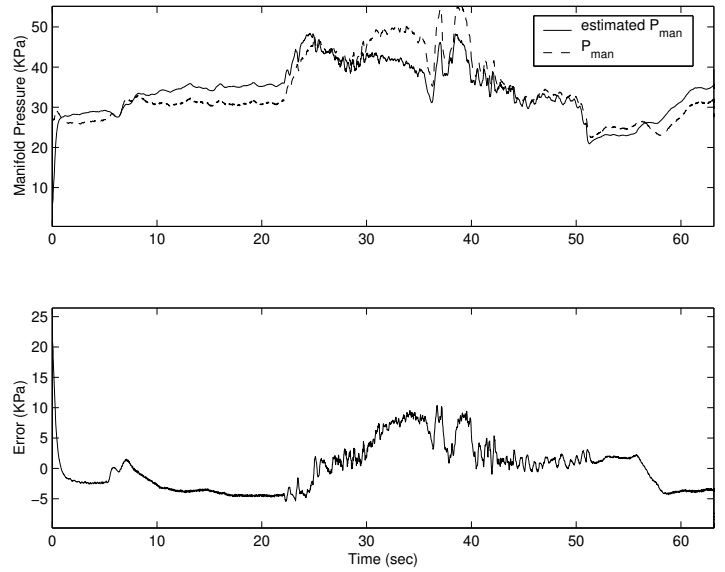

Figure 4.19: Estimation of manifold pressure during experimental test run at RFS

Chapter 5

Fault Management Systems for Longitudinal Controller

5.1 AHS Fault Tolerant Structure

In this chapter we follow the ideas presented in Lygeros *et al.* (2000) for the design of a hierarchical fault tolerant AHS. Lygeros *et al.* (2000) divide the problem of supervising the AHS operation into four major structures: sensor, capability, performance and control structures. The information flow between these structures is depicted in Figure 5.1. The sensor structure encodes all the information that is sensed at the individual vehicle level or at the roadside infrastructure level. The capability structure is designed to determine discrete changes in the system capability due to faults in the vehicle and roadside hardware. The objective of performance structure is to decide on any gradual degradation in system performance due to adverse environmental conditions and gradual wear of AHS components. The control structure, finally, decides on the control actions based on the information encoded by the three other structures. In this chapter we focus on the design of the capability and performance structures.

The fault management system works based on the AHS fault tolerant control structure scheme shown in Fig. 5.2.

Fig. 5.2 shows that the fault handling module receives information from the capability and performance structures. The design proposed in Lygeros *et al.* (2000) for the capability structure is in the form of a hierarchy of binary logic predicates, while the performance structure is realized through a set of maps from the causes of gradual performance degradation to the parameters that reflect the performance of the system. These maps can be realized on-line. Figure 5.3 shows more details about the capability structure and the performance structure suggested in Lygeros *et al.* (2000).

The capability structure in Figure 5.3 assumes the existence of a set of signals coming from a fault detection structure already in the appropriate format. The maps for the capability structure in Figure 5.3 are:

F_R - maps capabilities of the physical layer to the regulation layer.
F_I - maps capabilities of regulator to its supervisor.
F_C - maps capabilities of regulation layer, communication and neighboring vehicles to coordination layer supervisor.

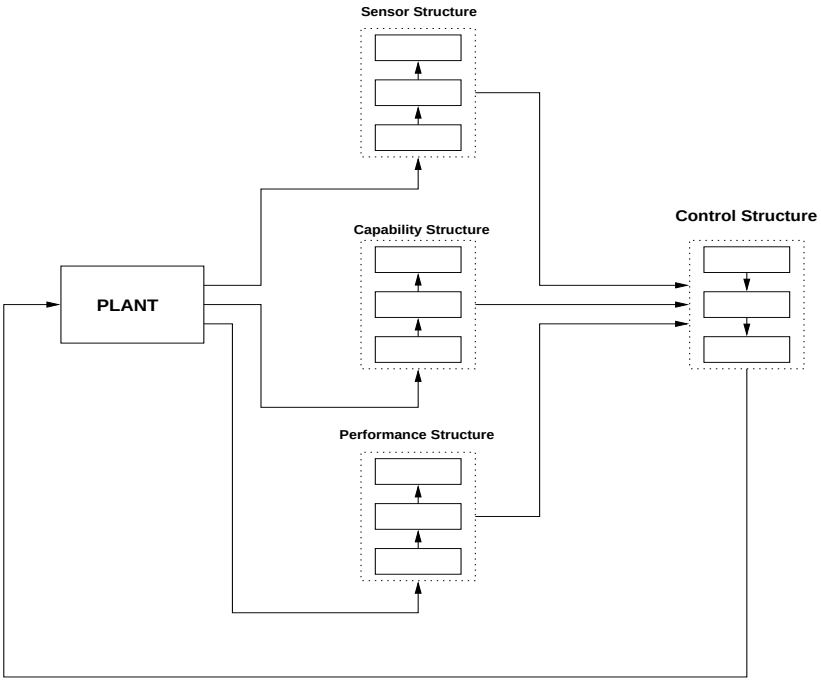

Figure 5.1: Overview of fault tolerant control structure

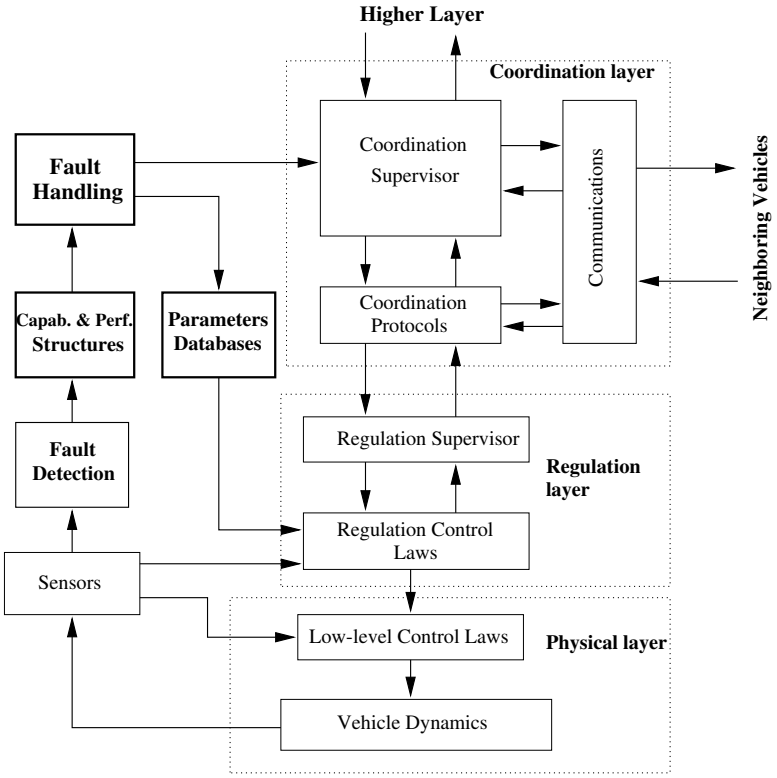

Figure 5.2: Extended hierarchical AHS fault tolerant control structure

The maps for the performance structure in Figure 5.3 are:

$$f: \quad \mathcal{C} \longrightarrow \mathcal{P}.$$

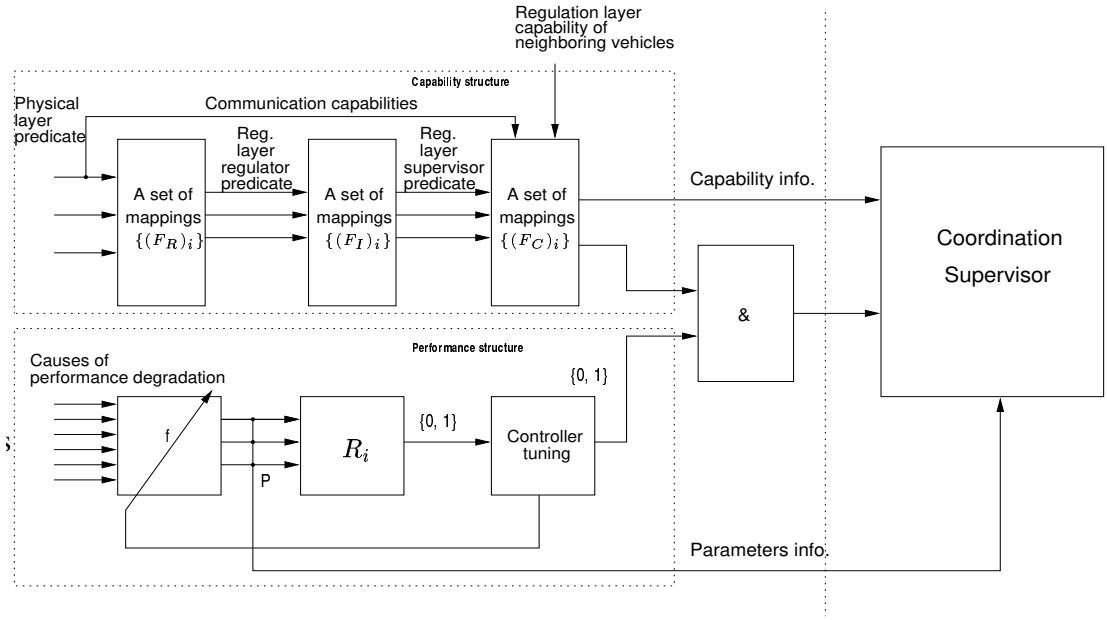

Figure 5.3: Capability and performance structure

$R_i : \ \mathcal{P} \longrightarrow \{0, 1\}; \qquad i = 1, \ldots, r.$
$\mathcal{C}$ – causes of degradation and performance parameters.
$\mathcal{P}$ – set of performance parameters
$\mathcal{P} = P_P \cup P_S \cup P_R \cup P_C \cup P_L \cup P_N.$

where the sub-indexes P, S, R, C, L and N stand for parameters related to the physical layer, sensor structure, regulation, link and network layers, respectively.

5.2 Capability Structure

5.2.1 Design of Capability Structure

The operation of the fault detection and identification (FDI) system can be divided into two primary tasks: the generation of signals sensitive to faults in the longitudinal control system components and their subsequent processing to detect the occurance a fault as well as the cause. The set of sensors and actuators which are assumed to be monitored in last chapter are shown in Table 5.1. In addition, the information about acceleration and velocity of the preceding vehicle and the lead vehicle in the platoon is obtained through the communication channels.

The creation of signals sensitive to control components, termed *residuals*, relies on redundancy in the information known about the vehicle. This redundancy can be achieved through multiple sensors at the cost of additional hardware and physical complexity of the system. However, model based fault diagnostic techniques overcome these additional costs by taking advantage of the mathematical relationships between the physical components to provide the necessary redundancy. The FDI system described in sections 4.1, 4.2 and 4.3 gives more details about construction of observers, residual generation and processings. Briefly, the observers proposed are as follows:

Table 5.1: Components monitored by the FDI system

Sensors	Actuators
Radar, manifold pressure sensor, engine speed sensor, accelerometer throttle angle sensor, wheel speed sensor, brake pressure sensor, magnetometer	*Brake actuator, throttle actuator*

- **Relative position observer**
  The relative position between two vehicles is estimated using the first order linear observer:

$$\dot{\hat{\delta}} = v - v_{prev} + k_s \left[(n - n_{prev})L - \hat{\delta} \right] \tag{5.1}$$

  where $\hat{\delta}$ is the inter-vehicle distance estimate, $v - v_{prev}$ is the velocity difference between the current and previous vehicle, L is the magnetic marker spacing, and $n - n_{prev}$ is the difference in the number of markers passed by the two vehicles.

- **Engine speed and manifold flow rate observer** A nonlinear detection filter based on the methodology presented in Garg and Hedrick (1995) allows estimation of the manifold pressure and engine speed using the following second order observer:

$$\begin{cases} \dot{\hat{\omega}}_e = & \frac{T_{net}(\hat{\omega}_e, \hat{m}_a) - c_a R^3 h^3 \hat{\omega}_e^2 - R(hF_f + K_b P_{mcc})}{J_e} + \\ & l_1(\omega_e - \hat{\omega}_e) + l_2(m_a - \hat{m}_a) \\ \dot{\hat{m}}_a = & MAX \cdot TC(\alpha) \cdot PRI(\hat{m}_a) - \\ & \dot{m}_{ao}(\hat{\omega}_e, \hat{m}_a) + l_3(\omega_e - \hat{\omega}_e) + l_4(m_a - \hat{m}_a) \end{cases} \tag{5.2}$$

  where ω_e and $\hat{\omega}_e$ are the measured and estimated engine speeds, m_a and $\hat{m}_a$ are the measured and estimated mass of air in the intake manifold, $T_{net}(\hat{\omega}_e, \hat{m}_a)$ is the net engine torque, $TC(\alpha)$ is the nonlinear throttle characteristic function of throttle angle α, $PRI(\hat{m}_a)$ is the pressure ratio influence function of the throttle body, and $\dot{m}_{ao}(\hat{\omega}_e, \hat{m}_a)$ is the mass flow rate of air out of the intake manifold. Finally, MAX, c_a, R, h, J_e are constant vehicle parameters, while l_1, l_2, l_3 and l_4 are the chosen observer gains.

- **Vehicle speed observer**
  By using accelerometer and magnetometer measurements, a and Δn respectively, the vehicle's absolute velocity can be estimated by the following first order observer:

$$\dot{\hat{v}} = a + k_v(\frac{\Delta n L}{T} - \hat{v}) \tag{5.3}$$

  where Δn is the number of magnets passed in time T and L is the magnet spacing.

The capability structure is implemented by a set of finite state machines whose function can be viewed as transformations that map the set of binary numbers produced by the FDI system into another set of binary numbers. This new set indicates the availability of each regulation layer control law and coordination layer maneuver, according to the pattern of faults that is presented

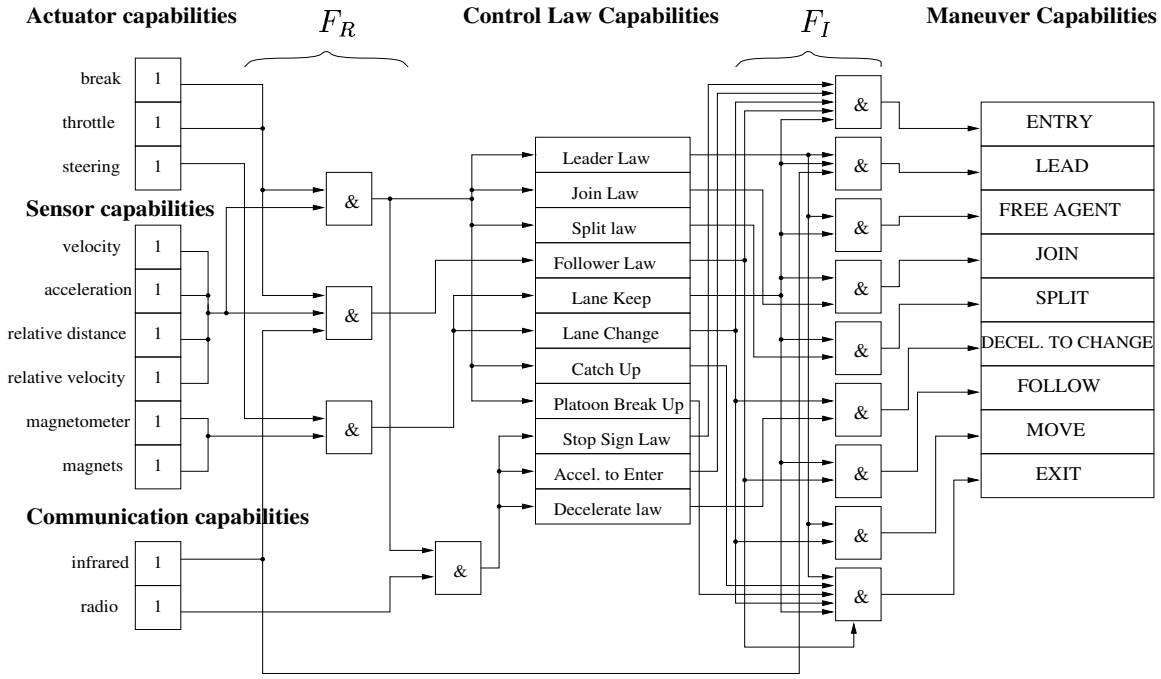

Figure 5.4: Logic structure of fault handling for normal mode AHS

by the FDI system (see Eskafi (1996), for example, for more details about the regulation and coordination layers).

We present a very simple example, taken from Lygeros *et al.* (2000), to illustrate the capability structure under the normal mode of operation. One approach to implement this capability structure example in SHIFT is discussed.

The control scheme for normal operating conditions relies on a number of resources: sensors, actuators and communication devices [1], both on vehicles and on the roadside. From an input-output point of view, the goal of the capability structure is to take information from this resources and to determine the influence of failures in any of these resources on the ability of a vehicle to perform a given maneuver. To achieve this goal Lygeros *et al.* (2000) proposed a design based on a hierarchy of logical binary predicates. In Figure 5.4, each predicate will monitor a single functional capability and will return a "1" (True) if the system possesses a correct capability or a "0" (False) otherwise[2]. The values returned by the predicates higher in the hierarchy depend, naturally, on the values of predicates at lower levels of the hierarchy. The example in Figure 5.4 illustrates the hierarchical binary logic process. The maps F_R and F_I can be denoted as:

$$F_R : \ \{0,\ 1\}^{n_{act}+n_{sen}+n_{comm}} \longrightarrow \{0,\ 1\}^{n_{long}+n_{lat}}$$
$$F_I : \ \{0,\ 1\}^{n_{long}+n_{lat}} \longrightarrow \{0,\ 1\}^{n_{man}}$$

where n_{act}, n_{sen} and n_{comm} indicate the number of actuators, sensors and communication channels,

[1] Even though in the fault diagnostic system given in Chapter 4, we have not considered the communication device faults, we assume that these communication faults can be detected in the fault management scheme design, see Sengupta (1999) and Simsek *et al.* (1999) for details in communication fault diagnostics.

[2] For this reason the logical predicates are processed by AND operators

respectively. n_{long} and n_{lat} the number of longitudinal and lateral control laws in the regulation layer, respectively. Finally, n_{man} denotes the number of maneuvers in the coordination layer.

Fig 5.5 shows the generic finite state machines that compose the hybrid system implementation of the capability structure.

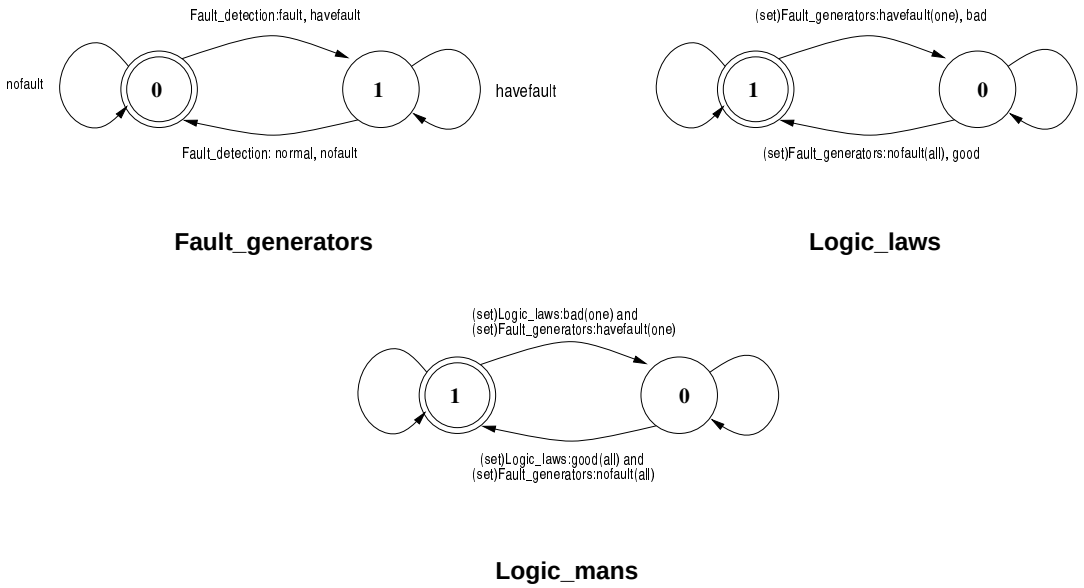

Figure 5.5: Capability structure finite state machines

Fault information, together with the capability information, is sent to the fault handling module which is located next to the coordination layer. Depending on the kind of fault and its severity, the fault handling module classifies the faults and initiates an alternative control strategy or degraded maneuver to overcome it. In some cases, the redundancy features normally available in FDI are exploited. For example, the output of the linear and nonlinear observers is used as an alternative information source for the measurements that are no longer available when a fault in a sensor occurs. In other cases, some degraded maneuvers must be executed to let the faulty vehicle exit the highway or stop on the highway for emergency vehicles.

The faults among sensor, actuator and communication devices are classified into two classes. The first one corresponds to faults which can be handled by using the information provided by the observers in the control algorithms and adjusting the controller parameters. For these faults, the operation mode is still normal. The second class includes the faults which require degraded mode maneuvers. The faults in the first class are less severe than those in the second one. A description of the handling procedures followed by the FMS is provided below.

Faults that are handled in normal mode

Radar range and range rate sensor faults

Radar measurements, range and range rate are used in all longitudinal maneuver control laws. Therefore a radar fault affects all of them. When the radar range rate sensor is at fault, it is possible to use the vehicle velocity and the LAN communication to estimate the relative velocity to the vehicle ahead. For the range measurement, the range observer in Eq. (5.1) is employed to estimate the relative distance between two vehicles.

Manifold pressure sensor fault
The manifold pressure sensor is used to calculate the manifold flow rate according to the ideal gas law. When the engine manifold pressure sensor is diagnosed with a fault, the manifold flow rate observer in Eq. (5.2) is used. This allows to use this flow rate to derive an estimate of the manifold pressure, $\hat{P}_m$, according to

$$\hat{P}_m V = \hat{m}_a R_g T_m \tag{5.4}$$

where R_g is a thermal coefficient, T_m is the manifold temperature, and V is the volume of the manifold.

Engine speed sensor fault
When the engine speed sensor has been detected to be faulty, it is possible to use the wheel speed sensor measurement as a signal to estimate the engine speed under the assumption that the torque converter is locked, i.e.

$$\hat{\omega}_e = \omega_w / h \tag{5.5}$$

where h is the driven-train ratio including the torque converter, transmission and the differential gears.

Wheel speed sensor fault
If a wheel speed sensor is faulty, the vehicle speed can be estimated from a combination of the radar range rate measurements and the LAN communication information that provides the preceding car velocity [3]. Alternatively, it is possible to estimate the wheel speed using the engine speed sensor measurements by assuming that the torque converter is locked.

Accelerometer fault
If an accelerometer fault has been detected there are two situations. In the first one, the vehicle is a follower. In this case there is no direct effect on the follower control law given in (Swaroop 1994); however, the incorrect acceleration information is communicated to the next follower vehicle. To compensate for this fault, the desired or "synthetic" acceleration is communicated instead of the actual measured acceleration.

If the faulty vehicle is the leader of the platoon, the feedback safety control laws in (Li *et al.* 1997) require vehicle acceleration information. In this case, velocity information is used to produce a numerical estimate of the acceleration.

Magnetometer fault
When the magnetometer fails, the vehicle is still able to perform the basic longitudinal control laws[4]. However, a flag is set to warn the system of the existence of a single fault.

Throttle angle sensor fault
The throttle angle measurement is not directly used by the regulation layer control laws. However a fault in this sensor most likely will induce a throttle actuator fault.

[3]When wheel speed (ω_w) is used to estimate the vehicle absolute velocity (v), it is assumed that there is no slip between the tires and the road surface, and the linear relationship $v = R\omega_w$ is used.

[4]Notice however that a magnetometer fault inhibits all lateral control and therefore has a great impact on vehicle's ability to remain in the AHS

Brake pressure sensor fault
A brake pressure sensor fault does not directly affect the regulation layer controller, however it can have a direct effect on the brake actuator and can induce faulty operation in it.

Since the accuracy of the estimates used whenever there is a fault in this first group is assumed to be smaller than the accuracy of the sensor provided measurement, in all cases, with the exception of the last three faults, the intra- and/or inter-platoon space are increased to L_{1f} and/or L_{2f}, respectively [5].

Faults that are handled in degraded mode

LAN Communication fault
When the LAN communication channel in a vehicle has a fault, this vehicle can not form part of a platoon since its fault will compromise the string stability (Swaroop 1994)[6]. Coordination layer maneuvers are executed to isolate the vehicle as a free agent as soon as possible. If the faulty vehicle is a platoon leader, it commands the second vehicle in the platoon to initiate a split maneuver. If the faulty vehicle is a follower, two split maneuvers are executed; the first one splits the faulty vehicle from the other vehicles ahead and the second split separates it from the vehicles behind. In both cases, the faulty vehicle becomes a free agent and exits the highway.

WAN Communication fault
If a fault in WAN communication has been declared, the faulty vehicle cannot coordinate with any other vehicle for maneuvering. At this point the vehicle is commanded to stop in the highway[7].

Brake actuator fault
When a fault has been detected in the brake actuator, no normal mode maneuver can be safely executed. The faulty vehicle needs assistance from other vehicles in the highway to stop. A front-dock (Lindsey 1997) maneuver must be initiated for the faulty vehicle through WAN communication. With this maneuver the previous platoon helps the faulty vehicle stop on the highway.

Throttle sensor/actuator fault
The throttle actuator fault is detected and identified using the engine speed and manifold observers in Eqs. (5.2)-(5.5).

When a throttle actuator fault has been detected, the faulty vehicle must be isolated from other vehicles and then forced to exit or to stop in the highway. If the faulty vehicle is a leader, its follower vehicles are commanded to split from the faulty leader using communication. If the faulty vehicle is a follower, two split maneuvers are performed such that the faulty vehicle becomes a free agent. In either case, the inter-platoon space is increased to L_{2f} and, after the splits are finished, the faulty vehicle will attempt to exit the highway. If the severity of the throttle actuator fault does not allow this, the vehicle is stopped in the highway.

[5]The increased distances, L_{1f} and L_{2f}, are calculated based on observer accuracy and safety distance under the worst cases for the leader and followers of a platoon. In the NAHSC '97 Demonstration $L_{1f} = 2L_1$ and $L_{2f} = 2L_2$, respectively, where L_1 and L_2 are the intra- and inter-platoon distance. In AHS design, $L_1 = 1 - 2m$ and $L_2 = 30 - 60m$.

[6]Strictly speaking if the vehicle is still able to receive information it can be the last follower of a platoon, although this is not the approach taken in this section to handle the LAN communication fault.

[7]Ideally, there should be some redundancy in the WAN communication devices considering the big impact of this kind of fault in the AHS throughput. However in this section this redundancy is not considered.

5.2.2 Simulation Results

The simulation results in this section show how the designed fault management system can safely handle the class of faults presented in this section for the longitudinal maneuver control in AHS. In the simulations, the platoon consists of three automated vehicles on a two lane highway as illustrated in Fig. 5.6, produced by the simulation animation. The same velocity profile for the platoon leader as that given in section 4.4 is used.

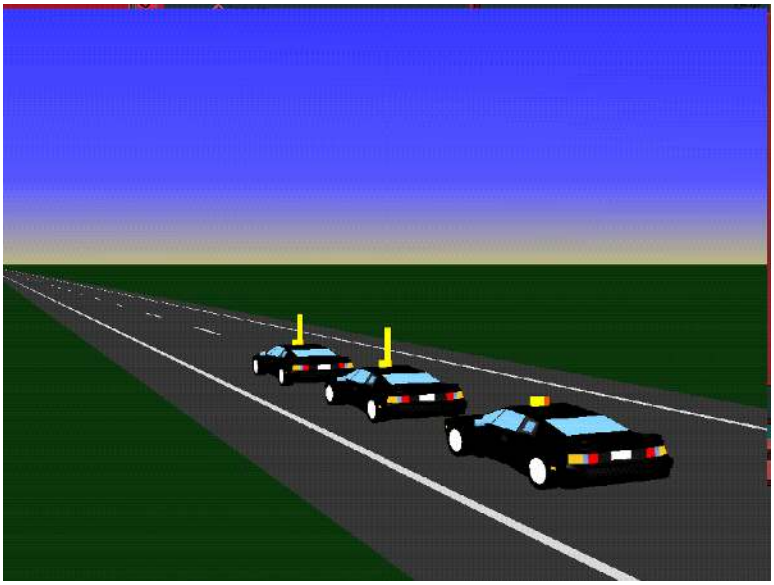

Figure 5.6: Simulation scenario for fault management system

A fault in the radar of the second vehicle is simulated in the results shown in Fig. 5.7. The fault is induced at $t = 4sec$ while the third vehicle is involved in a split maneuver. The simulation results show that the fault management system is still able to sustain a safe normal mode of operation. The third vehicle finishes the split maneuver and then it is commanded to perform a join. The maneuvering of the third vehicle is not affected even though there is a radar fault because the FMS decides to use the magnetometer observer information to replace the range measurement from the radar. The intra-platoon space has been increased from $2\ m$ to $4\ m$. The plots in Fig. 5.7 show: a) the relative distances among the three vehicles, b) the relative velocities, c) the absolute velocities and (d) the accelerations.

Fig. 5.8 shows another simulation result. The second vehicle in the platoon has a throttle actuator fault at $t = 4sec$. The fault management system commands two split maneuvers. First the leader of the platoon splits with respect to the second and third vehicles and then the third vehicle splits from the second vehicle. After the two split maneuvers, the faulty vehicle has been isolated and will stop or exit the highway. The plots in Fig. 5.8 are ordered similarly to Fig. 5.7.

5.3 Performance Structure

Safe feedback based longitudinal maneuvers for AHS and their associated control laws have been derived in Alvarez and Horowitz (1999) and Li *et al.* (1997). These maneuvers are proven to be safe (i.e. vehicle collisions never occur) under the assumption that an upper bound on the maximum

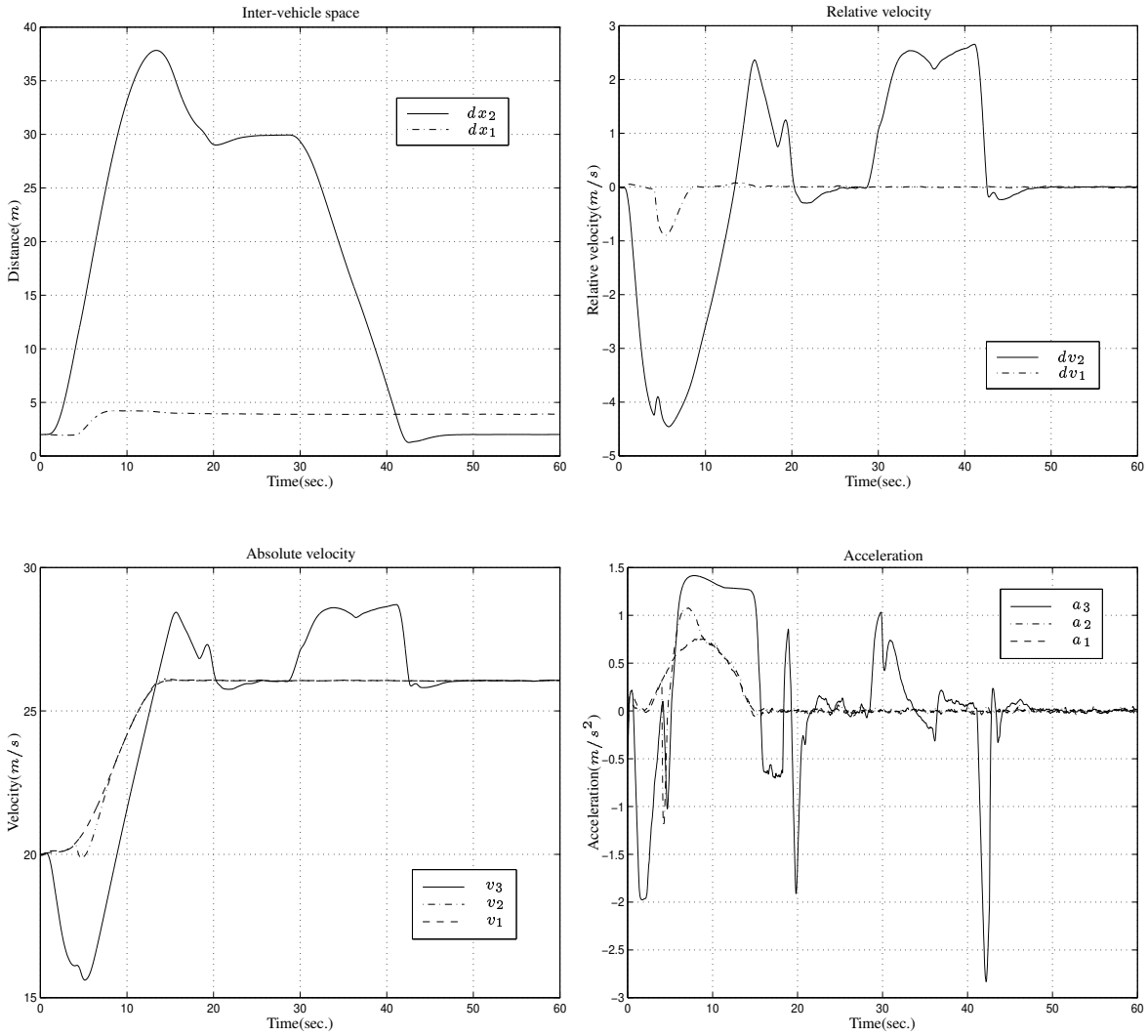

Figure 5.7: The control strategy when the second car has radar sensor fault at $t = 4sec$

deceleration a_{min} of all vehicles is known[8]. This safety critical maximum deceleration is closely related to the performance of vehicles during the emergency braking maneuvers that may be needed for fault handling purposes (Lygeros *et al.* 2000). The braking capacity of vehicles changes with adverse environmental conditions, gradual wear of components and highway topology, etc. There are two main factors that influence this braking capacity: tire/road friction and available braking torque. These factors have complex behavior and the associated variables are difficult to measure.

In order to maintain AHS safety it is imperative that the braking capabilities of all vehicles in the system be conservatively estimated at all times. On the other hand, to increase highway throughput it is also necessary that a_{min} be estimated as closely as possible to its actual value.

In this section a scheme for estimating the tire-road friction coefficient of a vehicle is presented which is guaranteed to underestimate its true value at all times, but converges to the true value under persistence of excitation conditions. A scheme for estimating an overall brake system gain is also

[8]In addition, the maneuvers are shown to be optimal in the sense that they are completed in minimum time, while satisfying comfort and safety constraints.

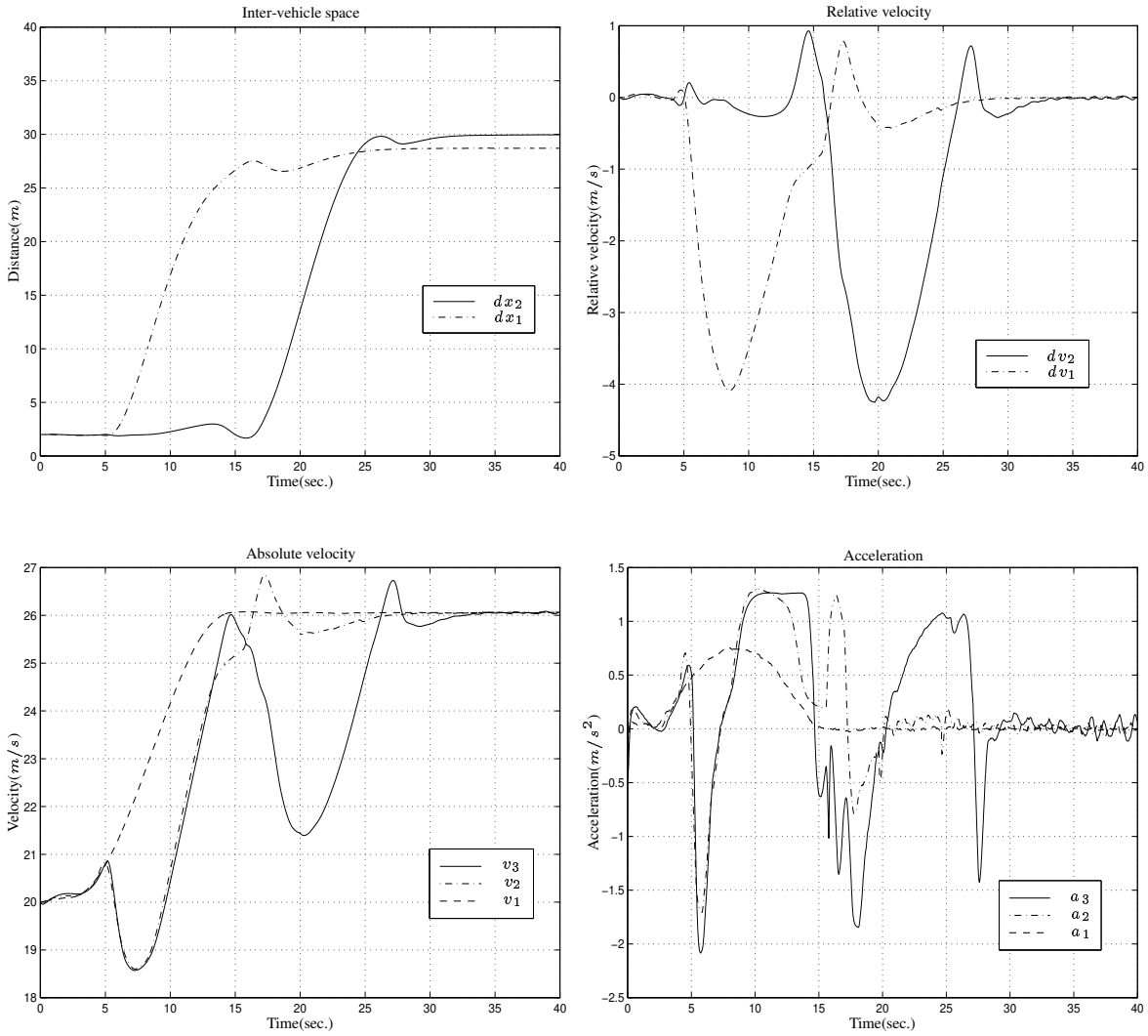

Figure 5.8: The control strategy when the second car has throttle actuator fault at $t = 4sec$

introduced. Based on these two estimation schemes an emergency braking controller is designed.

It is important to remark that the knowledge of the tire/road friction characteristic allows vehicles not only to adjust their spacing for safety, they can also broadcast this information to the road-side infrastructure controller, which in turn can modify overall traffic conditions if necessary.

This section is divided in six subsections. Section 5.3.1 develops a dynamic model of vehicles. In section 5.3.2, the estimation procedure for the tire/road friction is introduced. Section 5.3.3 describes the design of a stabilizing controller for emergency braking while section 5.3.4 describes the necessary conditions for friction underestimation. Simulation work is illustrated in section 5.3.5.

5.3.1 Vehicle Modeling

To describe the vehicle longitudinal dynamics, a quarter vehicle model is used. The intention of the model is dual: to develop dynamic expressions to be used later on for control purposes and to

derive the coefficient of tire/road friction as a function of the vehicle dynamics. The longitudinal motion of the vehicle can be expressed by

$$m\dot{v} = 4F_x - F_{ax}\,, \tag{5.6}$$

where v is the longitudinal speed of the vehicle, m is its mass, F_x is the force at the tire and F_{ax} is the aerodynamic drag force. It is assumed that forces at the tires are evenly distributed. The rotational dynamics at the wheel is described by

$$I\dot{\omega} = \tau_d - \tau_b - F_x R\,, \tag{5.7}$$

where ω is the angular velocity, I the wheel inertia, τ_d the driving torque, τ_b the braking torque and R the effective rolling radius. Eqs. (5.6) and (5.7) assume that the longitudinal velocity v and the wheel angular velocity ω are related through the relative velocity, s, defined as

$$s = v - R\omega\ . \tag{5.8}$$

During braking, relative velocity s and slip λ are related by $\lambda = s/v$. The drag force and tire force are modeled by

$$F_{ax} = C_{ax}v^2\,; \quad F_x = -\mu F_N = -\mu\frac{mg}{4}\ , \tag{5.9}$$

with C_{ax} a properly chosen constant, μ the tire/road friction and $F_N = mg/4$ the normal load in each tire.

Substituting Eqs. (5.9) into Eqs. (5.6) and (5.7) and using the time derivative of Eq. (5.8) yields

$$\dot{v} = -c\,\mu - d\,v^2\,, \tag{5.10}$$

$$\dot{s} = -(a+c)\,\mu - b - dv^2 + e\,K_b P_b\,, \tag{5.11}$$

with $a = R^2 mg/4I$, $b = R\tau_d/I$, $c = g$, $d = C_{ax}/m$ and $e = R/I$. As suggested in Gerdes and Hedrick (1995), the braking torque is approximated by $\tau_b = K_b P_b$, where K_b is an overall brakes system gain and P_b the master cylinder pressure. During braking, $\tau_d = 0$ is considered. The velocity v and relative velocity s are assumed to be uniformly continuous functions.

5.3.2 Tire/road Friction Characteristics

Literature for tire/road friction estimation is abundant. We revise some of the relevant work for the purposes of this section. Bakker *et al.* (1987a) and Burckhardt (1993) describe two analytical models for tire/road behavior that are intensively used by researchers in the field. In these two models the coefficient of friction, μ, is mainly determined based on the wheel slip λ and some other parameters like speed and normal load. Fig. 5.9 presents two curves, obtained from Harned *et al.* (1969), that represent typical μ versus λ behavior.

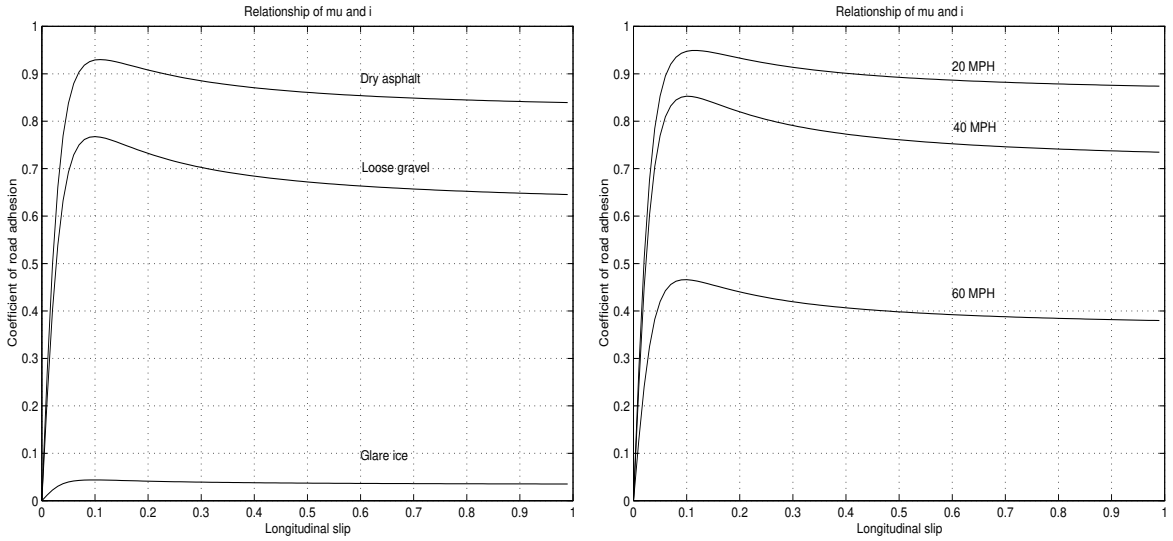

(a) Different road surface conditions

(b) Different vehicle velocities

Figure 5.9: Variations between coefficient of road adhesion μ and longitudinal slip λ

The expression given by Bakker *et al.* (1987a), also known as "magic formula" is derived heuristically from experimental data to produce a good fit. It provides the tire/road coefficient of friction μ as a function of the slip λ. The expression in Burckhardt (1993) is derived with a similar methodology. The final map expresses μ as a function of λ, the vehicle velocity, v, and the normal load on the tire, F_N.

Kiencke (1993) presents a procedure for real-time estimation of μ. A simplification to the analytical model by Burckhardt (1993) is introduced in such a way that the relation between μ and λ is linear in the parameters. Kiencke (1993) uses a two stage identification algorithm. In the first stage, the value of μ is estimated. This estimate of μ is used in the second stage to obtain the parameters for the simplified μ versus λ curve.

The paper by Gustafsson (1997) derives an scheme to identify different classes of roads. The hypothesis in Gustafsson (1997) is that by combining the slip and the initial slope of the μ versus λ curve it is possible to distinguish between different road surfaces. The author tests for asphalt, wet asphalt, snow and ice and identifies the actual value of the slope with a Kalman filter and a least squares algorithm.

Ray (1997) estimates μ based on a different approach. Instead of using the slip information to derive a characteristic curve, Ray (1997) estimates the forces on the tires with an extended Kalman filter. Using a tire model introduced by Szostak *et al.* (1988), that expresses the tire forces as a function of μ, the author tries this model for different values of μ. A Bayesian approach is used to determine the value of μ that is most likely to produce the forces estimated with the extended Kalman filter.

The work in Kiencke (1993), Gustafsson (1997) and Ray (1997) does not consider any velocity dependence in the derivation of μ, as suggested by Burckhardt (1993) and Harned *et al.* (1969). An attempt to consider the velocity dependence for ABS control is presented in Liu and Sun (1995). The authors assume the tire/road characteristics to be known. Due to the limitations in the available data, the authors are not able to compare their algorithm with other methods.

There are other works related to the on-line identification of the tire/road friction, as for example Lee and Tomizuka (1995) and Yi and Jeong (1998). However, in these papers only the instantaneous coefficient of friction is identified.

All the research above is based on the pseudo-static models for the road/tire friction. Recently, a LuGre dynamic model for friction was introduced in Canudas de Wit *et al.* (1995). This model is applied to road/tire friction in Canudas de Wit and Tsiotras (1999) and Canudas de Wit and Horowitz (1999), where lumped and distributed parameter models derived from a LuGre friction model are presented. It is shown that with this model it is possible to reproduce the shape of the pseudo-static magic formula. There are however some issues regarding the calibration of these models that still need further investigation. This section is only concerned with pseudo-static friction models as the ones in Bakker *et al.* (1987a) and Burckhardt (1993), as the experimental data available for simulation purposes was derived with the pseudo-static approach.

For emergency braking, braking forces are large and therefore high values of slip are expected[9]. If the time and distance for braking are to be minimized, emergency braking maneuvers should attempt to sustain maximum friction during all the maneuver. For this reason it is very important to make an priori estimation of the point of maximum friction based on the information available from the instantaneous coefficient of friction, as this maximum friction point will be used as a target slip point by the emergency braking controller. The strategy in this section is to use different points of the instantaneous coefficient of friction to identify the shape of the curve that describes the behavior of the coefficient of friction. Once this curve is identified, it is possible to deduct a proper value for the maximum coefficient of friction.

The model proposed in (Burckhardt 1993) is

$$\mu = \left(C_1(1 - e^{-C_2\lambda}) - C_3\lambda\right) e^{-C_4 v}\,, \tag{5.12}$$

where $C_1, \cdots, C_4$ are constants and the normal load at the tire is kept constant. In this project this model is approximated by

$$\mu = p_1 e^{-p_2\lambda} \lambda^{(p_3\lambda + p_4)} e^{-p_5 v}\,, \tag{5.13}$$

where p_1, p_2, p_3, p_4 and p_5 are parameters to be determined. As shown in section 5.3.5, Eq. (5.13) accurately approximates the behavior of Eq. (5.12), particularly in the region $\lambda \in [0, \lambda_m]$, where λ_m is the point where the maximum coefficient of friction μ_m is attained.

After applying a logarithm to both sides of Eq. (5.13) and rearranging in vector form

$$y = \ln \mu = \mathbf{U}\mathbf{\Theta}\,, \tag{5.14}$$

with $\mathbf{U} = [1, -\lambda, \lambda \ln \lambda, \ln \lambda, -v]$, $\mathbf{\Theta} = [p_1', p_2, p_3, p_4, p_5]^T$ and $p_1' = \ln p_1$. An estimated $\hat{\mathbf{\Theta}}$ of the vector $\mathbf{\Theta}$ can be obtained via a standard parameter adaptation algorithm (PAA)

$$\dot{\hat{\Theta}} = \Gamma\, \mathbf{U}^T\, \tilde{y}\,, \tag{5.15}$$

where $\tilde{y} = y - \hat{y} = \mathbf{U}(\mathbf{\Theta} - \hat{\mathbf{\Theta}}) = \mathbf{U}\,\tilde{\mathbf{\Theta}}$, $\Gamma = \Gamma^T > 0$ is a diagonal matrix of gains and assuming that μ can be accurately measured as discussed in section 4.

[9] A value of slip of 20% is considered high.

If the velocity is kept constant, the peak value of μ_m can be derived from Eq. (5.13),

$$\mu_m\Big|_{v=v_0} = p_1 e^{-p_2\lambda_m}\lambda_m^{(p_3\lambda_m+p_4)}e^{-p_5 v_0}\,, \tag{5.16}$$

where λ_m, the peak slip given by the solution to

$$p_3\lambda_m(\ln\lambda_m + 1) = p_2\lambda_m - p_4\,. \tag{5.17}$$

Notice that although the peak friction value in Eqs. (5.12) and (5.13) changes with velocity, the peak slip does not change with velocity in the same curves.

5.3.3 Controller Design

In this section a controller for emergency braking that exploits the knowledge of the μ surface is designed. It is assumed that vehicles are equipped with anti-lock braking systems (ABS) and that the longitudinal and angular velocities can be measured. In the case of AHS, the longitudinal velocity can be derived from infrastructure devices designed to facilitate vehicle's position detection (Varaiya 1993) and also can be obtained from the observer design given in section 4.1.

Define

$$\tilde{s} = s - s_m\,, \tag{5.18}$$

where $s_m = \hat{\lambda}_m\, v$ is the peak relative velocity that corresponds to the estimated peak slip $\hat{\lambda}_m$ at velocity v. s_m can be obtained from Eqs. (5.16) and (5.17) and the current estimation $\hat{\mathbf{\Theta}}$. Correspondingly, the velocity error could be defined as $\tilde{v} = v - v_d$, with v_d the desired velocity; however as for emergency braking $v_d = 0$, this definition of $\tilde{v}$ is not necessary.

The braking pressure P_b is set as

$$P_b = \frac{\hat{M}_b}{e}\left[(a+c)\mu + b + d\,v^2 - \zeta\tilde{s}\right]\,, \tag{5.19}$$

where $\hat{M}_b = 1/\hat{K}_b$, with $\hat{K}_b$ the estimated value of K_b and μ is derived from Eq. (5.10) under the assumption that the longitudinal acceleration can be measured.

Substituting Eq. (5.19) into Eq. (5.10) yields

$$\dot{s} = -\zeta\,\tilde{s} - K_b\tilde{M}_b\left[(a+c)\mu + b + d\,v^2 - \zeta\tilde{s}\right] \tag{5.20}$$

with $\tilde{M}_b = M_b - \hat{M}_b$.

Define

$$W = \frac{1}{2}\tilde{s}^2 + \frac{1}{2}v^2 + \frac{1}{2\xi}K_b\tilde{M}_b^2 + \frac{1}{2}\,\tilde{\mathbf{\Theta}}^T\Gamma^{-1}\tilde{\mathbf{\Theta}}\,. \tag{5.21}$$

Taking the time derivative of Eq. (5.21) and using Eqs. (5.11), (5.15) and (5.20) yields

$$\begin{aligned}\dot{W} = \tilde{s}\Big\{&-\zeta\,\tilde{s} - K_b\tilde{M}_b\left[(a+c)\mu + b + d\,v^2 - \zeta\tilde{s}\right]\\ &-\hat{\lambda}_m\dot{v}\Big\} + v\dot{v} + K_b\tilde{M}_b\dot{\tilde{M}}_b/\xi - \tilde{\mathbf{\Theta}}^T\Gamma^{-1}\left(\Gamma\mathbf{U}^T\tilde{y}\right)\end{aligned} \tag{5.22}$$

Choose $\dot{\tilde{M}}_b$ as

$$\dot{\tilde{M}}_b = \xi\ \tilde{s}\left[(a+c)\mu + b + d\ v^2 - \zeta\tilde{s}\right]\ . \tag{5.23}$$

Substitute Eq. (5.23) in Eq. (5.22) to get

$$\dot{W} = -\zeta\tilde{s}^2 + \dot{v}(\tilde{s}\hat{\lambda}_m + v) - \tilde{\mathbf{\Theta}}^T\mathbf{U}^T\mathbf{U}\tilde{\mathbf{\Theta}} \leq 0\,. \tag{5.24}$$

In the last step in Eq. (5.24) the facts that $\dot{v} \leq 0$, and $v + \tilde{s}\hat{\lambda}_m = v(1 + \hat{\lambda}_m(\hat{\lambda}_m - \lambda)) > 0$ were used. Eq. (5.24) implies that $\tilde{s}$, v, $\tilde{M}_b$ and $\tilde{\mathbf{\Theta}}$ are bounded. Straightforward calculations show that $\ddot{W}$ is bounded. Thus, applying Barbalat's Lemma, (Slotine and Li 1991), it follows that

$$\lim_{t\to\infty}\ \tilde{s} = \lim_{t\to\infty}\ v = \lim_{t\to\infty}\ \tilde{K}_b = \lim_{t\to\infty}\ \tilde{\mu} = 0\,, \tag{5.25}$$

and therefore stability of $s = s_m, v = 0$ follows. It is important to recall that only persistence of excitation will guarantee that $lim_{t\to\infty}\ \tilde{\mathbf{\Theta}} = \mathbf{0}$.

5.3.4 Underestimation of Friction Coefficient

The goal in this section is to find the conditions on Θ and $\hat{\Theta}$ under which

$$\hat{\lambda}_m \leq \lambda_m\,, \tag{5.26}$$

$$\hat{\mu}_m \leq \mu_m\,, \tag{5.27}$$

where μ_m is maximum coefficient of friction and λ_m the value of slip at which μ_m occurs. The corresponding estimated quantities are denoted as $\hat{\mu}_m$ and $\hat{\lambda}_m$, respectively. In order to prove Ineqs. (5.26) and (5.27) it is necessary to introduce some preliminary results.

Define the following function

$$f(\Theta,\lambda) = \frac{p_2}{p_3} - 1 - \ln\lambda - \frac{1}{\lambda}\frac{p_4}{p_3}\,, \tag{5.28}$$

which is obtained by taking the partial derivative in Eq. (5.14) with respect to λ and dividing by p_3, the third component of Θ. From Eqs. (5.14) and (5.28), λ_m and $\hat{\lambda}_m$ satisfy

$$f(\Theta,\lambda_m) = 0\,, \tag{5.29}$$

$$f(\hat{\Theta},\hat{\lambda}_m) = 0\,. \tag{5.30}$$

Notice that Eqs. (5.29) and (5.30) imply that there is always a slip point with maximum coefficient of friction for the sets of real and estimated parameters, respectively. Define

$$\bar{\lambda}_m = \arg\{\max_{\Theta,\lambda,v}\mu\}\,,\quad \underline{\lambda}_m = \arg\{\min_{\Theta,\lambda,v}\mu\} \tag{5.31}$$

and the interval $\Lambda_m = \left[0, \bar{\lambda}_m\right]$ [10].

[10] For most of the tires reported in the literature $\bar{\lambda}_m < 0.3$.

Lemma 2 *If $\lambda \in \Lambda_m$ and $\bar{\lambda}_m < p_4/p_3$, then the partial derivative of Eq. (5.28) satisfies*

$$\frac{\partial f}{\partial \lambda} \geq 0 \, .$$

Proof: See appendix B.

Lemma 3 *Assume Lemma 2 holds and*

$$\frac{p_2}{p_3} - \frac{\hat{p}_2}{\hat{p}_3} - \frac{1}{\bar{\lambda}_m}\left(\frac{p_4}{p_3} - \frac{\hat{p}_4}{\hat{p}_3}\right) \leq 0 \tag{5.32}$$

then $\hat{\lambda}_m \leq \lambda_m$.

Proof: See appendix B.

Remark 1 The condition in Ineq. (5.32) of Lemma 3 can be expressed in terms of the signs of $\tilde{p}_i, i = 2, 3, 4$ the parameter estimation errors. For comparable sizes of $\tilde{p}_i, i = 2, 3, 4$, and considering that $\bar{\lambda}_m << 1$, the choice of $\tilde{p}_3 < 0$ and $\tilde{p}_4 > 0$ is the most convenient in order for Ineq. (5.32) to hold. Once $\tilde{p}_3 < 0$ is chosen, making $\tilde{p}_2 < 0$ follows from Ineq. (5.32).

When the true parameters are fixed, the adaptation law in Eq. (5.15) can be rewritten as

$$\dot{\tilde{\Theta}} = -\Gamma \mathbf{U}(\lambda, v)^T \mathbf{U}(\lambda, v)\tilde{\Theta} = \mathbf{A}(\lambda, v)\tilde{\Theta} \, . \tag{5.33}$$

By Eqs. (5.25), Eq. (5.33) can be linearized about $\lambda = \hat{\lambda}_m$ and $v = 0$ to obtain

$$\dot{\tilde{\Theta}} = \mathbf{A}(\hat{\lambda}_m, 0)\tilde{\Theta} + \frac{\partial \mathbf{A}(\lambda, v)}{\partial \lambda}\left(\lambda - \hat{\lambda}_m\right) + \frac{\partial \mathbf{A}(\lambda, v)}{\partial v} v \, . \tag{5.34}$$

This linearization can be further simplified if the fact that the maximum coefficient of friction is attained when $v \to 0$. Thus, neglecting the velocity term in Eq. (5.13), it is possible to focus the analysis only in $p_1, \cdots, p_4$ the first four parameters of Θ when analyzing the point of slip where the maximum friction occurs. If the difference $\lambda - \hat{\lambda}_m$ is small and p_5 is ignored, Eq. (5.34) can be rewritten as

$$\dot{\tilde{\Theta}} = \mathbf{A}(\hat{\lambda}_m)\tilde{\Theta} \, . \tag{5.35}$$

where the vector Θ and matrix $\mathbf{A}$ only consider the first four elements of Θ, i.e., $p_1, \cdots, p_4$.

Solving Eq. (5.35), the elements of $\tilde{\Theta}(t)$ are given by

$$\begin{aligned}
\tilde{p}_1(t) &= \tilde{p}_1(t_0) - \gamma_1 \alpha(t_0) f/d \\
\tilde{p}_2(t) &= \tilde{p}_2(t_0) + \gamma_2 \hat{\lambda}_m \alpha(t_0) f/d \\
\tilde{p}_3(t) &= \tilde{p}_3(t_0) - \gamma_3 \hat{\lambda}_m \ln \hat{\lambda}_m \alpha(t_0) f/d \\
\tilde{p}_4(t) &= \tilde{p}_4(t_0) - \gamma_4 \ln \hat{\lambda}_m \alpha(t_0) f/d
\end{aligned} \tag{5.36}$$

where $\gamma_i; i = 1. \cdots, 4$, are the elements of the diagonal matrix $\Gamma > 0$,

$$\begin{aligned}
s_4 &= -(\gamma_1 + \gamma_2 \hat{\lambda}_m^2 + \gamma_3 \hat{\lambda}_m^2 \ln^2 \hat{\lambda}_m + \gamma_4 \ln^2 \hat{\lambda}_m) \, , \\
d &= \gamma_2\gamma_3\gamma_4 + \gamma_1\gamma_2\gamma_3 \ln^2 \hat{\lambda}_m + \gamma_1\gamma_3\gamma_4 \hat{\lambda}_m^2 + \gamma_1\gamma_2\gamma_4 \hat{\lambda}_m^2 \ln^2 \hat{\lambda}_m \, , \\
\alpha(t_0) &= \tilde{p}_1(t_0) - \hat{\lambda}\tilde{p}_2(t_0) + \hat{\lambda} \ln \hat{\lambda} \tilde{p}_3(t_0) + \ln \hat{\lambda} \tilde{p}_4(t_0) \, , \\
f &= \left[1 - e^{s_4(t-t_0)}\right] \, .
\end{aligned}$$

Lemma 4 *Assume there exists a time t_0 at which $\lambda \geq \underline{\lambda}_m$ and that the following conditions are satisfied:*

$$(i)\ \tilde{p}_1(t_0) \geq 0\,,\ \tilde{p}_2(t_0) \leq 0\,,\ \tilde{p}_3(t_0) \leq 0\,,\ \tilde{p}_4(t_0) \geq 0\,,$$
$$(ii)|\tilde{p}_i(t_0)| \leq \tilde{p}_{max}\,, i = 1, \cdots, 4,$$
$$(iii)\ Lemma\ 3\ holds\ for\ t_0\,,$$

Choose the gain matrix Γ in the PAA given by (5.15) according to

$$\gamma_1 < \frac{\tilde{p}_1(t_0)\ln^2\ \underline{\lambda}_m}{\delta}\,, \tag{5.37}$$
$$\gamma_2 < \frac{|\tilde{p}_2(t_0)|\ln^2\ \underline{\lambda}_m}{\delta\ \bar{\lambda}_m}\,, \tag{5.38}$$
$$\gamma_3 < \frac{|\tilde{p}_3(t_0)|\ln^2\ \underline{\lambda}_m}{\delta\ \bar{\lambda}_m \ln \bar{\lambda}_m}\,, \tag{5.39}$$
$$\gamma_4 > 1\,, \tag{5.40}$$
$$\frac{\gamma_3}{\gamma_2}|\ln \bar{\lambda}_m| \geq \max\left(1, \frac{\tilde{p}_3(0)}{\tilde{p}_4(0)}\right)\,, \tag{5.41}$$

with $\delta = \tilde{p}_{max}(1 + \bar{\lambda}_m + \bar{\lambda}_m \ln \bar{\lambda}_m)$.

Then Ineq (5.32) in Lemma 2 is satisfied and the estimated peak value for the longitudinal slip, $\hat{\lambda}_m$, satisfies

$$\hat{\lambda}_m(t) \leq \lambda_m(t)\,, \forall t \geq t_0$$

Proof: See appendix B.

Lemma 4 defines a region in the space of parameters and λ such that trajectories inside it, will remain in it. This region, however, does not include the case when $\lambda \approx 0$, that is expected to happen if vehicles are cruising before attempting emergency braking. To analyze the effect when λ is small consider the following lemma.

Lemma 5 *Assume that $\tilde{p}_1(0) \geq 0$, $\tilde{p}_2(0) \leq 0$, $\tilde{p}_3(0) \leq 0$, $\tilde{p}_4(0) \leq 0$, $\tilde{p}_5(0) \leq 0$ and $\frac{\tilde{p}_2(0)}{\tilde{p}_3(0)} \leq \frac{p_2}{p_3}$. By choosing $\gamma_i,\ i = 1, \ldots, 4$ as stated in Lemma 4 and in addition*

$$\gamma_4 \geq \gamma_{4m}, \tag{5.42}$$

where

$$\gamma_{4m} = \max\left\{-\frac{\tilde{p}_4(0)}{\tilde{p}_1(0)\ln \bar{\lambda}_m}\gamma_1,\ \frac{\tilde{p}_4(0)\bar{\lambda}_m}{\tilde{p}_2(0)\ln \bar{\lambda}_m}\gamma_2,\ \frac{\tilde{p}_4(0)\bar{\lambda}_m}{\tilde{p}_3(0)}\gamma_3\right\}$$

then $\exists\, t_0 > 0$ such that the conditions in Lemma 4 are satisfied under the adaptation law for $t \geq t_0$ when λ is initially small.

Proof: See appendix B.

The previous lemmas can be summarized in the following theorem.

Theorem 1 *Assume that the initial conditions for the adaptation law in Eq. (5.15) are such that $\tilde{p}_1 \geq 0$, $\tilde{p}_2 \leq 0$, $\tilde{p}_3 \leq 0$, $\tilde{p}_4 \leq 0$ and $\tilde{p}_5 \leq 0$. Let γ_4 to be large relative to $\gamma_i\,; i = 2, 3, 4$ as stated in conditions of Lemma 4. Then after a long enough time t_0 the estimated peak value for the longitudinal slip, $\hat{\lambda}_m$, satisfies*

$$\hat{\lambda}_m(t) \leq \lambda_m(t)\,; \forall t \geq t_0$$

Proof: See appendix B. Finally, the other desired result is proved in the following theorem.

Theorem 2 *Assume that Lemma 4 is satisfied and in addition*

$$\tilde{p}_1 - \tilde{p}_5 v - \tilde{p}_4(1 - \ln \underline{\lambda}_m) - \tilde{p}_3 \underline{\lambda}_m > 0\,, \tag{5.43}$$

then the estimated peak friction, $\hat{\mu}_m$ satisfies

$$\hat{\mu}_m \leq \mu_m$$

Proof: See appendix B.

Remark 2 Conditions on Theorem 2 are sufficient conditions for underestimation of μ_m. There are cases in which underestimation of μ_m can be achieved even when conditions in Theorem 2 are not satisfied. A more relaxed condition for underestimation of μ_m is that

$$\tilde{p}_1 - \tilde{p}_5 v - \tilde{p}_4(1 - \ln \hat{\lambda}_m) - \tilde{p}_3 \lambda_m + (\lambda_m - \hat{\lambda}_m)\left(\frac{p_4}{\hat{\lambda}_m} - p_3\right) > 0\,. \tag{5.44}$$

This condition does not depend on Lemma 4 and therefore is independent of the underestimation of λ_m.

5.3.5 Simulation Results

Data from Schuring (1976) tires #76, 81 and 137 is used to test the approximation presented in section 5.3.2 for the μ versus λ and v surface. All the tests were performed under the same road conditions, same tire pressures ($24psi$), same velocity ($30mph$) and same normal forces. The nominal $\mu - \lambda$ curve for the tires are shown in Figs. 5.10-5.12.

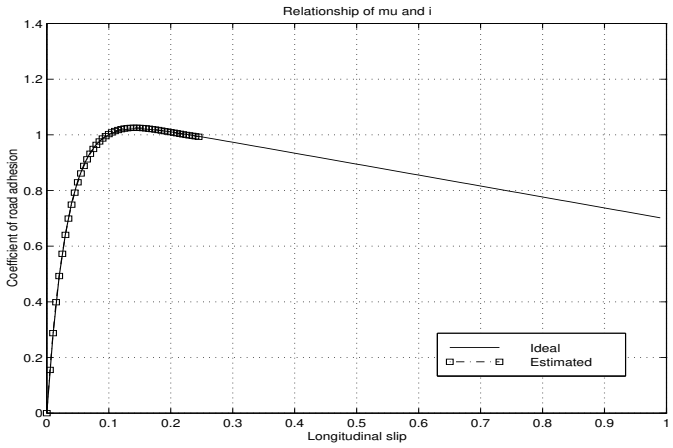

Figure 5.10: Coefficients of road adhesion μ and longitudinal slip λ by nominal and estimated values. Tire # 76.

Figs. 5.10-5.12 show that the proposed approximation in Eq. (5.13) fits very well the nominal formula of the road friction μ given by Eq.(5.12) in the region of $[0, \mu_{max}]$ which is the region of

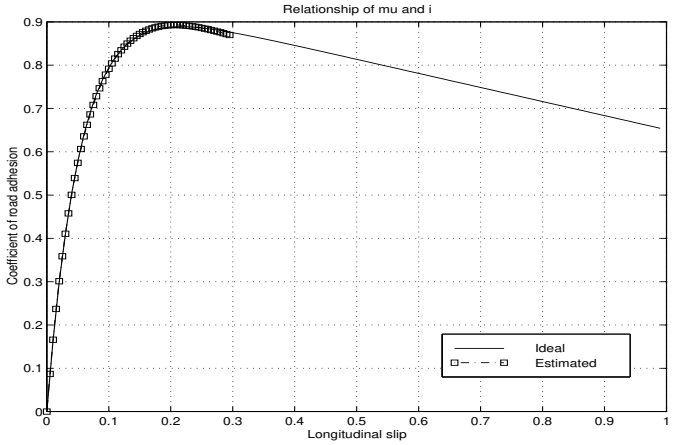

Figure 5.11: Coefficients of road adhesion μ and longitudinal slip λ by nominal and estimated values. Tire # 81.

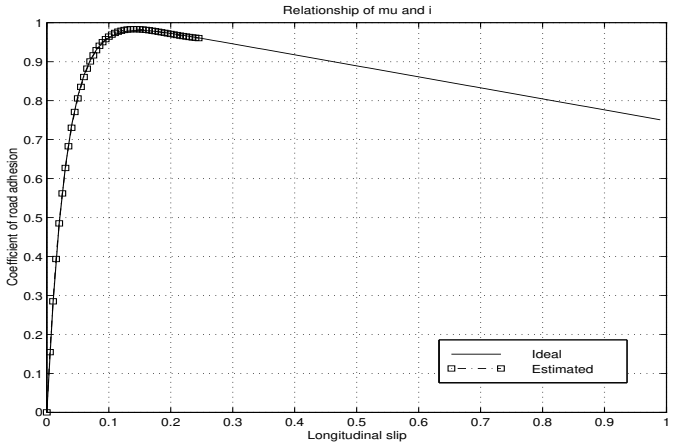

Figure 5.12: Coefficients of road adhesion μ and longitudinal slip λ by nominal and estimated values. Tire # 137.

interest. The velocity-dependent parameter p_5 is constant since the tests in (Schuring 1976) were performed at constant velocity.

Simulations of emergency braking maneuvers using the controller introduced in the previous section were performed. The "true parameters" for the approximation in Eq. (5.13) were obtained with an off-line test and are shown in Table 5.2 together with the real value of the brake system gain. Figs. 5.13-5.16 show several plots that illustrate typical simulation results for an emergency braking maneuver.

Fig. 5.17 (a) shows one example of the underestimation of the peak slip ratio when the initial values of the parameter estimates satisfy the conditions of the Theorems. Fig. 5.17 (b) shows the case when $\tilde{p}_1(0) < 0$ which violates one of the conditions in the Theorems. In this case underestimation of λ_m does not occur.

The emergency braking maneuver was accomplished in both simulation cases, even in the case when underestimation of λ_m was not achieved. This is happening because in the controller design an upper limit for the admissible value of the estimated point of maximum slip, namely $\bar{\lambda}_m$, was included. This limit allows the emergency braking maneuver to be performed, even when

the estimated friction curve is incorrect[11]. A bad estimation of λ_m produces, as expected, an increase in the distance that vehicles require for the emergency braking maneuver. If the tire/road friction estimation is to be used for traction control purposes other than emergency braking, the case in which underestimation is achieved (Fig. 5.17 (a)) is clearly a good approximation to the reference tire/road friction curve and would be useful for these other purposes. The other case, when underestimation is not achieved (Fig. 5.17 (b)) is not useful for traction control purposes.

Table 5.2: Parameters for the approximation in Eq. (5.13)

p_1	p_2	p_3	p_4	p_5	K_b
3.16	3.3	2.64	1.05	0.01	0.9

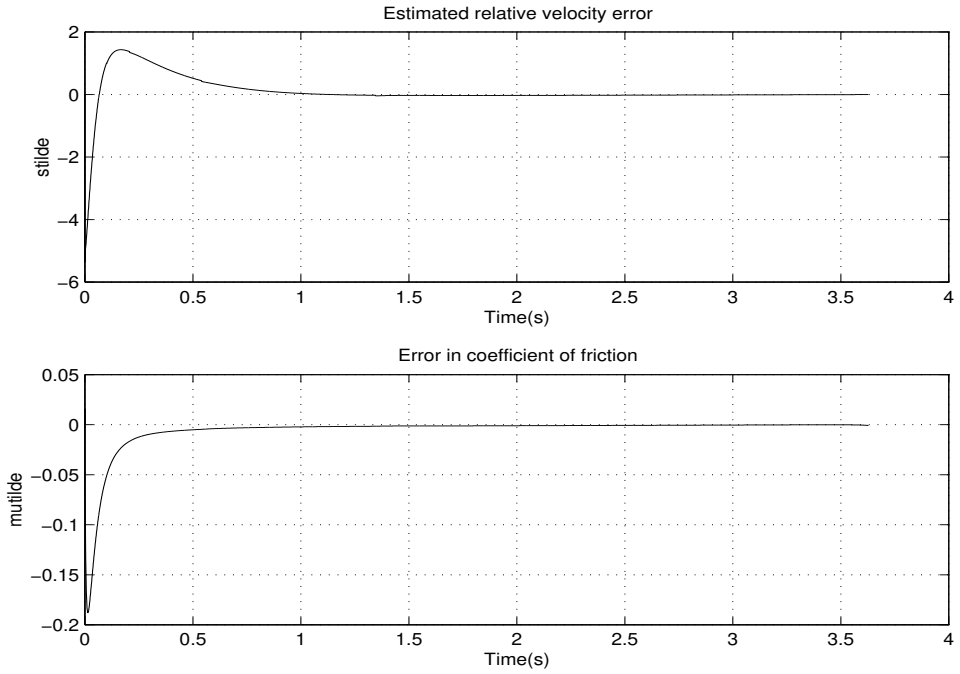

Figure 5.13: Error signals.

The use of this controller provides less chattering, as the controller avoids exceeding the peak slip in the current tire/road situation.

When there is not persistence of excitation and when the proper set of initial conditions is chosen for the estimation algorithms, the maximum friction and the point of maximum friction, of μ_m and λ_m, respectively are guaranteed to be underestimated.

This is a very desirable feature for the deployment of AHS, where it is of first importance to ensure a safe operation. For this purpose of safety, the information provided with the on-line tire/road identification scheme proposed in this report may be very useful for on-line safe spacing calculations in vehicles running under AHS or intelligent cruise control algorithms. The information can also be used by the road-side infrastructure to adjust on-ramp metering control.

[11] In the simulations here included, $\bar{\lambda}_m = 0.45$ was chosen.

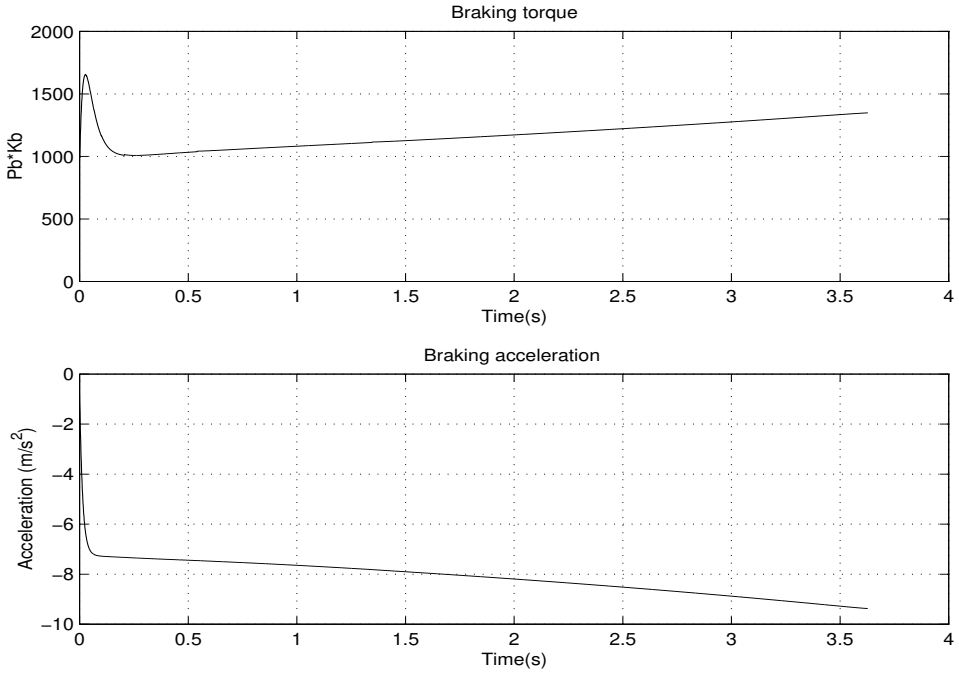

Figure 5.14: Braking torque and deceleration.

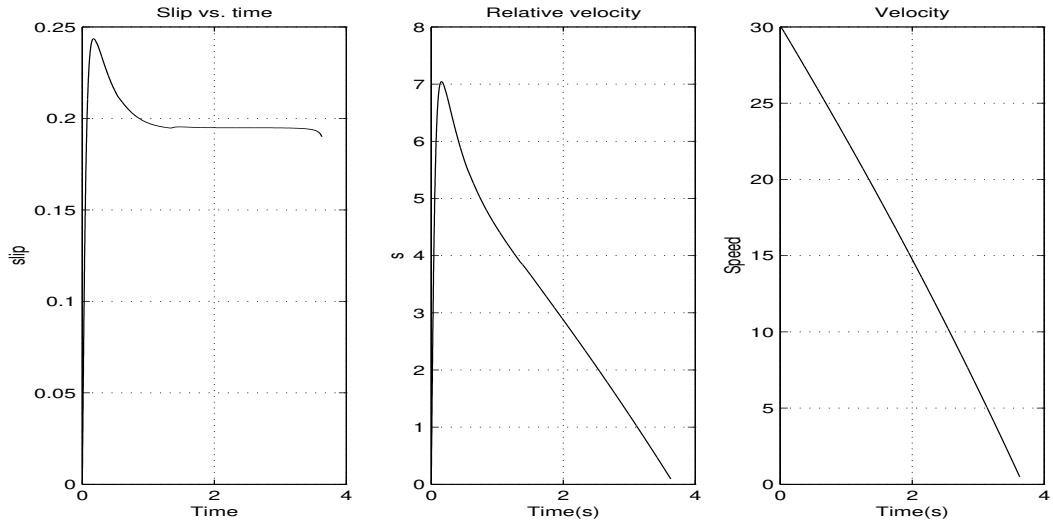

Figure 5.15: Slip and state evolution vs. time.

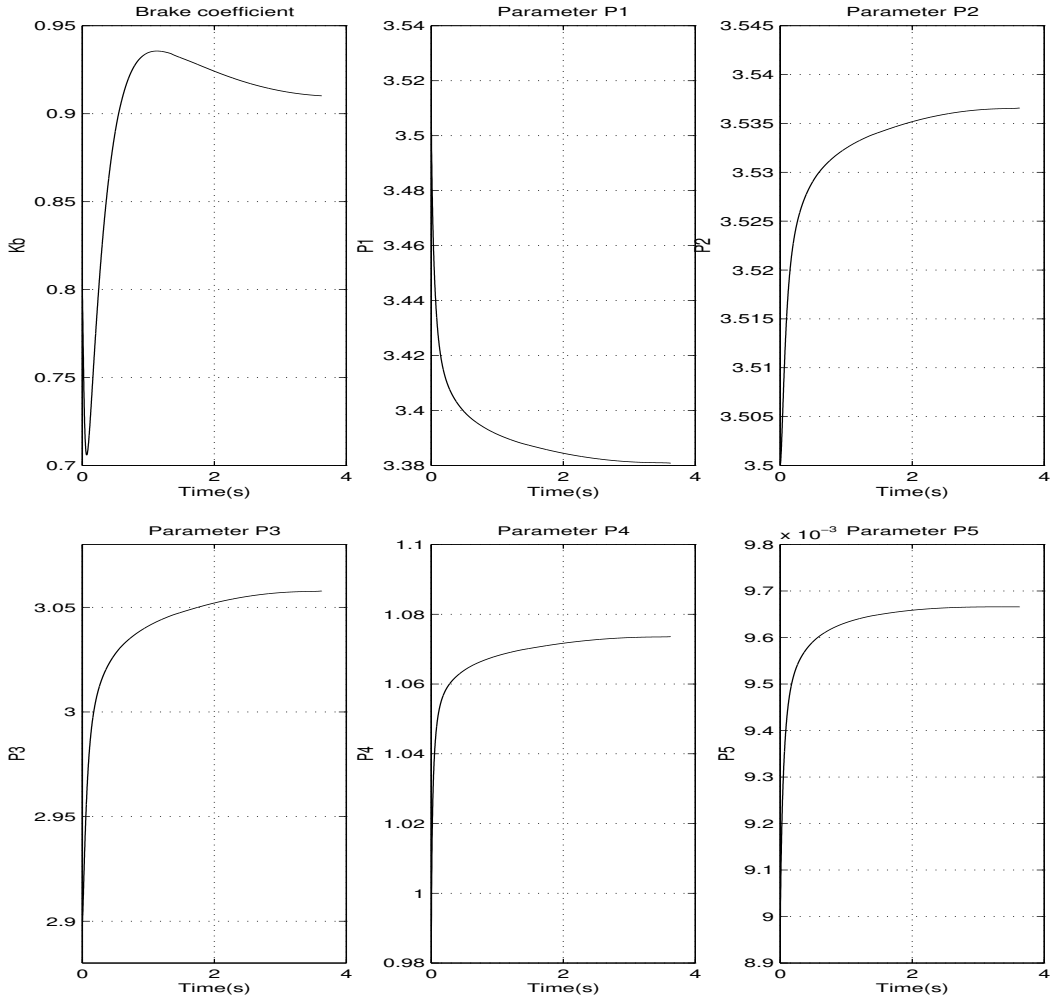

Figure 5.16: Adapted parameters.

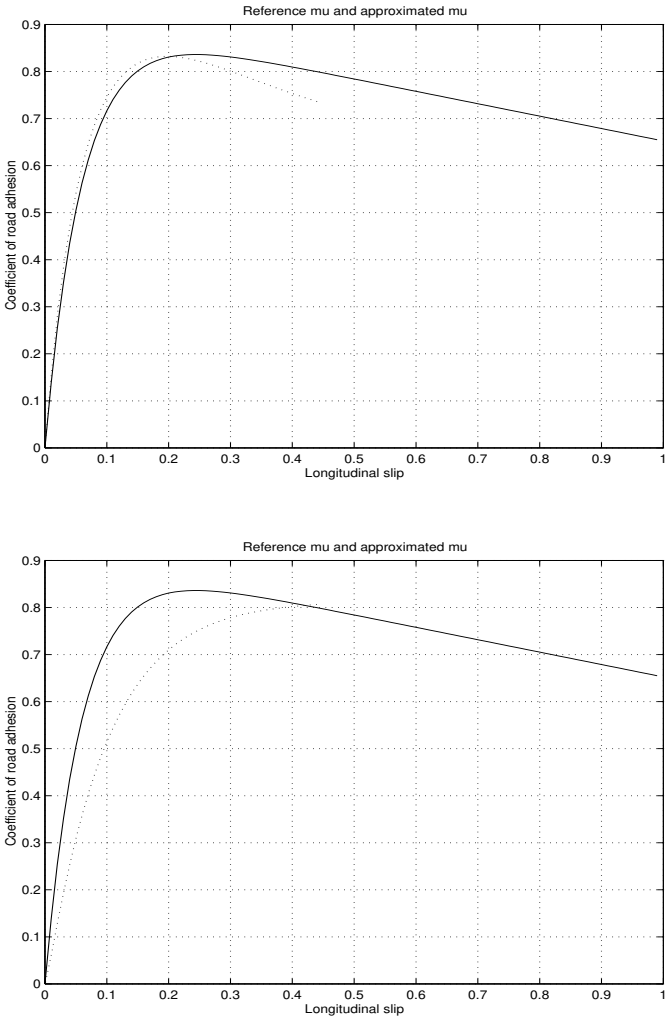

Figure 5.17: Reference friction μ (solid) and estimated friction $\hat{\mu}$ (dotted) (a) underestimation of λ_m and μ_m; (b) no underestimation of λ_m.

Chapter 6

Conclusions and Future Works

This report presented the design methodology and performance tests of a fault diagnostic and management system for the longitudinal vehicle controller of the PATH automated highway system (AHS). This new fault tolerant controller is able to detect, identify, and handle failures in all of the critical control components for the controller and has the ability to compensate for adverse environmental conditions.

The fault diagnostic system was developed in this project utilizes model-based techniques to diagnose faults in all of the sensors and actuators involved in the physical layer longitudinal controller. A method for detecting, identifying and estimating faults using linear least squares estimation was also presented. The fault diagnostic system was shown to work well when simulated with a detailed vehicle model incorporating realistic unmodeled dynamics. Experimental results using the intervehicle observer to detect and correct for radar faults were shown to work extremely effectively, while the limited performance of the engine dynamics observer requires further study.

The fault management system described in this project uses safe regulation layer control laws (Li *et al.* 1997) and equivalent safety results for the coordination layer (Hsu *et al.* 1994) so as to guarantee that the control strategies yield safe maneuvering of vehicles. Simulation results were presented that show the fault tolerant controllers ability to continue normal operation in the presence of non-severe faults and to transition from the normal mode to degraded mode of operation when a severe fault is detected. In addition, these results show that the fault management system can safely handle all faults in the set of sensor, actuators and communication devices involved in the longitudinal controller.

A performance structure which monitors the gradual degradations of operational conditions of AHS due to adverse environmental conditions and gradual wear of physical AHS components was also presented. A controller for emergency braking maneuvers of vehicles equipped with ABS is designed which uses estimates of the tire/road characteristics and an overall brake system gain to achieve maximum braking effort during the entire maneuver. The stability of the controller was proven and the controllers performance was shown to be in accordance with the theoretical findings via simulations.

Further research is currently underway in MOU 373 to further develop several ideas related to this research. First, one of the underlying assumptions for the fault diagnostic system is that only one fault may occur at any given time. However, this condition is not true in general. Therefore, the detection of multiple simultaneous faults is currently being investigated under MOU 373. Furthermore, integration of the longitudinal fault tolerant controller and a similar system for the lateral control system developed by Professor Tomizuka's research group at UC Berkeley (Surya-

narayanan and Tomizuka 2000) to provide a complete fault tolerant vehicle control system is also ongoing. The third topic under research concerns the static relationship between the friction coefficient and longitudinal tire slip ratio used in the tire/road friction estimation scheme proposed in this report. In reality, the time-varying nature of this relationship limits the applicability of this estimator. Recently, a dynamic approach to estimate the frictions between the road and tire has been investigated (Yi *et al.* 2000). The final task in progress is the implementation and testing of the complete system on the PATH experimental vehicles at Richmond Field Station.

Bibliography

Agogino, A., K. Goebel, and S. Alag (1997). Intelligent Sensor Validation and Sensor Fusion for Vehicle Guidance Using Probabilistic and Fuzzy Methods. PATH Research Report UCB-ITS-PRR-97-31, Institute of Transportation Studies, University of California at Berkeley.

Alvarez, L. (1996). *Automated Highway Systems: Safe Platooning and Traffic Flow Control*. Ph. D. thesis, Department of Mechanical Engineering, University of California at Berkeley.

Alvarez, L. and R. Horowitz (1999). Safe platooning in AHS. Part I: safety regions design. *Journal of Vehicle Systems Dynamics 32*(1), 23–56.

Alvarez, L. and J. Yi (1999). Adaptive Emergency Braking Control in Automated Highway System. In *Proceedings of* 38^{th} *IEEE Conference of Decision and Control*, Phoenix, AZ, pp. 3740–3745.

Alvarez, L., J. Yi, and R. Horowitz (2000). Adaptive Emergency Brake Control in AHS with Underestimation of Friction Coefficient. In *Proceedings of American Control Conference*, Chicago, IL, pp. 574–579.

Antoniotti, M., A. R. Deshpande, F. Dufraisse, and M. Zandonadi (1998). *The Sensor Architecture in SmartAHS*. Berkeley, California: California PATH. available at website, `http://www.path.berkeley.edu/smart-ahs/sensors.html`.

Bakker, E., L. Nyborg, and H. Pacejka (1987a). Tyre Modelling for Use in Vehicle Dynamic Studies. Society of Automotive Engineers Paper # 870421.

Bakker, E., L. Nyborg, and H. B. Pacejka (1987b). Tyre Modeling for Use in Vehicle Dynamics Studies. *SAE Transactions* (870421), 190–204.

Banks, S. (1981). A note on nonlinear observers. *Int. Journal of Control 34*, 185–190.

Basseville, M. and I. Nikiforov (1993). *Detection of Abrupt Changes*. Prentice Hall.

Beard, R. V. (1971). *Failure accommodation in linear systems through self-reorganization*. Ph. D. thesis, Massachusetts Institute of Technology, Cambridge, MA.

Bow, S.-T. (1992). *Pattern Recognition and Image Preprocessing*. Marcel Dekker, Inc.

Burckhardt, M. (1993). *Fahrwerktechnik: Radschlupfregelsysteme*. Germany: Vogel-Verlag.

Canudas de Wit, C. and R. Horowitz (1999). Observers for Tire/Road Contact Friction using only wheel angular velocity information. In *Proceedings of* 38^{th} *IEEE Conference of Decision and Control*, Phoenix, AZ.

Canudas de Wit, C., H. Olsson, K. Åström, and P. Lischinsky (1995). A New Model for Control of Systems with Friction. *IEEE Transactions on Automatic Control 40*(3), 419–425.

Canudas de Wit, C. and P. Tsiotras (1999). Dynamic Tire Friction Models for Vehicle Traction Control. In *Proceedings of* 38^{th} *IEEE Conference of Decision and Control*, Phoenix, AZ.

Carbaugh, J., L. Alvarez, P. Y. Chen, and R. Horowitz (1997). SmartPATH Regulation Layer Implementation: A User's Guide. PATH Research Reports UCB-ITS-PRR-97-48, Institute of Transportation Studies, University of California at Berkeley.

Chen, P. Y., L. Alvarez, and R. Horowitz (1997). Trajectory Design and Implementation of Longitudinal Maneuvers on Automated and Transition Lanes. PATH Research Reports UCB-ITS-PRR-97-49, Institute of Transportation Studies, University of California at Berkeley.

Cho, D. and H. J.K. (1989, December). Automotive powertrain modeling for control. In *ASME Transactions on Dynamic Systems, Measurements and Control*, Volume 111.

Cho, D.-I. (1987). *Nonlinear Control Methods for Automotive Powertrain Models*. Ph. D. thesis, Department of Mechanical Engineering, MIT, Boston, MA.

Chung, R. K. D. W., D. Malladi, R. Chen, J. L. Speyer, and D. Mingori (1996). Fault Detection and Identification with Application to Advanced Vehicle Control Systems: Final Report. PATH Research Report UCB-ITS-PRR-96-25, Institute of Transportation Studies, University of California at Berkeley.

Chung, R. K. D. W., D. Malladi, R. Chen, J. L. Speyer, and D. Mingori (1997). Fault Detection and Identification with Application to Advanced Vehicle Control Systems. PATH Research Report UCB-ITS-PRR-97-51, Institute of Transportation Studies, University of California at Berkeley.

Deshpande, A. R., A. Göllü, and L. Semenzato (1997). SHIFT *Reference Manual*. Berkeley, California: California PATH, also `http://www.path.berkeley.edu/shift`.

Eskafi, F. (1996). *Modeling and Simulation of the Automated Highway Systems*. Ph. D. thesis, Department of Electrical Engineering and Computer Sciences, University of California at Berkeley.

Eskafi, F. (1998). Communication Structure for Automated Highway System. California PATH presentation slides.

Frank, P. (1990). Fault diagnosis in dynamic systems using analytical and knowledge-based redundancy. *Automatica 26*(3), 459–474.

Garg, V. (1995). *Fault Detection in Nonlinear Systems*. Ph. D. thesis, Department of Mechanical Engineering, University of California at Berkeley.

Garg, V. and K. Hedrick (1995, June). Fault Detection Filters for a Class of Nonlinear Systems. In *The American Control Conference*, Seattle, Washington, pp. 1647–1651.

Gerdes, J. and K. Hedrick (1995). Brake System Requirements for Platooning on an Automated Highway. In *the American Control Conference*, Seattle, Washington, pp. 165–169.

Gerdes, J. C. (1996). *Decoupled Design of Robust Controllers for Nonlinear Systems: As Motivated by and Applied to Coordinated Throttle and Brake Control for Automated Highways*. Ph. D. thesis, Department of Mechanical Engineering, University of California, Berkeley, CA.

Gertler, J. (1988, December). Survey of model-based failure detection and isolation in complex plants. *IEEE Control Systems Magazine*, 3–11.

Godbole, D., J. Lygeros, E. Singh, A. Deshpande, and A. Lindsey (2000). Communication Protocols for a Fault-Tolerant Automated Highway Systems. *IEEE Transactions on Control Systems Technology 8*(5), 787–800.

Gustafsson, F. (1997). Slip-based Tire-road Friction Estimation. *Automatica 33*(6), 1087–1099.

Harned, J., L. Johnston, and G. Scharpf (1969). Measurement of Tire Brake Force Characteristics as Related to Wheel Slip (Antilock) Control System Design. *SAE Transactions 78*(690214), 909–25.

Horowitz, R., S. Sastry, P. Varaiya, L. Alvarez, K. Lueng, C. Toy, and D. Gulick (1998). Emergency Vehicle Maneuvers and Control Laws for Automated Highway Systems. PATH Research Reports to Caltrans 98-C2, Institute of Transportation Studies, University of California at Berkeley.

Hsu, A., F. Eskafi, S. Sachs, and P. Varaiya (1994). Protocol Design for an Automated Highway System. *Discrete Event Dynamic Systems 2*(1), 4–16.

Isermann, R. (1984). Process fault detection based on modeling and estimation methods - a survey. *Automatica 20*(4), 387–404.

Isermann, R. (1997). Supervision,fault detection and diagnosis of technical systems. Notes from the Tutorial workshop of the 1997 American Control Conference.

Khalil, H. (1996). *Nonlinear Systems* (2nd ed.). NJ: Prentice Hall.

Kiencke, U. (1993). Realtime Estimation of Adhesion Characteristic Between Tyres and Road. In *Proceedings of the IFAC World Congress*, Volume 1.

Krstic, M., I. Kanellakopoulos, and P. Kokotovic (1995). *Nonlinear and Adaptive Control Design*. John Wiley and Sons, Inc.

Lee, H. and M. Tomizuka (1995). Adaptive Traction Control. PATH Research Report UCB-ITS-PRR-95-32, Institute of Transportation Studies, University of California at Berkeley.

Li, P., L. Alvarez, and R. Horowitz (1997). AVHS Safe Control Laws for Platoon Leaders. *IEEE Transactions on Control Systems Technology 5*(6), 614–628.

Lindsey, A. E. (1997). *Design, Verification and Simulation of Communication Protocols for a Fault Tolerant Automated Highway System*. Ph. D. thesis, Department of Electrical Engineering and Computer Sciences, University of California at Berkeley.

Liu, Y. and J. Sun (1995, June). Target Slip Tracking Using Gain-Scheduling for Antilock Braking Systems. In *The American Control Conference*, Seattle, Washington, pp. 1178–82.

Lygeros, J., D. Godbole, and M. Broucke (2000). A Fault Tolerant Control Architecture for Automated Highway Systems. *IEEE Transactions on Control Systems Technology 8*(2), 205–219.

Maciuca, D. (1997). *Nonlinear Robust and Adaptive Control with Application to Brake Control for Automated Highway Systems*. Ph. D. thesis, Department of Mechanical Engineering, University of California, Berkeley, CA.

McMahon, D. (1994). *Robust Nonlinear Control of Uncertain Systems: An Application to Intelligent Vehicle Highway Systems*. Ph. D. thesis, Department of Mechanical Engineering, University of California, Berkeley, CA.

Moskwa, J. (1988). *Automotive Engine Modeling for Real Time Control*. Ph. D. thesis, Department of Mechanical Engineering, MIT, Boston, MA.

Murgier, V. (1998). *SmartAHS Components for Communication Simulation*. Berkeley, California: California PATH. available at website, *http://www.path.berkeley.edu/smart-ahs/sahs-manual/communication_devices.html*.

Patwardhan, S. (1994a). *Fault Detection and Tolerant Control for Lateral Guidance of Vehicles in Automated Highways*. Ph. D. thesis, Department of Mechanical Engineering, University of California, Berkeley, California.

Patwardhan, S. (1994b). *Fault Detection and Tolerant Control for Lateral Guidance of Vehicles in Automated Highways*. Ph. D. thesis, Department of Mechanical Engineering, University of California, Berkeley, CA.

Peng, H. (1992). *Vehicle Lateral Control for Highway Automation*. Ph. D. thesis, Department of Mechanical Engineering, University of California, Berkeley, CA.

Pham, H. (1996). *Combined Lateral and Longitudinal Control of Vehicles for the Automated Highway System*. Ph. D. thesis, Department of Mechanical Engineering, University of California, Berkeley, CA.

Raghavan, S. and J. Hedrick (1994). Observer design for a class of nonlinear systems. *Int. Journal of Control 59*, 515–528.

Rajamani, R. and Y. Cho (1998). Existence and design of observers for nonlinear systems: Relation to distance to unobservability. *Int. Journal of Control 69*, 717–731.

Rajamani, R., K. Hedrick, and A. Howell (1997). A Completed Fault Diagnostic System for Longitudinal Control for Automated Vehicles. In *Proceedings of Symposium on Advanced Automotive Control, ASME International Congress*.

Rajamani, R., A. Howell, C. Chen, and J. Hedrick (1997, November). A Complete Fault Diagnostic System for the Longitudinal Control of Automated Vehicles. In *The ASME Winter Conference*, Dallas, Texas.

Ray, L. R. (1997). Nonlinear Tire Force Estimation and Road Friction Identification: Simulation and Experiments. *Automatica 33*(10), 1819–1833.

Ross, T. (1995). *Fuzzy logic with engineering applications*. McGraw-Hill.

Schuring, D. J. (1976). Tire Parameter Determination. DOT HS-802 089, Calspan Corporation.

Sengupta, R. (1999). Diagnosis and Communication in Distributed Systems. PATH Research Report UCB-ITS-PRR-99-16, Institute of Transportation Studies, University of California at Berkeley.

Simsek, H. T., R. Sengupta, S. Yovine, and F. Eskafi (1999). Fault Diagnosis for Intra-Platoon Communications. PATH Research Report UCB-ITS-PRR-99-24, Institute of Transportation Studies, University of California at Berkeley.

Slotine, J.-J. E. and W. Li (1991). *Applied Nonlinear Control*. USA: Prentice-Hall.

Suryanarayanan, S. and M. Tomizuka (2000). Observer Based "Look-Ahead" Scheme for Fault Tolerant Lateral Control of Automated Vehicle. In *The Proceedings of the 5th Advanced Vehicle Control Conference*, Ann Arbor, MI.

Swaroop, D. (1994). *String Stability of Interconnected Systems: An Application to Platooning in Automated Highway Systems*. Ph. D. thesis, Department of Mechanical Engineering, UC Berkeley.

Swaroop, D., J. Gerdes, and H. J.K. (1996, December). Dynamic surface control of nonlinear systems. In *35th IEEE Conference on Decision and Control*, Kobe, Japan. IEEE.

Szostak, H. T., R. W. Allen, and T. J. Rosenthal (1988). Analytical Modeling of Driver Response in Crash Avoidance Manuevering. Volume II: An Interactive Tire Model for Driver/Vehicle Simulation. Report no. DOT HS 807-271, U.S. Department of Transportation.

Varaiya, P. (1993). Smart Cars on Smart Roads: Problems of Control. *IEEE Transactions on Automatic Control 38*(2), 195–207.

Willsky, A. S. (1976). A survey of design method for failure detection systems. *Automatica 12*, 601–611.

Yi, J., L. Alvarez, R. Horowitz, and C. Canudas de Wit (2000). Adaptive Emergency Braking Control in Automated Highway System Using Dynamic Tire/Road Friction Model. In *Proceedings of* 39^{th} *IEEE Conference of Decision and Control*, Sydney, Australia.

Yi, K. and T. Jeong (1998). Observer Based Estimation of Tire-road Friction for Collision Warning Algorithm Adaptation. *JSME International Journal 41*(1), 116–124.

Appendix A

SmartAHS Implementation

The vehicle model, controllers, and diagnostic systemsr developed throughout this report have been implemented in the SHIFT programming language developed at PATH. The SHIFT programming language is designed to simulate systems described by finite state machines using an object oriented programming style. A complete description of SHIFT is beyond the scope of this report, however the interested reader can find more information at (Deshpande, Göllü, and Semenzato 1997). For the remainder of this appendix, it will be assumed that the reader is familiar with SHIFT and object oriented programming.

A.1 Vehicle Models

The vehicle models are described by a set of SHIFT types that represent the various subsystems and physical components. At the most abstract level, the parent type VehicleDynamics represents a standardized set of inputs and outputs necessary for any vehicle model. Each specific model is a child type which inherits these inputs and outputs from the VehicleDynamics parent type. Four vehicle models have currently been implemented in SHIFT to allow the user to choose an appropriate model for their simulation based on the tradeoff of model fidelity versus computational complexity. The basic inheritance tree for these four vehicle models is shown in Figure A.1.

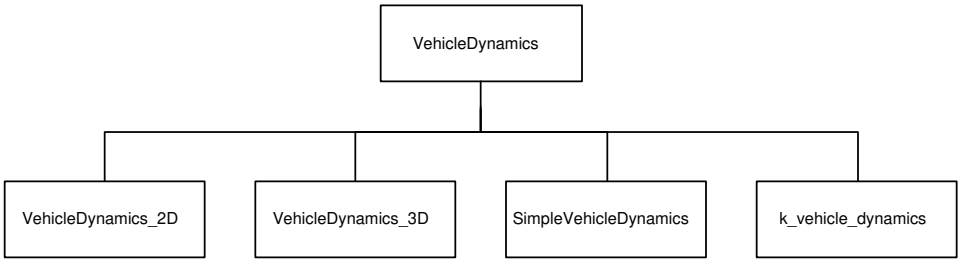

Figure A.1: Basic inheritance hierarchy for the `VehicleDynamics` type

This inheritance framework and the related vehicle models have been incorporated into a set of software libraries called SmartAHS. The purpose of this package is to provide a general automated highway simulation environment to researchers in the field. The vehicle models in SmartAHS were developed in conjunction with this project, however the basic SmartAHS models have been modified to suit the simulation of the fault diagnostic and management systems. The following

four sections will describe the key mathematical relationships of the modified vehicle models and their implementation in SHIFT. They will be presented in order of decreasing complexity, ie. the most complex model is presented in Section A.1.1 while the simplest is described in Section A.1.4.

A.1.1 `VehicleDynamics_3D` type

The `VehicleDynamics_3D` type represents the full 6 degree of freedom linear and rotational model described in Chapter 2. However, the `VehicleDynamics_3D` type is simply a container, since all of the dynamics associated with this model have been separated into individual internal types. This separation allows for reuse of common code throughout different vehicle models and a simplified means of modifying the vehicle model.

A basic block diagram of the internal structure of the `VehicleDynamics_3D` type in SHIFT is shown in Figure A.2. Although the role of each type roughly follows that of a specific sections in Chapter 2, a brief description of each type is as follows:

1. Powertrain: The Powertrain type contains the dynamic models for the engine, intake manifold, torque converter, transmission, and wheels. The close interaction of these dynamics, as well as the discrete change in dynamics due to torque converter locking, requires the use of such a complicated representation of the powertrain. However, several internal types are used to simplify the code as shown in Figure A.3.

2. Brake: The Brake type contains both the direct master cylinder control and vacuum booster models of the braking system. The type of model used is set at the start of the simulation.

3. RigidBody_3D: The `RigidBody_3D` type models the six degree of freedom dynamics associated with the vehicle body.

4. Moments_3D: The `Moments_3D` type is used to calculate the moments acting on the rigid body via the forces acting on the body and the body's speed.

5. Suspension: The `Suspension` type models the simplified suspension system presented in Section 2.4.

In addition to these internal types, two external types are also required by `VehicleDynamics_3D`; the Parameters type and the InitialConditions type. The Parameters type contains all of the necessary vehicle parameters needed for the any of the models described in Appendix A. The InitialConditions type sets the initial values of the model states based on a given initial speed and gear. These external types provide additional flexibility in creating vehicle models of different passenger cars at various initial conditions.

A.1.2 `VehicleDynamics_2D` type

While the three dimensional vehicle model presented in Chapter 2 provides a very high fidelity representation of a real vehicle, the three dimensional aspects of the model may be overly complex for some applications. For studies of vehicle dynamics under normal conditions, ie. no extreme braking or turning maneuvers, a two dimensional model can suffice.

The two dimensional vehicle model implemented in the `VehicleDynamics_2D` type is a simplified version of the six degree of freedom model in which the pitch, roll, and bounce dynamics

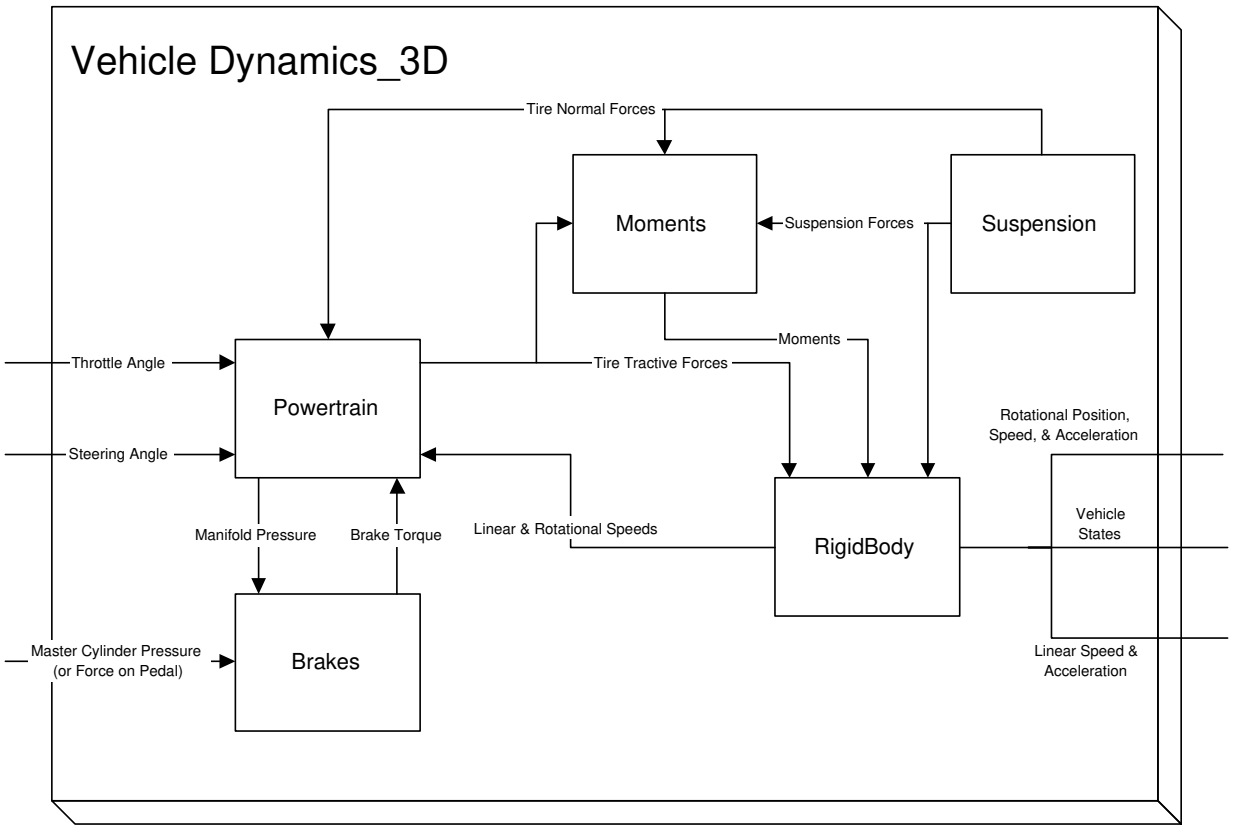

Figure A.2: Schematic of the `VehicleDynamics_3D` type

have been ignored. Grade and banking of the road are also neglected. Since much of the model presented in Chapter 2 still holds, the remainder of this section will only describe the changes made to the governing equations for the model.

Sprung Mass Dynamics Based on the simplifications discussed above, the equations of motion for the sprung mass reduce to

$$\begin{aligned}
\ddot{x} &= \frac{\sum_{i=1}^{4} F_{txi} - T_{rr} - c_x \dot{x}^2 \text{sign}(\dot{x})}{M} + \dot{y}\dot{\epsilon} \\
\ddot{y} &= \frac{\sum_{i=1}^{4} F_{tyi} - c_y \dot{y}^2 \text{sign}(\dot{y})}{M} - \dot{x}\dot{\epsilon} \\
I_z \ddot{\epsilon} &= l_1(F_{ty1} + F_{ty2}) - l_2(F_{ty3} + F_{ty4}) - \frac{1}{2}(s_{b1}(F_{tx1} - F_{tx2}) + s_{b2}(F_{tx3} - F_{tx4}))
\end{aligned}$$

Suspension System Since the bounce, or vertical, dynamics of the vehicle are ignored, the suspension model is neglected. The results of this simplification are that the suspension forces (F_{pi}) are constant, and equal to one quarter of the weight of the vehicle.

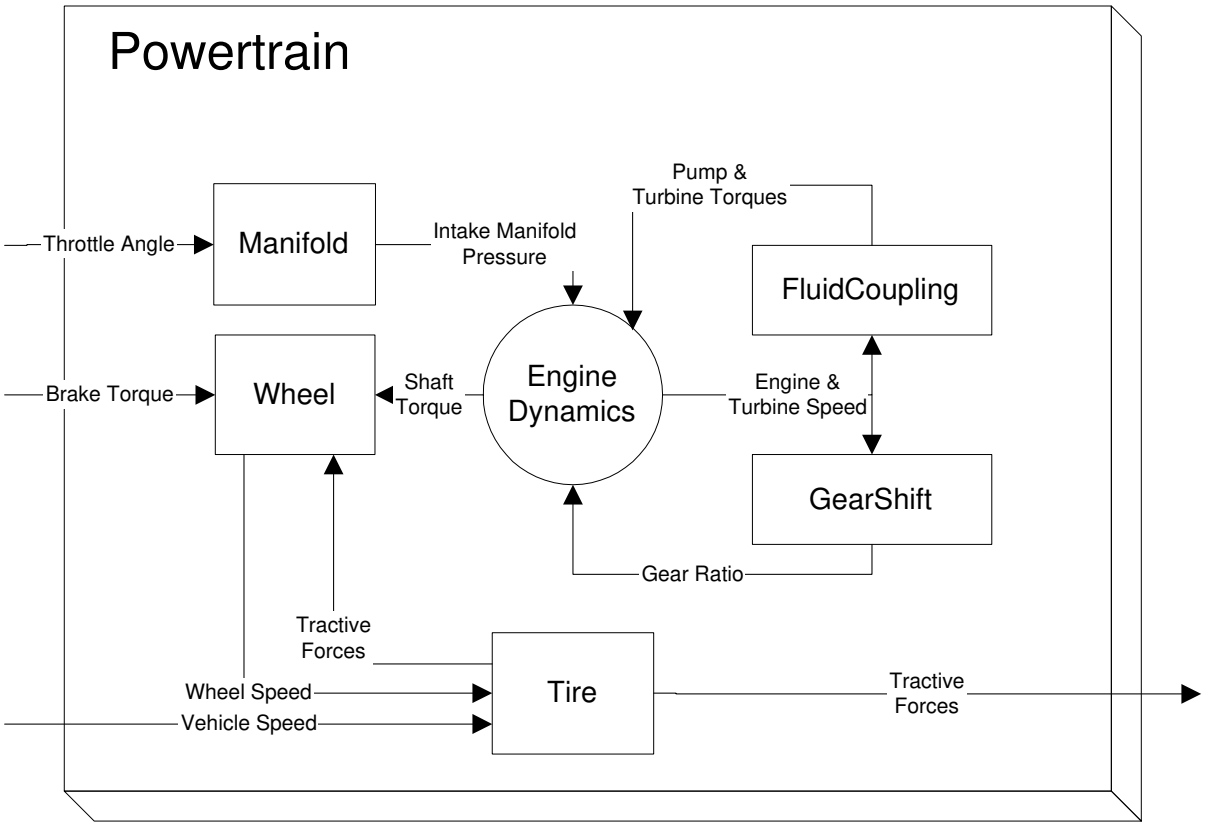

Figure A.3: Schematic of the `Powertrain` type

Tire Model From the simplification of the suspension forces, only the last two equations presented in Section 2.6 change as follows

$$F_{txi} = F_{tx}(\lambda_i, \zeta_i, \frac{Mg}{4}, \text{RC(skid number)})$$
$$F_{tyi} = F_{ty}(\lambda_i, \zeta_i, \frac{Mg}{4}, \text{RC(skid number)})$$

The `VehicleDynamics_2D` type has almost the same basic structure in SHIFT as the `VehicleDynamics_3D` type, since they differ primarily in the rigid body dynamics. The only difference is that the Suspension type is not present because the vertical dynamics of the vehicle are neglected. A simplified block diagram of the `VehicleDynamics_2D` type is shown in Figure A.4.

A.1.3 `SimpleVehicleDynamics` type

The two dimensional model can be further simplified by reducing the complexity of the internal subsystems in the powertrain and the tire model. The following three subsections will describe the simplifications and their impact upon the two dimensional vehicle model presented in Section A.1.2.

Powertrain The simplifications for the powertrain model are based on the following assumptions:

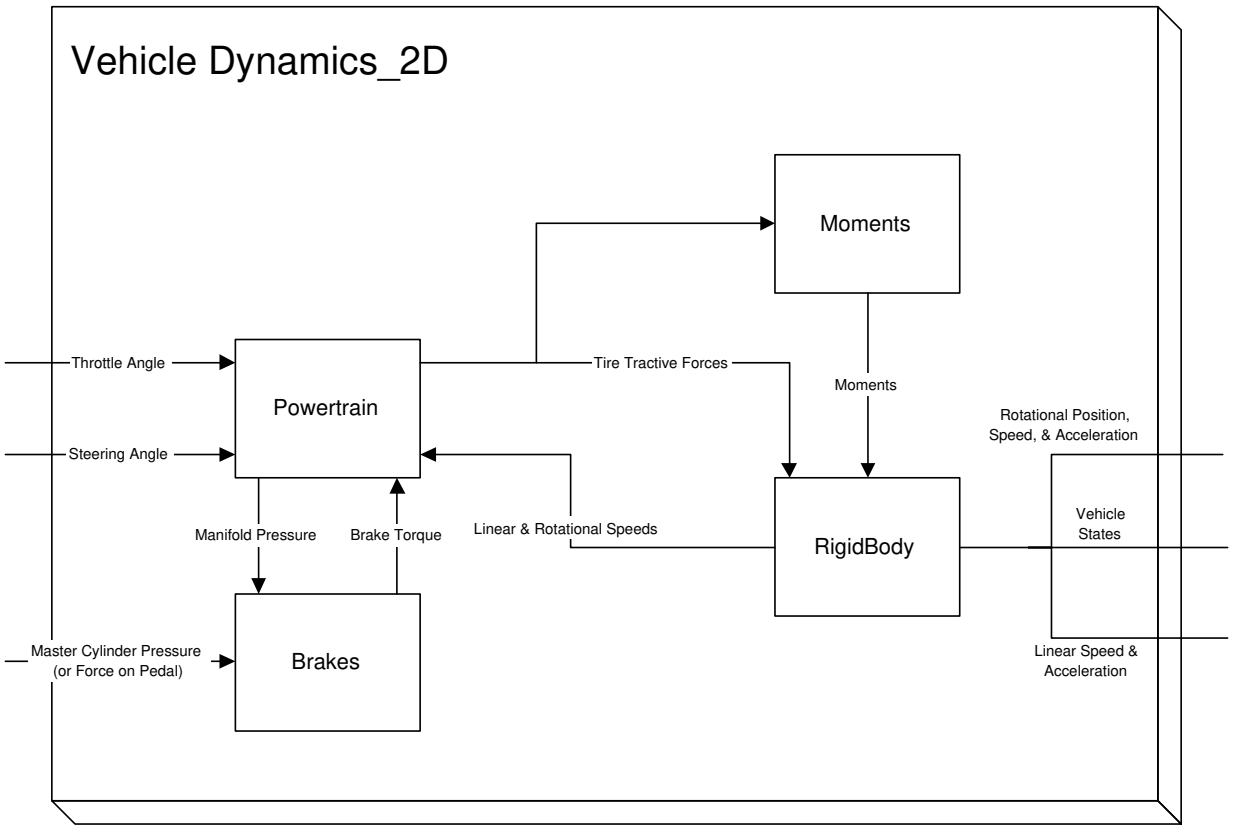

Figure A.4: Schematic of the `VehicleDynamics_2D` type

- The torque converter is locked and the transmission is rigid. This implies that the angular wheel speed of the driven wheels and the engine are proportionally related by the gear ratio. Limitations of this assumption are that low speed simulation of vehicle dynamics cannot be performed, nor can gear shifting be simulated.
- Intake manifold and throttle actuator dynamics are neglected.

The result of these assumptions is that the powertrain and wheel dynamics can be lumped together into a single differential equation

$$(I_e + I_t + R^{*2} I_w)\dot{\omega}_e = T_{net}(\omega_e, \alpha) - R^*(T_{brake} + h\sum_{i=1}^{4} F_{txi})$$

Under the assumptions above, the engine, turbine and wheel speeds are related by

$$\omega_w = R^*\omega_e = R^*\omega_t$$

Brake System To reduce the complexity of the vehicle model, only direct control of the master cylinder pressure is modeled.

Tire Model By assuming the low slip conditions exist between the tires and ground, the tire forces can be shown to linear functions of the longitudinal slip and slip angle. This assumption

constrains vehicle dynamics simulations to be performed on well paved roads. While the calculations for the tire velocity, longitudinal slip, and slip angle are identical to that presented in Section 2.6, the force relationships are now described by

$$\begin{aligned} F_{txi} &= K_{xslip}\lambda_i \\ F_{tyi} &= K_{yslip}\zeta_i \end{aligned}$$

The structure of the SimpleVehicleDynamics type in SHIFT is significantly different than the previously described model because of its simplicity. The main structural change is that the dynamics of each subsystem have been included in a single type. For example, all of the powertrain and rigid body dynamics for the simplified two-dimensional vehicle model are included in the `SimpleVehicleDynamics` type. This combination of dynamics reduces the amount of code, however a different `create` statement must be used in order to properly initialize all of the state variables.

A.1.4 `k_vehicle_dynamics` type

The vehicle models presented in the previous sections of this chapter describe the vehicle as a set of differential equations describing both the external and internal dynamics of the vehicle. For large scale simulations, even the simplified two dimensional model in Section A.1.3 may be computationally expensive. In these cases, a vehicle model based solely on simple kinematics is sufficient. This kinematic model can easily be written as the following set of differential equations

$$\begin{aligned} \ddot{x} &= u_x \\ \dot{y} &= u_y \end{aligned}$$

where direct control of the vehicle's longitudinal acceleration and lateral velocity is assumed via inputs u_x and u_y, respectively.

The structure of the `k_vehicle_dynamics` type in SHIFT is identical to that of the `SimpleVehicleDynamics` type, in that all of the vehicle dynamics are contained in the main type.

A.2 Automated Vehicles and Controllers

Like the vehicle models in the previous section, the basic SmartAHS controller structure is quite limited and required significant modification to simulate the hierarchical control system and fault diagnostic system presented in Chapters 3 and 4. This section will describe the basic structure of automated vehicles and the physical layer controller as implemented in the SHIFT programming language.

A.2.1 `PATHVehicle` type

At the most abstract level, an automated vehicle is represented by an instantiation of a `PATHVehicle` type. This type attempts to model the sensors, actuators, communication, and control hierarchy that is currently implemented on the experimental vehicles used at PATH. The `PATHVehicle` type contains sensor models for the radar, magnetometer, and communications systems in the

RadarSensor, Magnetometer, and Communications types respectively. The vehicle dynamics are contained in the VehicleDynamics_2D type, as described in the previous Section. The VREP, or Vehicle Roadway Environment Processor handles the interaction between the vehicle and its environment such as the roadway and other vehicles. Sampling of the sensor information is performed by the DataAcquisition type, and then fed to the ControlSystem type for determination of the actuator commands. Finally, the Scheduler type provides a consistent clock so that the various control tasks may be performed in a serial manner. While this may seem contrary to the hybrid system modeling approach, it is necessary that some control task be completed before others may proceed. For example, the fault diagnostics should be completed before a new set of actuator commands are given in order to allow for proper fault management. A schematic of the PATHVehicle type is shown in Figure A.5.

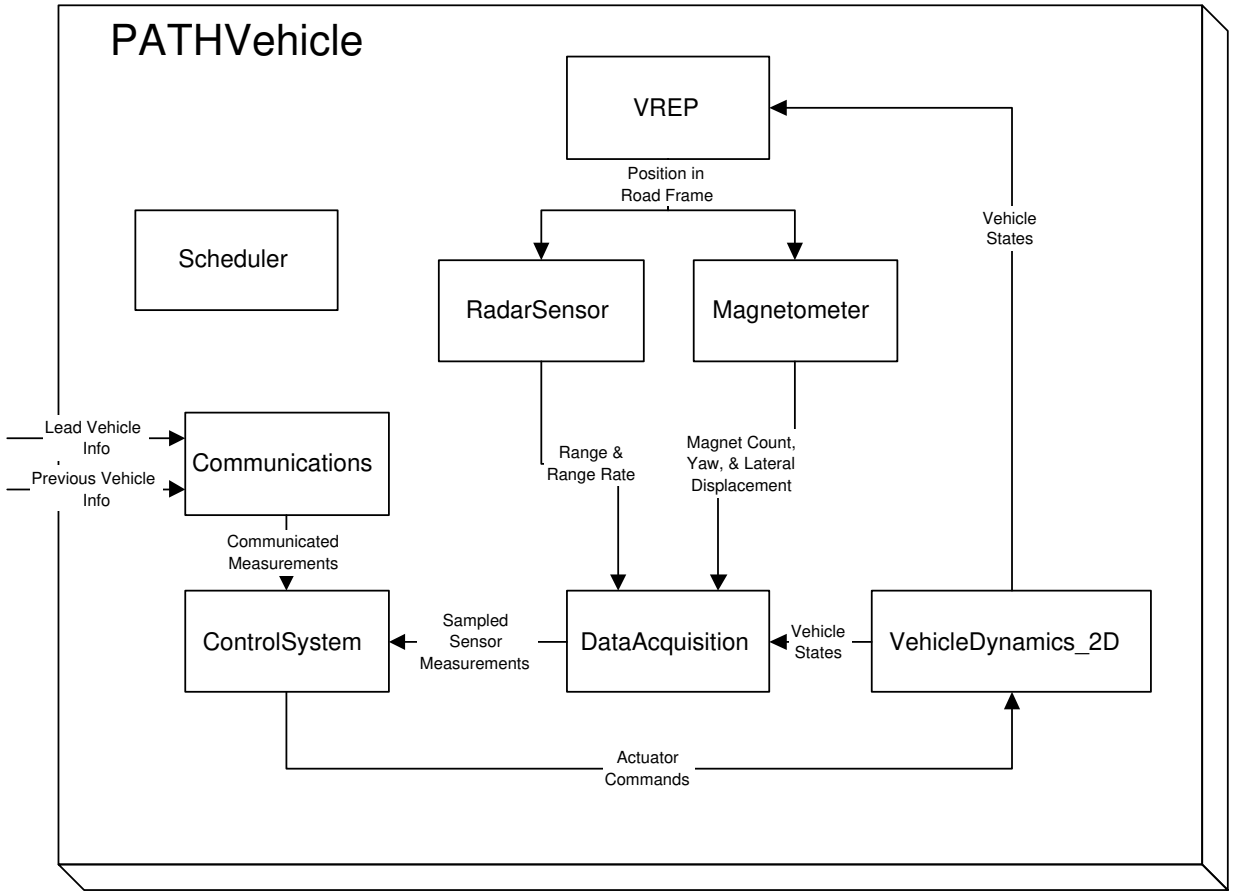

Figure A.5: Schematic of PATHVehicle type

A.2.2 ControlSystem and PhysicalLayer types

Within the ControlSystem type, each level of the control hierarchy described in Chapter 3 has been separated into different types. Currently, only the regulation layer and physical layer controllers have been implemented for the simulation of fault diagnostics. These layers of the control hierarchy have been implemented in the RegulationLayer and PhysicalLayer types, respectively. The PhysicalLayer type has a structure nearly identical to that described

in Section 3.1 as shown in Figure A.7. In addition, the fault diagnostics system is contained within the `FaultDiagnostics` type. A schematic of the `ControlSystem` type is shown in Figure A.6.

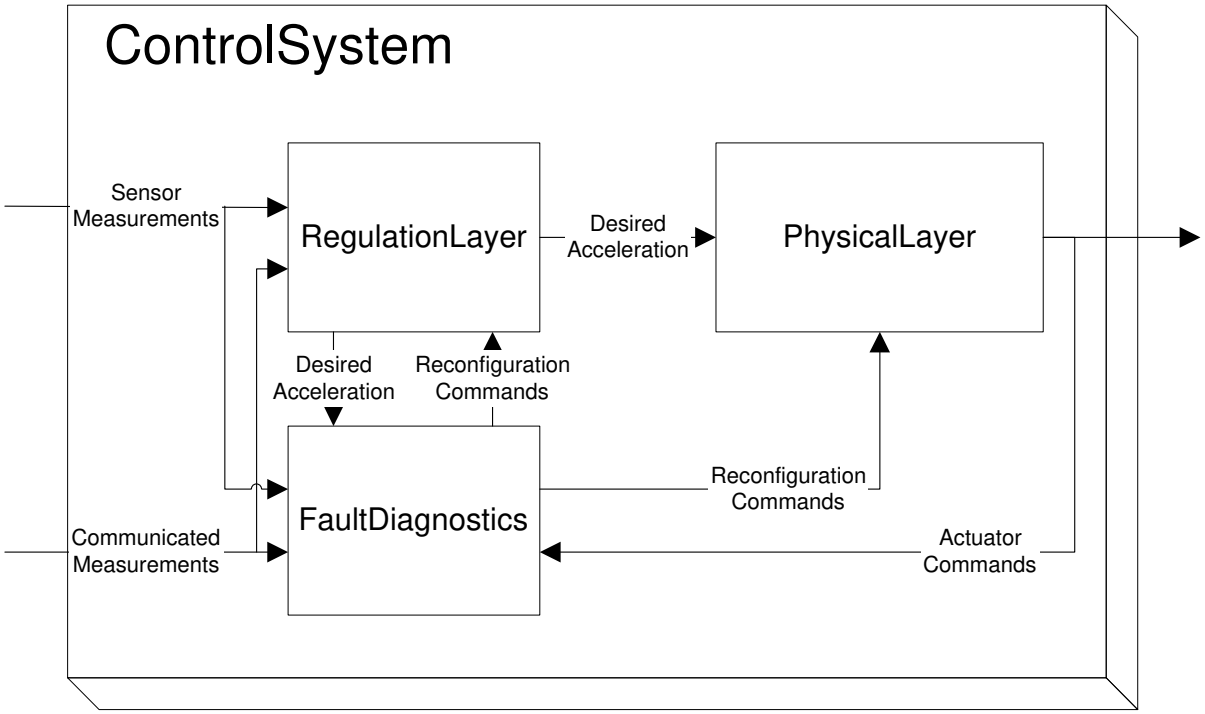

Figure A.6: Schematic of `ControlSystem` type

A.2.3 `FaultDiagnostics`

The `FaultDiagnostics` type is a simple container for the fault diagnostics system for the physical layer controller. The `ResidualGenerator` type contains the parity equations and observers required to form the residual vector, while the `ResidualProcessor` type conducts the least squares estimation, thresholding, and identification of faults. The output of the `ResidualProcessor` type is a flag indicating the current status of the vehicle.

A.3 Regulation Layer Control Systems

A.3.1 Design and Implementation of Normal Mode Control Systems

The regulation control laws is based on the algorithm given by Li *et al.* (1997) and most implementation in SHIFT can be found in Horowitz *et al.* (1998). The structure of implementation can be illustrated as Fig. A.9.

The regulation layer implementation consists of two sublayers: supervisor and maneuver control laws. The regulation supervisor coordinates between each regulation control law according to the commands it receives from the coordination layer. It creates the maneuver control law automaton and starts the maneuvers, and then kills this automaton when it finishes. The maneuver

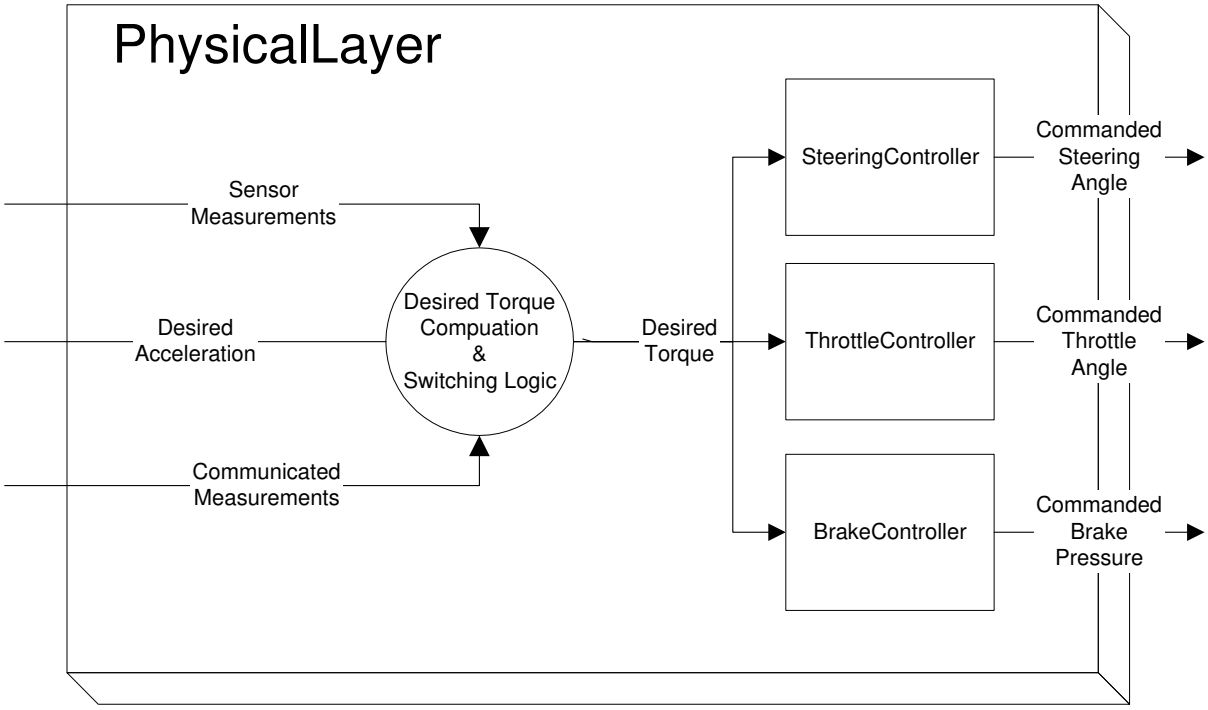

Figure A.7: Schematic of `PhysicalLayer` type

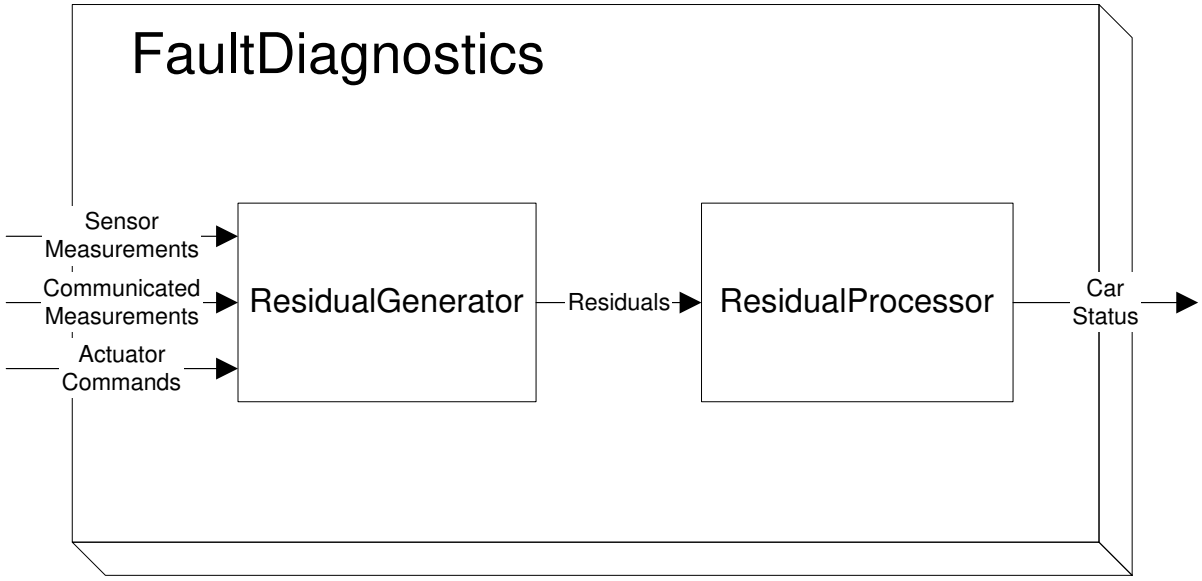

Figure A.8: Schematic of `FaultDiagnostics` type

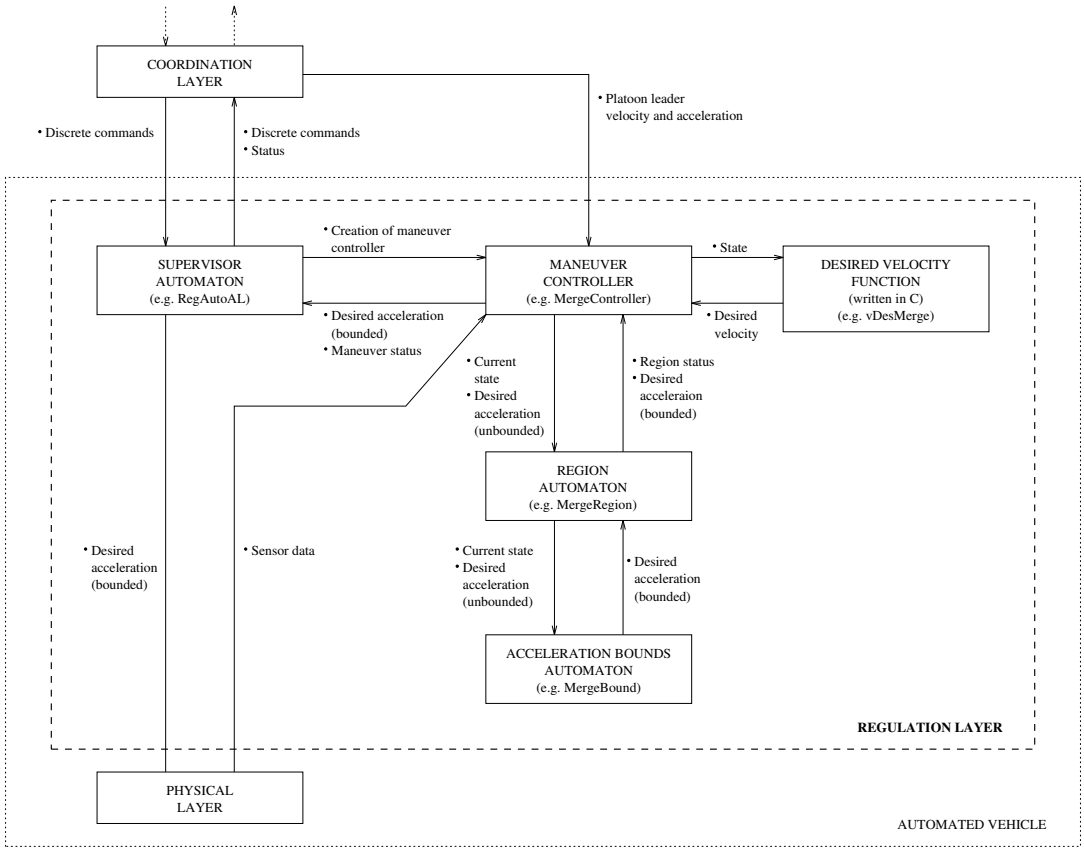

Figure A.9: A schematic of regulation layer implementation

controller consists of four parts: controller, region automaton, bounds automaton and desired velocity function. More details for each part can be found in Horowitz *et al.* (1998).

Currently we have implemented all normal mode regulation control laws. *Lead, merge* and *split* maneuvers are based on the control algorithm given in Li *et al.* (1997), the *follow* controller is given by Swaroop (1994), and the *changelane* controller uses the same safety criterion given by Alvarez (1996) along with a simplified stable lateral motion control. The safety is guaranteed by this controller for lane change, which is different from that implemented in SmartPATH (Eskafi 1996). Another maneuver has been implemented is *stop-light* (Chen *et al.* 1997).

The programs in SHIFT for the regulation control laws are same as those given in Fig. A.9. `regtop.hs` is the regulation supervisor and for each maneuver, `maneuvername_controller.hs, maneuvername_region.hs, maneuvername_bound` are for the controller, region automaton and acceleration bounds automaton, respectively. For the *follow* controller, we have only `follow_controller` due to the string-stability control design (Swaroop 1994).

A.3.2 Implementations of Fault Management Systems in Regulation Layer Level

The implementation of the fault management system in the regulation level consists of three parts, as shown in Fig. A.10. Types `Logic_mans` and `Logic_laws` model the interfaces between the capability of regulation control laws and maneuvers. Type `CapaStruc` uses those maps between fault status and regulation control laws and maneuvers, which has been discussed in section 5.2.1.

Faulty information is passed down to `DataAcq` type to tune the sensor measurement information if some sensor faults have happened.

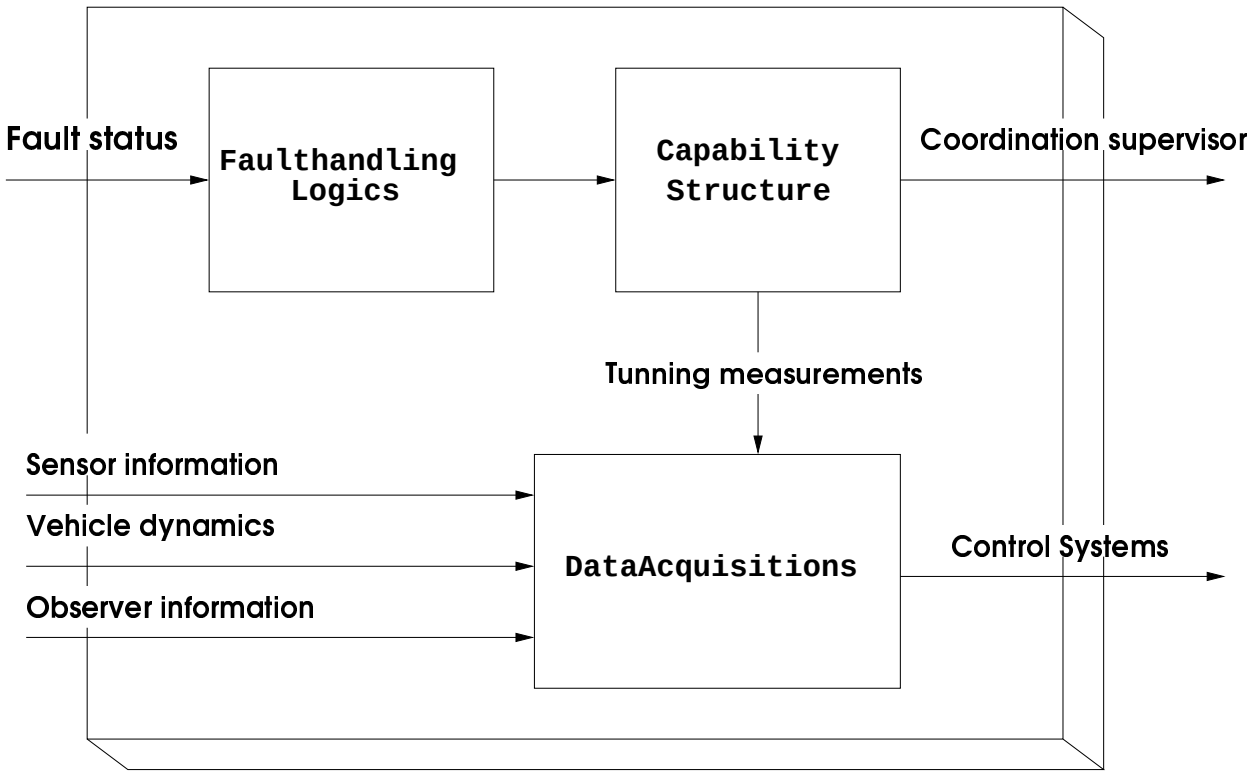

Figure A.10: A schematic of regulation layer fault handling implementation

A.4 Coordination Layer Control Systems

A.4.1 Implementations of Coordination Layer Control Systems

The implementation of communication in SmartAHS is based on the structure proposed by PATH staffs and different from those done in SmartPATH (Eskafi 1996). The communication components must model each layer of the open systems interconnection (OSI) reference model (Eskafi 1998). The OSI structure in an AHS consists of physical, data link, network, transport and application layers. The purpose of the physical layer is to send and receive messages, check the CRC, detect errors, etc. The data link layer is a logical link controller, and it interfaces the physical device and the network layer. The network layer manages the network configuration, address resolution, routing and mobility. The transport layer interfaces the network layer with the application layer. The user instantiates messages through the application layer.

In SmartAHS there is inherent conflict in the interface of the communication domain and the vehicle domain (Murgier 1998). Real hardware communication requires a time step of $\sim 10^{-8}$ sec. However, simulation of vehicle dynamics at this frequency is impractical. The simulation time used in SmartAHS is several orders of magnitude larger (around $\sim 10^{-3}$ sec.). To reduce the requirements of modeling the hardware, communication is simulated at the message level. Most of the

message level approach in SmartAHS has been completed separately by PATH projects (Murgier 1998).

We integrated a simplified version of the communication structure when simulating the coordination, link and network layers. We will interface vehicle control with communication devices at the message level, namely WAN and/or communication between vehicles and roadside. The developed physical layer communication components in SmartAHS can be used to broadcast and transmit the information among the vehicles.

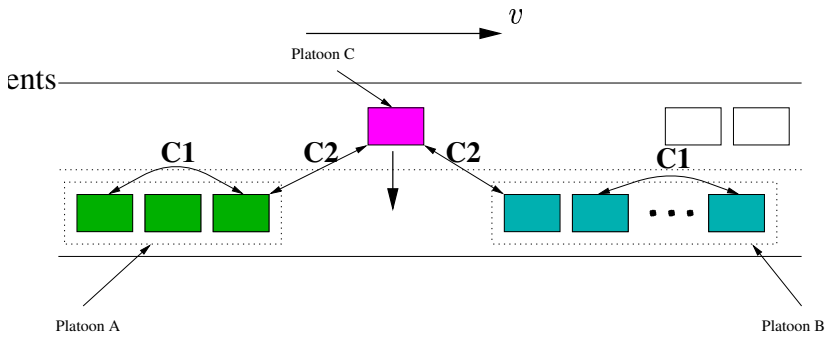

Figure A.11: Message level communication schematic

Figure A.11 shows the basic implementation scheme of the communication among vehicles at the coordination layer level. We will only use the **message** and **physical layer**[1] communication components in our simulation. These components include: *message, transmitter, receiver*, and the *monitor.* When one coordination control protocol initiates a request for a maneuver, the *message* will be created and sent to the transmitter. The *transmitter* broadcasts the messages to the specific vehicles or roadside link layer control systems involved in the maneuver. When the *receiver* accepts the message it will pass it through to the coordination controller. The *monitor* works as a centralized component for the physical layer in the communication. The *monitor* functions as a representation of a set of users adopting the same physical medium; in addition, it models channel properties and keeps track of the transmitters sharing the channel. Also the monitor models the connection type (point to point or broadcast channel). The vehicle ID is passed as part of the vehicle to vehicle communication.

We implemented the coordination layer level communication as shown in the Figure A.11. The communication type C1 denotes intraplatoon communication; for example, if the third vehicle in platoon A wants to *split*, it sends the *split* request to the leader of the platoon by communication type C1. This type of message can be broadcast using the point-to-point connection since each vehicle in a platoon knows the ID of the leader. Another type of communication, C2, can model the coordination communication among different platoons. In the figure, suppose platoon C (free agent) wants to *change lane*. It must communicate with the other vehicles in the adjacent lanes to request space. In SmartAHS, neighboring vehicles are detected using a `Sensor` component, which is described further in the next section (Antoniotti *et al.* 1998). Through this mechanism, platoon C is able to detect which vehicles are in its unsafe region and can send out lane-change requests to those vehicles via the C2 type communication (broadcast channel.)

The implementation of communication between the vehicles and the roadside system is similar

[1]The terminology **message** and **physical layer** comes from the developed communication components in SmartAHS (Murgier 1998).

to the coordination layers. The finite state machines for the communication implementation are listed in the appendix A.4.3.

A.4.2 Implementations of Fault Management Systems in Coordination Layer Level

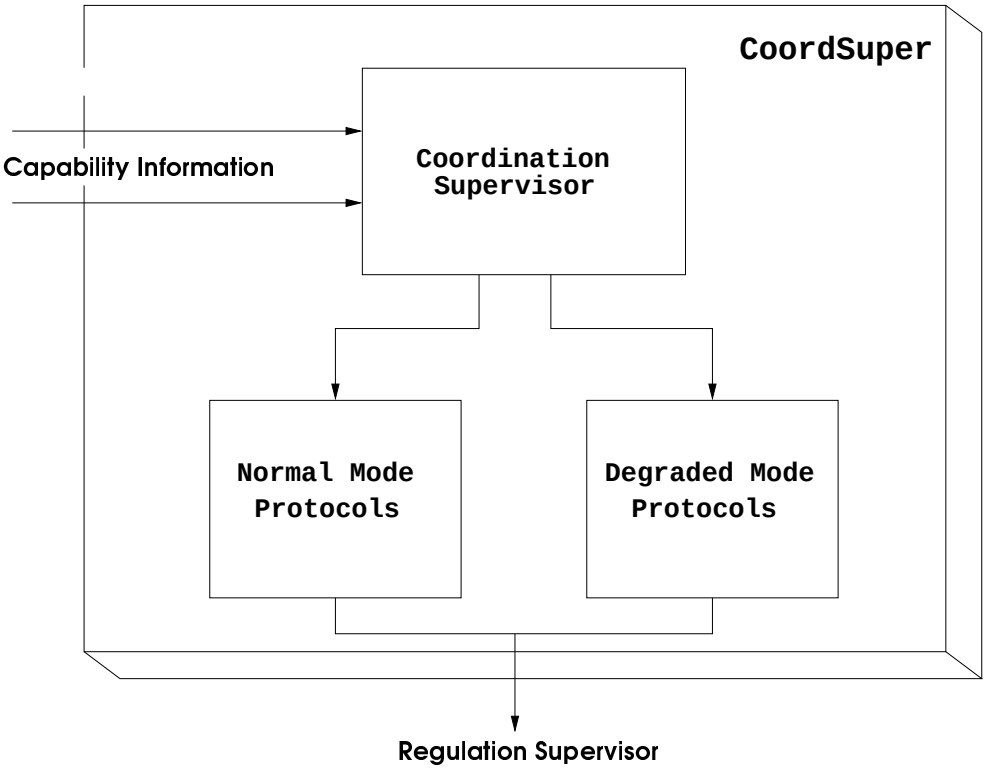

Figure A.12: A schematic of coordination layer fault handling implementation

The fault management in the coordination layer is implemented by the type `CoordSuper` and some degraded mode maneuvers such as `EmergencySplit` etc. Fig. A.12 shows the schematic of the implementation in SmartAHS. The fault status and capability information are sent to the coordination supervisor and the protocols in the coordination supervisor will decide which maneuver should be executed based on current faulty information. As discussed in section 5.2.1, some faults can be dealt with by the fault management system in the regulation layer (see section A.3.2); for more severe faults, degraded mode maneuvers must be initiated. The coordination protocols for these degraded mode maneuvers and normal mode maneuvers are then implemented separately to realize the coordination between vehicles. The degraded maneuver protocols have higher priorities than the normal mode maneuvers.

A.4.3 FSM of Normal Mode Maneuver Protocols

Figs A.13 – A.22 illustrate the maneuver protocols under normal conditions. These protocols were first designed in Hsu *et al.* (1994) and implemented in the SmartPATH simulator by Eskafi (1996). However, we re-designed them by considering the communication protocols and devices

and implemented them in the SmartAHS using SHIFT. The SmartAHS version is much more practical and easily extended and written compared with the previous design and implementation.

We only show the normal mode maneuver protocols here for `lead, join, change lane. leader split`, and `follower split`. Degraded mode maneuver protocols such as `emergency leader split` etc. are similar to these except they do not consider each safety check and handshake.

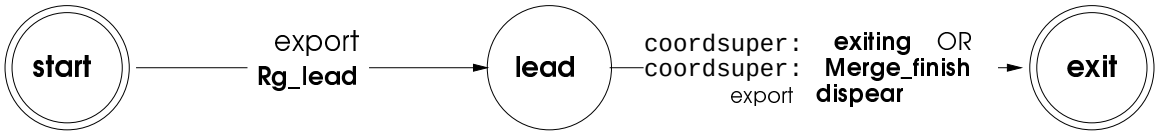

Figure A.13: Lead maneuver protocol

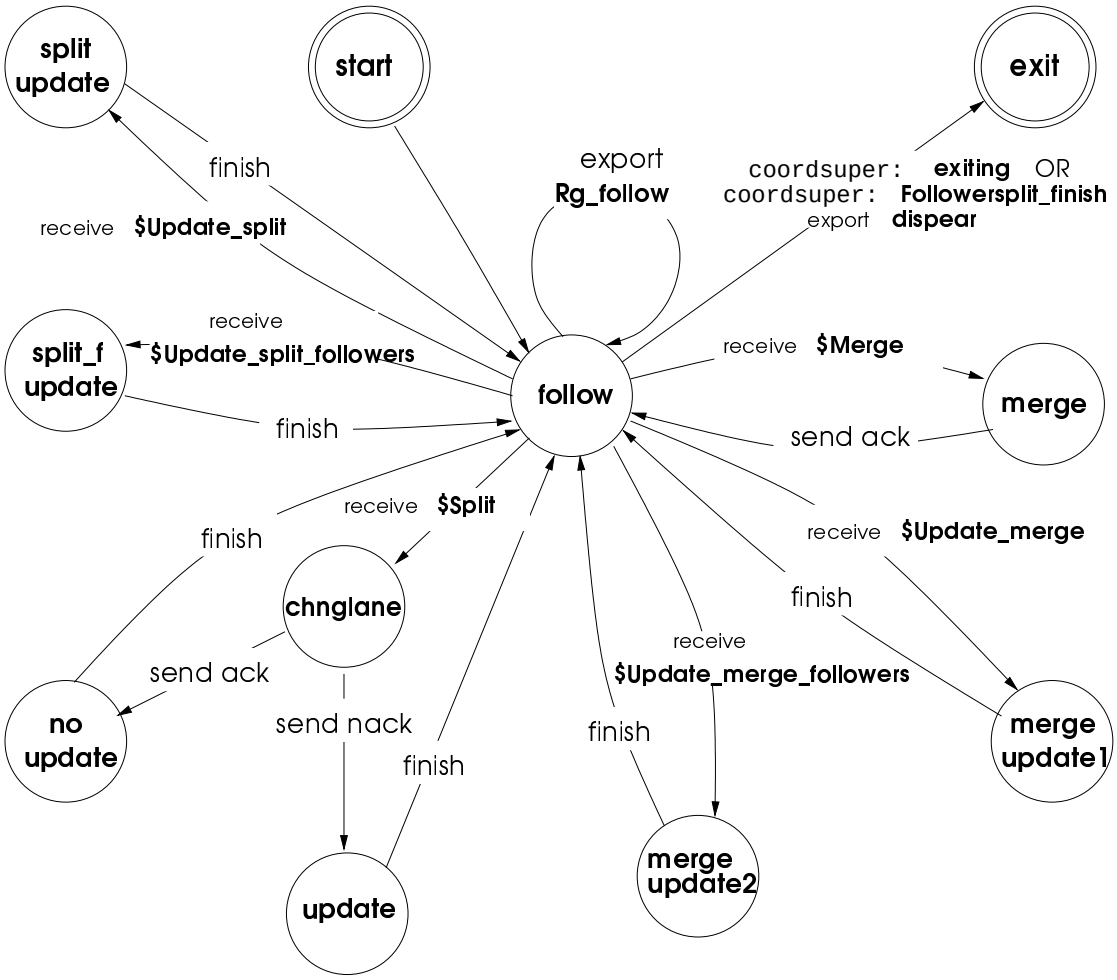

Figure A.14: Follow maneuver protocol

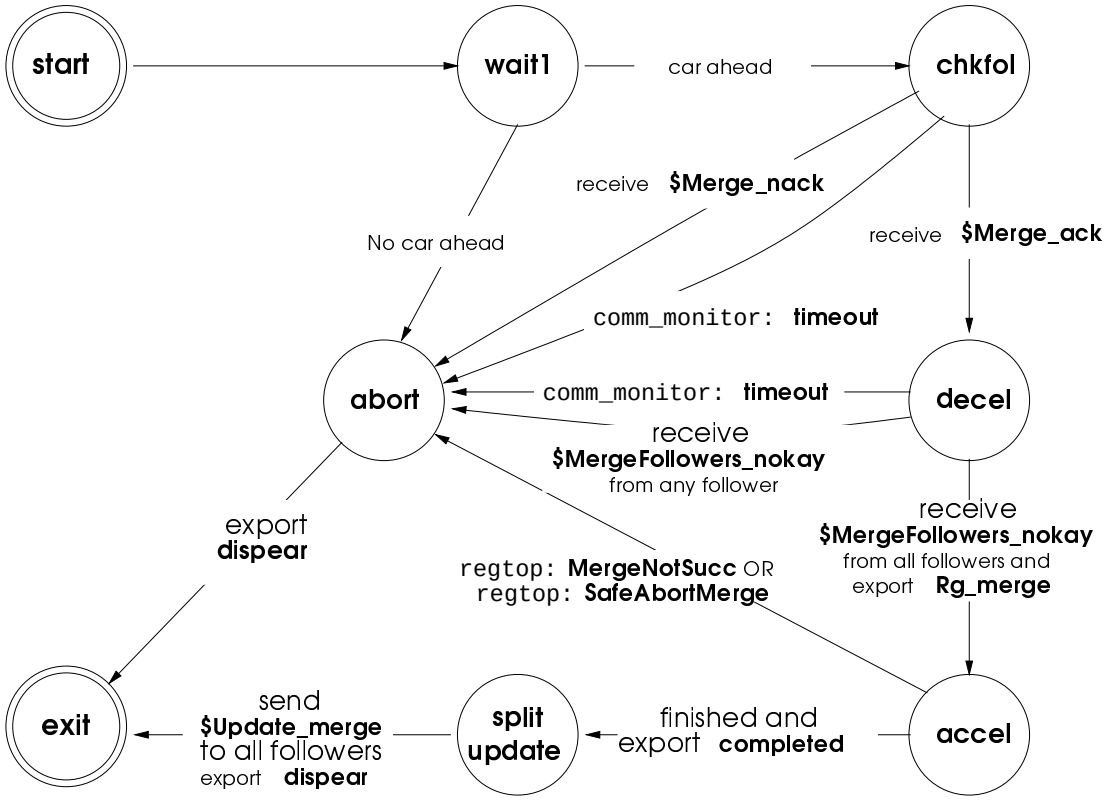

Figure A.15: Merge maneuver initiator protocol

A.5 FSM of Communications Devices in Coordination Layer

Communications in the coordination layer maintains the coordinated maneuvers among different vehicles on the highway. Figs A.23 – A.28 show the FSM diagrams for implementation of these communication devices. As we mentioned in section A.4.1, we only used physical layer components in the communication design such as `Message, Receiver, Transmitter` and `Monitor`. These types are shown by the figures illustrated in this section. Moreover, in this report, we have not discussed about the implementation for communication between vehicles and roadside systems in SmartAHS simulator. This topic is beyond this project and can be found in MOU 383.

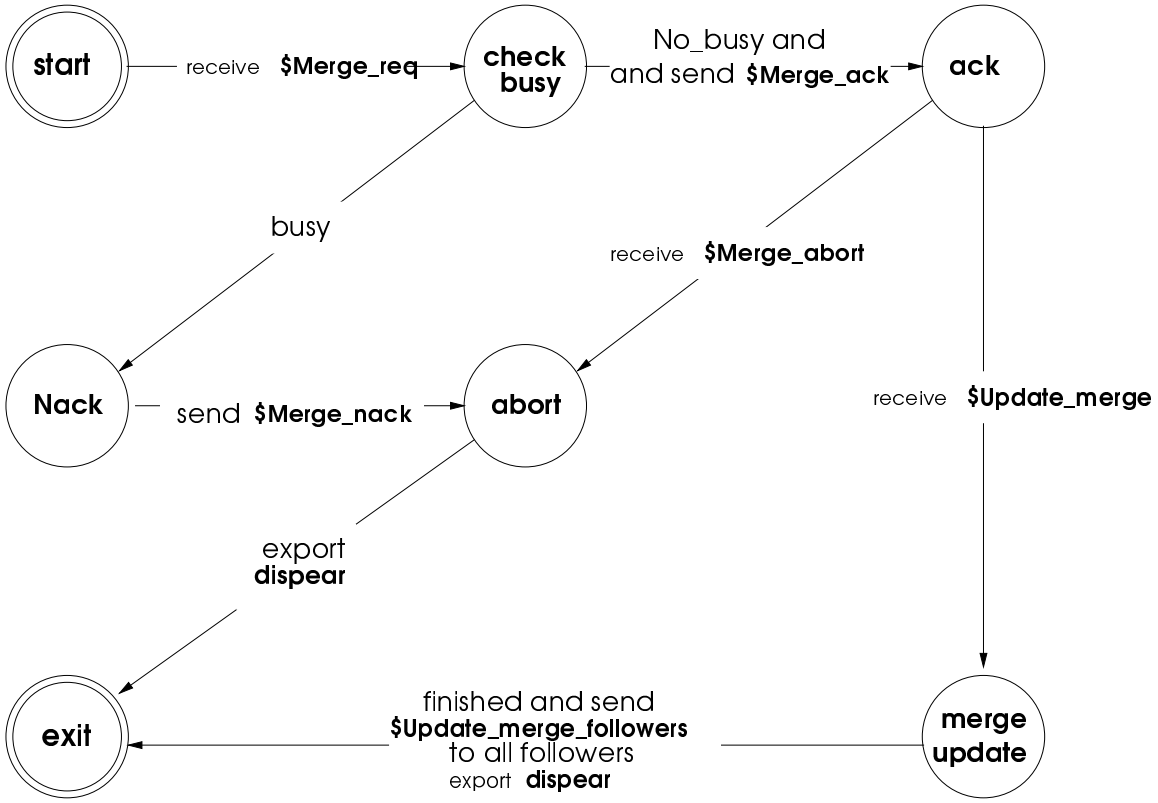

Figure A.16: Merge maneuver responder protocol

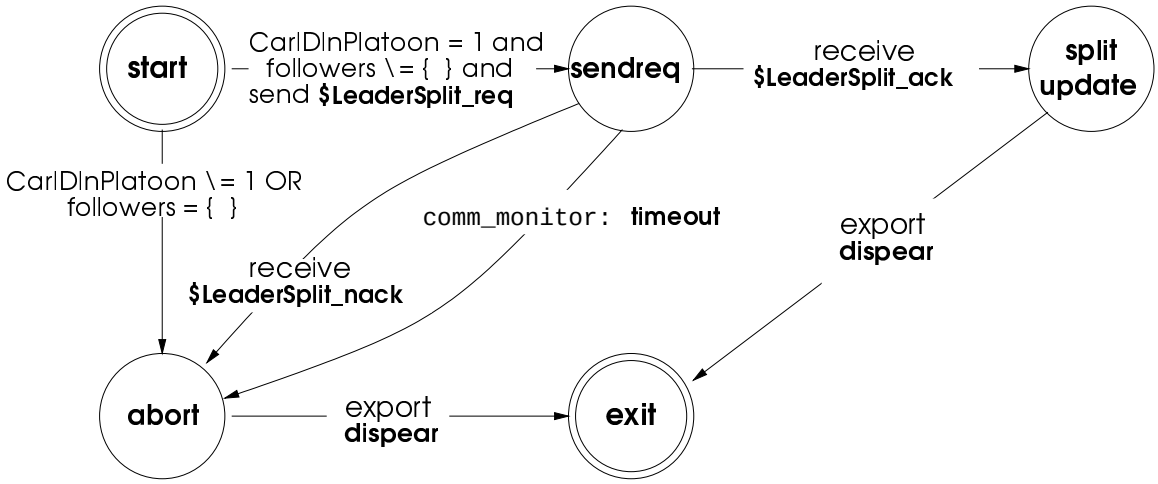

Figure A.17: Leader split maneuver initiator protocol

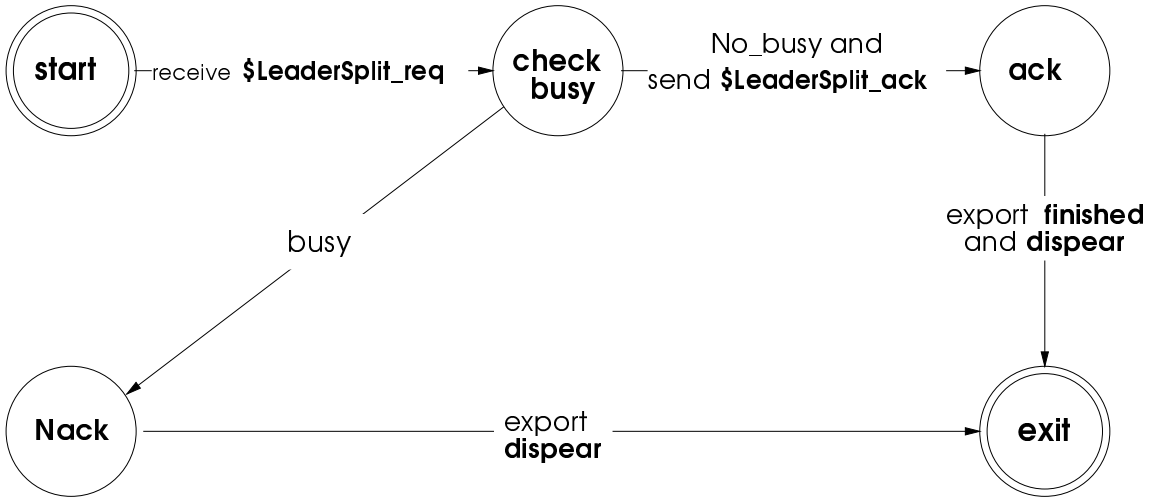

Figure A.18: Leader split maneuver responder protocol

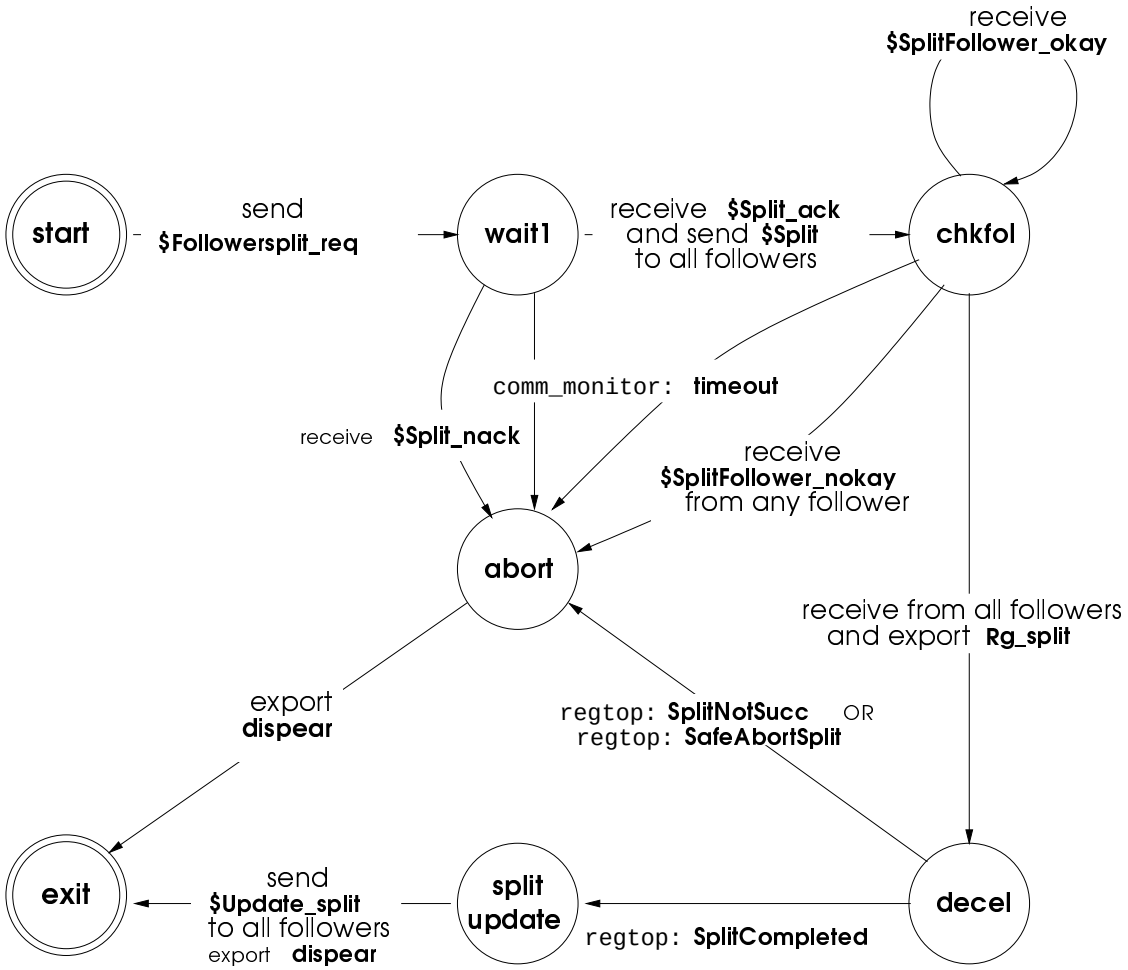

Figure A.19: Follower split maneuver initiator protocol

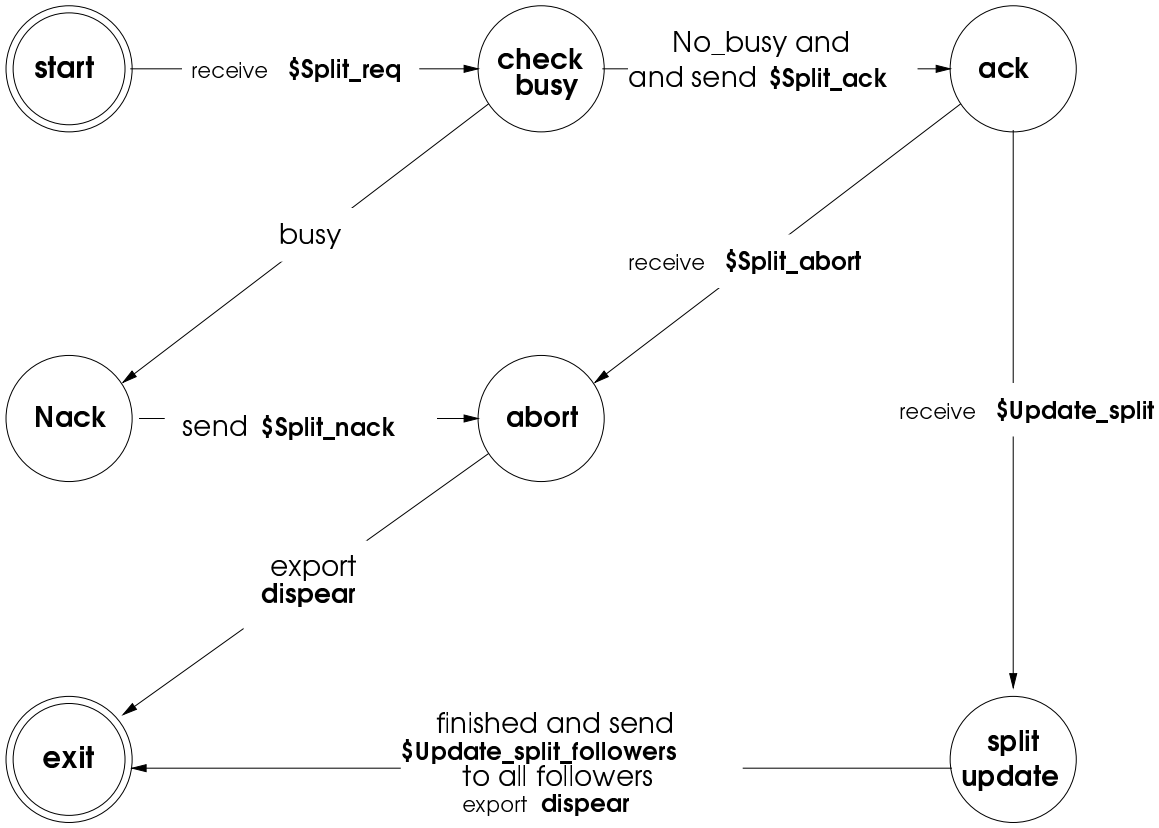

Figure A.20: Follower split maneuver responder protocol

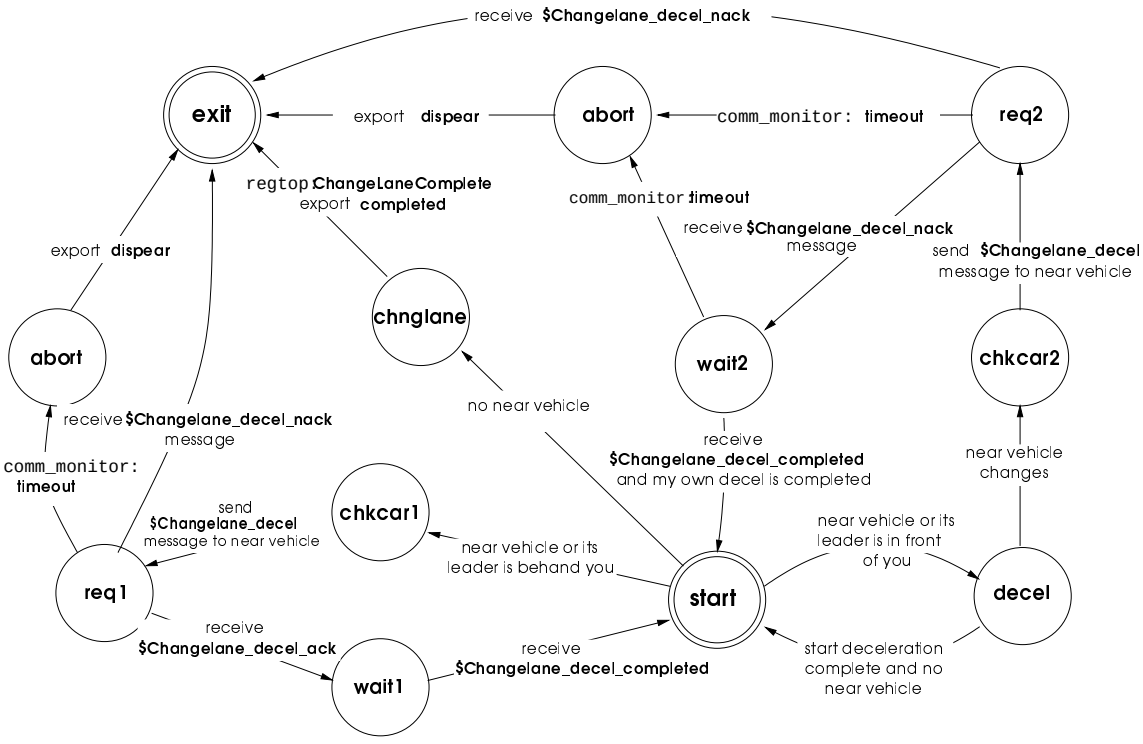

Figure A.21: Changelane maneuver initiator protocol

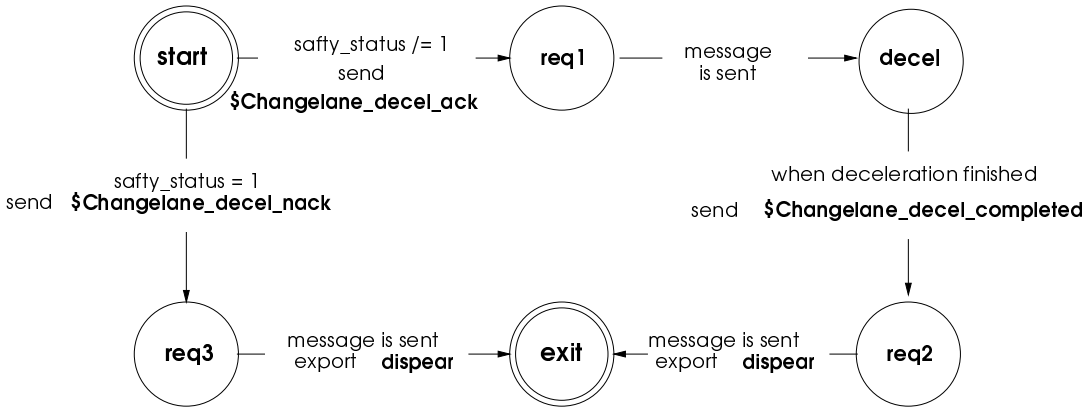

Figure A.22: Changelane maneuver responder protocol

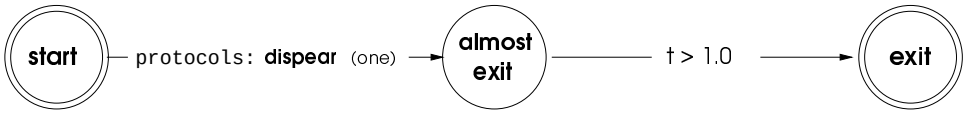

Figure A.23: Coordination layer communication message

Figure A.24: Coordination layer communication ordered message

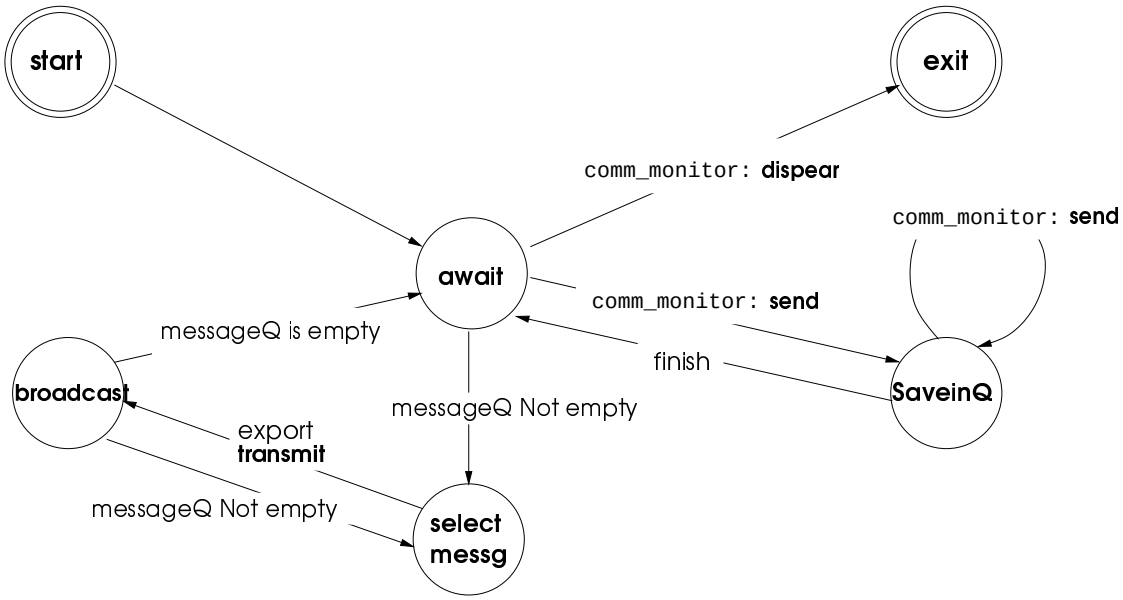

Figure A.25: Coordination layer communication transmitter

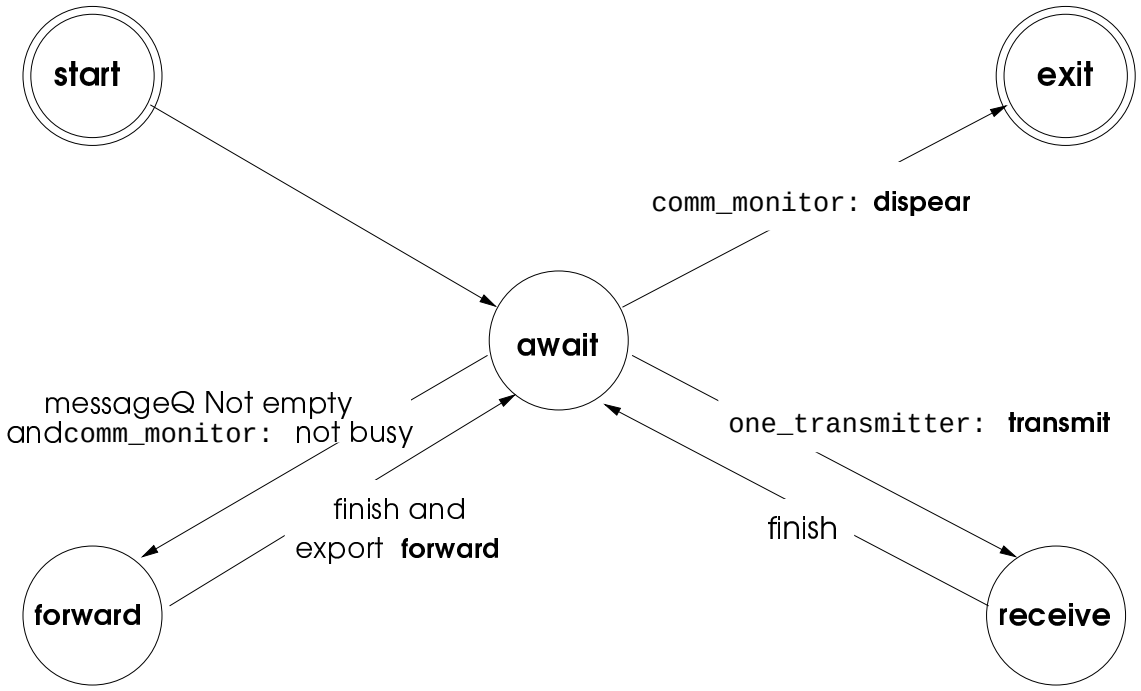

Figure A.26: Coordination layer communication receiver

Figure A.27: Coordination layer communication rejection automata

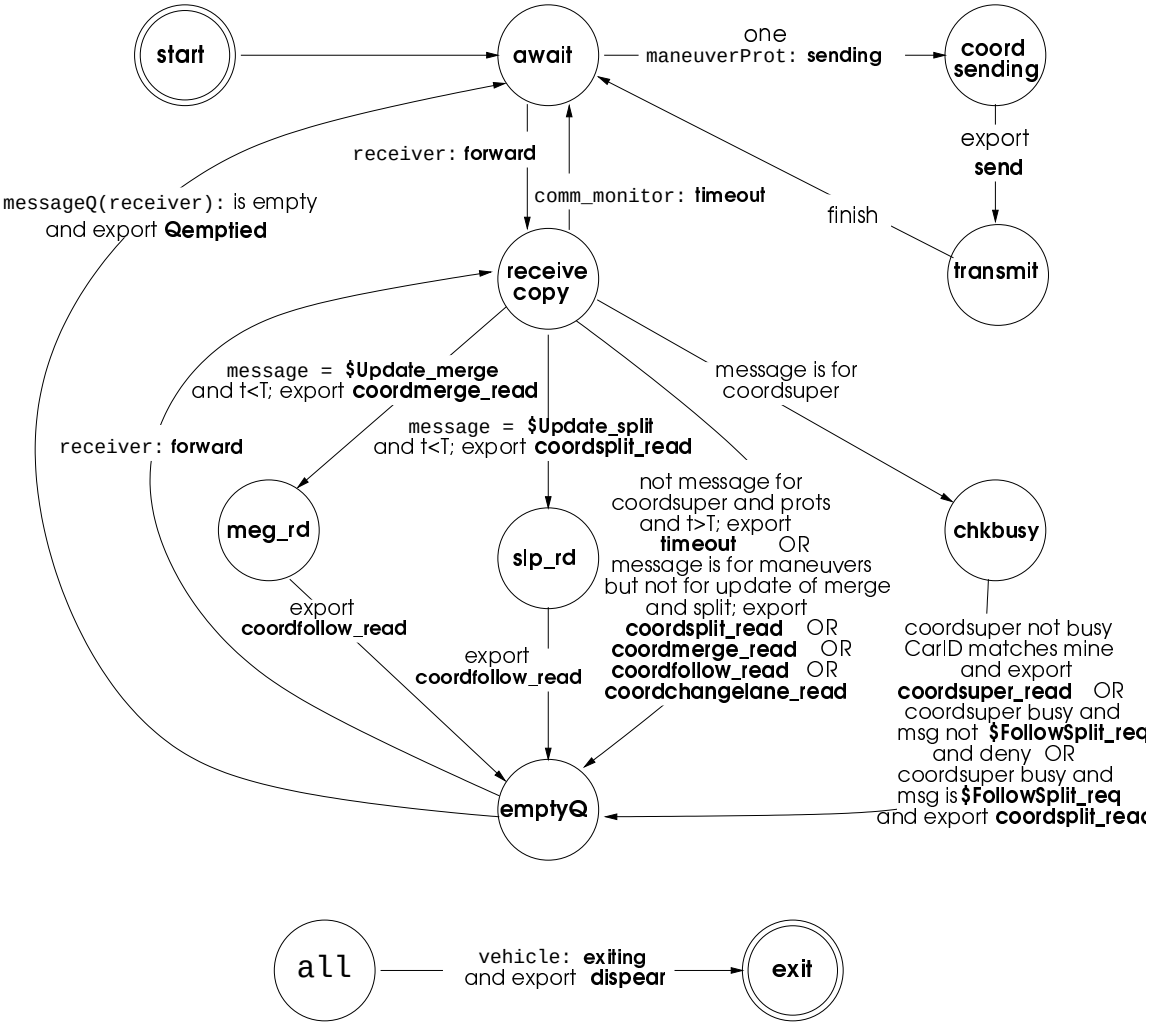

Figure A.28: Coordination layer communication monitor

Appendix B

Proofs of Underestimation Results

Lemma 1, Proof: The proof follows directly from the partial derivative of Eq. (5.28) and lemma assumptions. ■

Lemma 2, Proof: Eq. (5.29) together with Lemma 2 implies that

$$\hat{\lambda}_m < \lambda_m \Leftrightarrow f(\Theta, \hat{\lambda}_m) < f(\Theta, \lambda_m) = 0$$

From Eq. (5.28) it follows that

$$f(\Theta, \hat{\lambda}_m) = \frac{p_2}{p_3} - 1 - \ln \hat{\lambda}_m - \frac{1}{\hat{\lambda}_m}\frac{p_4}{p_3} \tag{B.1}$$

Adding and subtracting the term $\hat{p}_2/\hat{p}_3$ and $1/\hat{\lambda}_m(\hat{p}_4/\hat{p}_3)$ to Eq. (B.1) and using Eq. (5.30) it follows that

$$f(\Theta, \hat{\lambda}_m) = \frac{p_2}{p_3} - \frac{\hat{p}_2}{\hat{p}_3} - \frac{1}{\hat{\lambda}_m}\left(\frac{p_4}{p_3} - \frac{\hat{p}_4}{\hat{p}_3}\right)$$

By Eq. (5.31) $\hat{\lambda}_m \leq \bar{\lambda}_m$ then

$$f(\Theta, \hat{\lambda}_m) \leq \frac{p_2}{p_3} - \frac{\hat{p}_2}{\hat{p}_3} - \frac{1}{\bar{\lambda}_m}\left(\frac{p_4}{p_3} - \frac{\hat{p}_4}{\hat{p}_3}\right)$$

If condition (5.32) holds, $f(\Theta, \hat{\lambda}_m) \leq 0$ and $\hat{\lambda}_m \leq \lambda_m$. ■

Lemma 3, Proof: First notice that as Lemma 3 is satisfied under assumption (iii) of the Lemma, then

$$\hat{\lambda}_m(t_0) \leq \lambda_m(t_0)\ .$$

Using (i) and (ii) in Lemma assumptions, it follows that

$$\begin{aligned} \alpha(t_0) &\leq \tilde{p}_{max}(1 + \bar{\lambda}_m + \bar{\lambda}_m \ln \bar{\lambda}_m) = \delta \\ d &\geq \gamma_1 + \gamma_4 \ln^2 \underline{\lambda}_m \geq \gamma_4 \ln^2 \underline{\lambda}_m \\ 1 &\geq (1 - e^{s4(t-t_0)}) \ \ \forall t \geq t_0 \end{aligned} \tag{B.2}$$

Assume $\gamma_4 > 1$ then $d > \ln^2 \underline{\lambda}_m$, then

$$\begin{aligned} &Eq.\ (5.37) \Rightarrow \tilde{p}_1(t) > 0 \ \ \forall t \geq t_0 \\ &Eq.\ (5.38) \Rightarrow \tilde{p}_2(t) < 0 \ \ \forall t \geq t_0 \\ &Eq.\ (5.39) \Rightarrow \tilde{p}_3(t) < 0 \ \ \forall t \geq t_0 \\ &Eq.\ (5.40) \Rightarrow \tilde{p}_4(t) > \tilde{p}_4(t_0) > 0 \ \ \forall t \geq t_0 \end{aligned} \tag{B.3}$$

Analyzing $\tilde{p}_3(t)$ and $\tilde{p}_4(t)$ in Ineqs. (B.3) it follows that

$$-\frac{1}{\hat{\lambda}_m}\left(\frac{p_4(t)}{p_3(t)} - \frac{\hat{p}_4(t)}{\hat{p}_3(t)}\right) < 0 \ . \tag{B.4}$$

Therefore, for Ineq. (5.32) to hold it is sufficient that

$$\frac{p_2}{p_3} - \frac{\hat{p}_2(t_0)}{\hat{p}_3(t_0)} \geq \frac{p_2}{p_3} - \frac{\hat{p}_2(t)}{\hat{p}_3(t)} \, . \tag{B.5}$$

Using Ineqs. (B.3) in Ineq. (B.5) implies that

$$\frac{\hat{p}_2(t_0)}{\hat{p}_2(t)} \geq \frac{\hat{p}_3(t_0)}{\hat{p}_3(t)} \tag{B.6}$$

For Ineq. (B.6) to hold the ratio in the error reduction for $\tilde{p}_2$ has to be smaller or equal than that of $\tilde{p}_3$. This can be accomplished by Eq. (5.41)

From Ineqs. (B.3), (B.4) (B.6) and (5.41) it follows that condition (5.32) still holds for $t \geq t_0$ and therefore

$$\hat{\lambda}_m(t) \leq \lambda_m(t) \ , \forall t \geq t_0$$

■

Lemma 4, Proof: To analyze the PAA when λ is small consider that the adaptation law in Eq. (5.14) can be expressed component-wise as

$$\begin{aligned} \dot{\tilde{p}}_1 &= -\gamma_1 \tilde{y} \\ \dot{\tilde{p}}_2 &= \gamma_2 \lambda \tilde{y} \\ \dot{\tilde{p}}_3 &= -\gamma_3 \lambda \ln \lambda \tilde{y} \\ \dot{\tilde{p}}_4 &= -\gamma_4 \ln \lambda \tilde{y} \\ \dot{\tilde{p}}_5 &= \gamma_5 v \tilde{y} \end{aligned}$$

The term $\tilde{y} = \mathbf{U}\tilde{\Theta}$ is given by

$$\tilde{y} = \tilde{p}_1 - \tilde{p}_2 \lambda + \tilde{p}_3 \lambda \ln \lambda + \tilde{p}_4 \ln \lambda - \tilde{p}_5 v$$

Notice that when $\lambda \approx 0$, the term $\tilde{p}_4 \ln \lambda$ dominates $\tilde{y}$. There are two possible cases to consider: $\tilde{p}_4(0) \geq 0$ and $\tilde{p}_4(0) \leq 0$.

Case 1: Suppose $\tilde{p}_4(0) \geq 0$, then $\tilde{y}(0) \approx \tilde{p}_4(0) \ln \lambda \leq 0$ when λ is small. Let t_f be the time when $\tilde{y}$ changes sign from negative to positive, i.e. $\tilde{y}(t) \leq 0, \ \forall t \in [0, \, t_f]$ and t_i be the first time parameters $\tilde{p}_i(t)$ change signs, respectively, for $i = 1, 2, 3, 4, 5$. Therefore,

$$\tilde{p}_1(t) \geq 0, \quad \tilde{p}_i(t) \leq 0, \quad i = 2, 3, 4, 5, \quad \forall t \in [0, \, t_f]$$

Let $t_\alpha = \min\{t_3,\, t_4\}$ then by definition of t_i and the facts that $\tilde{p}_4(0) \geq 0$ and $\tilde{p}_3(0) \leq 0$, we have

$$\tilde{p}_3(t) \leq 0, \quad \tilde{p}_4(t) \geq 0, \qquad \forall\, t \in [0,\, t_\alpha] \tag{B.7}$$

consider $\tilde{p}_i(t) := p_i - \hat{p}_i(t)$. Thus, by Eq. (B.7),

$$\frac{p_4}{p_3} \geq \frac{\hat{p}_4(t)}{\hat{p}_3(t)}, \qquad \forall\, t \in [0,\, t_\alpha]$$

To apply Lemma 4 it is necessary to check the other conditions of Lemma 3. Note that

$$\frac{\dot{\tilde{p}}_3}{\dot{\tilde{p}}_2} = -\frac{\gamma_3}{\gamma_2} \ln \lambda > 0$$

and then

$$\frac{d}{dt}\left(\frac{\tilde{p}_2}{\tilde{p}_3}\right) = \frac{\tilde{p}_2 \dot{\tilde{p}}_2}{\tilde{p}_3^2}\left[\frac{\tilde{p}_3}{\tilde{p}_2} - \frac{\dot{\tilde{p}}_3}{\dot{\tilde{p}}_2}\right] = \frac{\tilde{p}_2 \dot{\tilde{p}}_2}{\tilde{p}_3^2}\left[\frac{\tilde{p}_3}{\tilde{p}_2} + \frac{\gamma_3}{\gamma_2} \ln \lambda\right]$$

by the conditions in Lemma 4 it is known that $\tilde{p}_2(t) \leq 0, \quad \dot{\tilde{p}}_2(t) \leq 0,\, \forall\, t \in [0,\, t_f]$, then if γ_3 and γ_2 are chosen such that

$$\frac{\gamma_3}{\gamma_2} |\ln \bar{\lambda}_m| \geq \frac{\tilde{p}_3(0)}{\tilde{p}_2(0)},$$

then

$$\frac{d}{dt}\left(\frac{\tilde{p}_2}{\tilde{p}_3}\right) \leq 0 \tag{B.10}$$

if the initial values for $\tilde{p}_2(0)$ and $\tilde{p}_3(0)$ are chosen such that

$$\frac{\tilde{p}_2(0)}{\tilde{p}_3(0)} \leq \frac{p_2}{p_3},$$

then by condition (B.10)

$$\frac{\tilde{p}_2(t)}{\tilde{p}_3(t)} \leq \frac{p_2}{p_3}, \qquad \forall\, t \in [0,\, t_f] \tag{B.12}$$

and

$$\frac{p_2}{p_3} \leq \frac{\hat{p}_2(t)}{\hat{p}_3(t)}, \qquad \forall\, t \in [0,\, t_f]$$

Pick $t_0 = \min\{t_\alpha,\, t_f\}$, then all conditions for Lemma 3 to hold are satisfied and thus Lemma 4 applies.

Case 2: Suppose $\tilde{p}_4(0) \leq 0$, then $\tilde{y}(0) \approx \tilde{p}_4(0) \ln \lambda \geq 0$ when λ is small. Let t_f and t_i be the first time that parameters $\tilde{p}_i(t)$ change signs, respectively as before in case 1 for $i = 1, 2, 3, 4, 5$. Therefore,

$$\tilde{p}_1(t) \leq 0, \quad \tilde{p}_i(t) \geq 0, \quad i = 2, 3, 4, 5, \quad \forall t \in [0,\, t_f]$$

Notice that for $\forall\, t \in [0,\, t_f]$

$$\frac{\dot{\tilde{p}}_4(t)}{\dot{\tilde{p}}_1(t)} = \frac{\gamma_4}{\gamma_1} \ln \lambda < 0,\ \frac{\dot{\tilde{p}}_4(t)}{\dot{\tilde{p}}_2(t)} = -\frac{\gamma_4 \ln \lambda}{\gamma_2 \lambda} > 0,\ \frac{\dot{\tilde{p}}_4(t)}{\dot{\tilde{p}}_3(t)} = \frac{\gamma_4}{\gamma_3 \lambda} > 0,$$

denote $t_{fi} = \min\{t_i, t_f\},\ i = 1, 2, 3, 4, 5$. Similarly as in case 1,

$$\frac{d}{dt}\left(\frac{\tilde{p}_4}{\tilde{p}_1}\right) = \frac{\dot{\tilde{p}}_1}{\tilde{p}_1}\left[\frac{\dot{\tilde{p}}_4}{\dot{\tilde{p}}_1} - \frac{\tilde{p}_4}{\tilde{p}_1}\right] = \frac{\dot{\tilde{p}}_1}{\tilde{p}_1}\left[\frac{\gamma_4}{\gamma_1}\ln\lambda - \frac{\tilde{p}_4}{\tilde{p}_1}\right] .$$

Using the facts

$$\tilde{p}_1(t) \geq 0, \quad \dot{\tilde{p}}_1(t) \leq 0, \qquad \forall\, t \in [0, t_{f1}]$$

then

$$\frac{d}{dt}\left(\frac{\tilde{p}_4}{\tilde{p}_1}\right) \geq 0, \qquad \forall\, t \in [0, t_{f1}]\,.$$

Noticing that $\frac{\tilde{p}_4(0)}{\tilde{p}_1(0)} < 0$ and by picking γ_4/γ_1 large enough such that

$$\frac{\gamma_4}{\gamma_1}|\ln\bar{\lambda}_m| \geq |\frac{\tilde{p}_4(0)}{\tilde{p}_1(0)}|\,, \tag{B.13}$$

then $t_{f4} \leq t_{f1}$, namely, $\tilde{p}_4(t)$ changes sign before $\tilde{p}_1(t)$.

Similarly,

$$\frac{d}{dt}\left(\frac{\tilde{p}_4}{\tilde{p}_2}\right) = \frac{\dot{\tilde{p}}_2}{\tilde{p}_2}\left[\frac{\dot{\tilde{p}}_4}{\dot{\tilde{p}}_2} - \frac{\tilde{p}_4}{\tilde{p}_2}\right] = \frac{\dot{\tilde{p}}_2}{\tilde{p}_2}\left[-\frac{\gamma_4\ln\lambda}{\gamma_2\lambda} - \frac{\tilde{p}_4}{\tilde{p}_2}\right] .$$

Choosing γ_2 and γ_4 such that

$$\frac{\gamma_4}{\gamma_2}\frac{|\ln\bar{\lambda}_m|}{\bar{\lambda}_m} \geq \frac{\tilde{p}_4(0)}{\tilde{p}_2(0)}\,, \tag{B.14}$$

then $t_{f4} \leq t_{f2}$, namely, $\tilde{p}_4(t)$ changes sign before $\tilde{p}_2(t)$. To make $t_{f4} \leq t_{f3}$ it is necessary that

$$\frac{\gamma_4}{\gamma_3}\frac{1}{\bar{\lambda}_m} \geq \frac{\tilde{p}_4(0)}{\tilde{p}_3(0)}\,. \tag{B.15}$$

Thus, from the conditions (B.13), (B.14) and (B.15), if Ineq. (5.42) in Lemma 4 and Ineq. (5.41) in Lemma 3 hold, then at $t_0 = t_{f4}$, by (B.12) and (5.42),

$$\tilde{p}_4(t_0) \geq 0, \quad \frac{\tilde{p}_2(t_0)}{\tilde{p}_3(t_0)} \leq \frac{p_2}{p_3}, \quad \tilde{p}_1 \geq 0,\ \tilde{p}_i \leq 0, \quad i = 2, 3, 5\,,$$

Applying Lemma 4 then it is possible to achieve

$$\hat{\lambda}_m(t) \leq \lambda_m(t), \qquad \forall\, t \geq t_0$$

■

Theorem 1, Proof: Follows directly from Lemmas 2 to 5. ■

Theorem 2, Proof: Proving the theorem is equivalent to show that $\mu_m/\hat{\mu}_m \geq 1$. By definition of μ, $\hat{\mu}$ and the relationship $y = \ln\mu$, it is equivalent to show

$$\tilde{y}_m := y_m - \hat{y}_m \geq 0 \tag{B.16}$$

note that

$$y_m = p_1 - p_2\lambda_m + p_3\lambda_m \ln \lambda_m + p_4 \ln \lambda_m - p_5 v$$
$$\hat{y}_m = \hat{p}_1 - \hat{p}_2\hat{\lambda}_m + \hat{p}_3\hat{\lambda}_m \ln \hat{\lambda}_m + \hat{p}_4 \ln \hat{\lambda}_m - \hat{p}_5 v$$

then plug above equations in Eq. (B.16)

$$\tilde{y}_m = \tilde{p}_1 - \tilde{p}_5 v - p_2\lambda_m + p_3\lambda_m \ln \lambda_m + p_4 \ln \lambda_m + \hat{p}_2\hat{\lambda}_m - \hat{p}_3\hat{\lambda}_m \ln \hat{\lambda}_m - \hat{p}_4 \ln \hat{\lambda}_m \tag{B.17}$$

Recall that the slip point of maximum friction satisfies Eq. (5.29) and therefore

$$p_3\lambda_m \ln \lambda_m - p_2\lambda_m + p_4 = -p_3\lambda_m \tag{B.18}$$

Using Eq. (B.18) and a similar expression developed from Eq. (5.30) into Eq. (B.17) it follows that

$$\tilde{y}_m = \tilde{p}_1 - \tilde{p}_5 v - \tilde{p}_4 - p_3\lambda_m + p_4 \ln \lambda_m + \hat{p}_3\hat{\lambda}_m - \hat{p}_4 \ln \hat{\lambda}_m \tag{B.19}$$

Expanding $\ln \lambda_m$ in a Taylor series about $\hat{\lambda}_m$ and taking the firt two terms

$$\begin{aligned}\tilde{y}_m &= \tilde{p}_1 - \tilde{p}_5 v - \tilde{p}_4 - \tilde{p}_3\lambda_m - p_3(\lambda_m - \hat{\lambda}_m) + \tilde{p}_4 \ln \hat{\lambda}_m + \frac{p_4}{\hat{\lambda}_m}(\lambda_m - \hat{\lambda}_m) \\ &= \tilde{p}_1 - \tilde{p}_5 v - \tilde{p}_4(1 - \ln \hat{\lambda}_m) - \tilde{p}_3\lambda_m + (\lambda_m - \hat{\lambda}_m)\left(\frac{p_4}{\hat{\lambda}_m} - p_3\right) .\end{aligned}$$

By Lemma 3,

$$(\lambda_m - \hat{\lambda}_m)\left(\frac{p_4}{\hat{\lambda}_m} - p_3\right) > 0\,, \tag{B.20}$$

and

$$-\tilde{p}_3\hat{\lambda}_m > -\tilde{p}_3\underline{\lambda}_m\,,$$
$$|1 - \ln \hat{\lambda}_m| < |1 - \underline{\lambda}_m|\,,$$

and therefore for $\tilde{y}_m > 0$ it is sufficient that

$$\tilde{p}_1 - \tilde{p}_5 v - \tilde{p}_4(1 - \ln \underline{\lambda}_m) - \tilde{p}_3\underline{\lambda}_m > 0\,.$$

that is the condition required in the theorem.

■